The Development of an In-Vitro System for the Study of Osteoarthritis in a Mouse Model

A dissertation submitted by

Christopher R. Nehme

In partial fulfillment of the requirements for the degree of

Doctorate of Philosophy

in

Mechanical Engineering

Tufts University

May 2017

Adviser: Professor William Messner

Abstract

Osteoarthritis (OA) is a painful and debilitating disease of the human joints. Sufferers of OA face a lifelong struggle with the chronic disease. Current treatment options are directed at pain and inflammation management, occasionally culminating in total joint replacements for qualifying patients. To date, no comprehensive treatments have been developed, partially attributed to limitations in current OA research models. With the incidence of OA constantly on the rise, in part due to our aging population and increasing life spans, the necessity of comprehensive treatment options is becoming inevitable.

A novel model for studying OA in a mouse model was developed. A first generation system capable of actuating and culturing amputated murine stifle joints was designed, fabricated and tested. The system comprises of: a mechanical device that maintains a stifle joint in a culture medium reservoir and actuates the joint through a controlled flexion-extension profile; and a microcontroller board used to run an open-loop controller supporting the device's function. The system was used to investigate the effects of actuation and culture medium glucose concentration on the articular cartilage of stifle joints harvested from eight-week-old $NF_\kappa B$/Balb C mice. Results suggest that a high concentration of glucose (9.0 mg/ml) in Dulbecco's Modified Eagle's Medium (DMEM) used to culture dynamically actuated joints promotes a higher degree of joint damage as measured by quantification of Safranin-O staining loss, as opposed to moderate (4.5 mg/ml) and low (1.0 mg/ml) glucose concentrations.

A second-generation system was then developed, addressing limitations identified in the first-generation system related to repeatability, reliability and usability. The design

process focused on developing a pair of robust coupled four bar linkage systems with the ability to repeatedly actuate the joint through a well-defined and repeatable flexion extension cycle. A novel joint clamping and mounting system was also developed to minimize user uncertainty associated with experimental set ups. The device's function is supported by a closed-loop speed control system combining proportional-integral (PI) action with an iterative feed forward controller. The superior controllability of this system allowed investigation into the effects of actuation cycle rate and relative activity-rest durations on joint health. Results demonstrate that the system is capable of causing a range of damage as measured by Safranin-O staining loss on joint samples by varying activity cycle durations.

Finally, substantial work was directed towards extending the functionality of the second-generation system to implement active loading control, effectively allowing the device to control the loads at a mounted stifle joint as function of the cycle position. A second PI control system was developed to control load by sensing bending torque in a system link. Extensive experimental and analytical modeling was performed to develop a working control system. Several limitations of the controllability were determined due to the system geometry and assumptions made during the design process. Nevertheless, it was successfully demonstrated that with proper loading profile considerations, accurate control could be achieved, opening the door for a plethora of future research.

Acknowledgements

The work presented here is the result of extensive collaboration and its completion must be attributed to several people. I would first like to thank my advisor, Dr. William Messner. His support, creativity and insight have all been vital in overcoming countless challenges I have faced. I want to express my deepest gratitude to Dr. Li Zeng and her team for warmly welcoming me to work in their lab. They are one of the hardest working and most dedicated research groups I have ever had the pleasure of working with. I would also like to thank Dr. Robert White and Dr. Alan Grodzinsky for serving on my committee and their support and recommendations. I also want to recognize Dr. Thomas James for introducing me to the project and designing the first generation system.

I want to thank Carrie Hui Mingalone for patiently working alongside me on this project from the beginning and teaching me almost everything I know about molecular biology techniques. I also want to thank Kirsten Garvey for her extensive contributions in tirelessly sectioning, staining and analyzing samples as well as developing some of the fantastic figures included in this dissertation. I want to recognize Rose Banks who worked significantly on the experiments investigating glucose concentration. I would also like to thank Judith Hollander for all her help in setting up experiments as well. I want to recognize Ramesh Govindan for his contributions to the design process.

Finally I want to acknowledge my colleagues in the Mechanical Engineering Department: Fangzheng Guo, Jiabin Zhang, John Scott Parker, Dominic Guri and Piers Echols-Jones; all of whom have in one way or another given me new perspective and highlighted unseen paths forward.

Table of Contents

List of Figures

List of Tables

1

Introduction

1.1 Background & Motivation

This dissertation develops and validates an *in vitro* system capable of producing osteoarthritis (OA)-like joint damage in explanted stifle joints of laboratory mice, with the aim of studying the progression and treatment of OA. Joints are biomechanical components that are key to the healthy function of the body. Acting as connections and mating points between bones, joints enable motion of the limbs and provide the mechanical support necessary to maintain the dynamic integrity of the body during physical activity. A typical joint consists of articular cartilage attached to two or more tangential bone surfaces, with ligaments and other tissues maintaining structural components in place. This entire structure is enclosed in the joint capsule and synovial fluid present between the articular surfaces acts as a lubricant. Functionally, the joint provides resistance to compressive and shear stresses [1]. In particular, the knee joints of the human body are essential to the well-being of a person as they play a significant role in locomotion and several day-to-day activities.

Given their critical role in supporting body function, joint diseases can greatly degrade quality of life. Although numerous medical conditions can affect joint function,

osteoarthritis (OA) is of particular interest to researchers and medical professionals due to its relatively high prevalence, and the limited availability of treatment options. Typically referred to as a "wear and tear" disease due to the suspected role of repeated mechanical stresses in the initiation and propagation of the disease, OA causes inflammation, and loss of cartilage within the joint (Figure 1), triggering significant pain in patients [2]. Due to the high loads and large ranges of motion experienced, the knee is the most frequent joint to be affected by OA. Currently, no comprehensive treatment is available to reverse or halt the disease. Due to the chronic nature of OA, the only available treatment for sufferers is directed at pain management and slowing the progression.
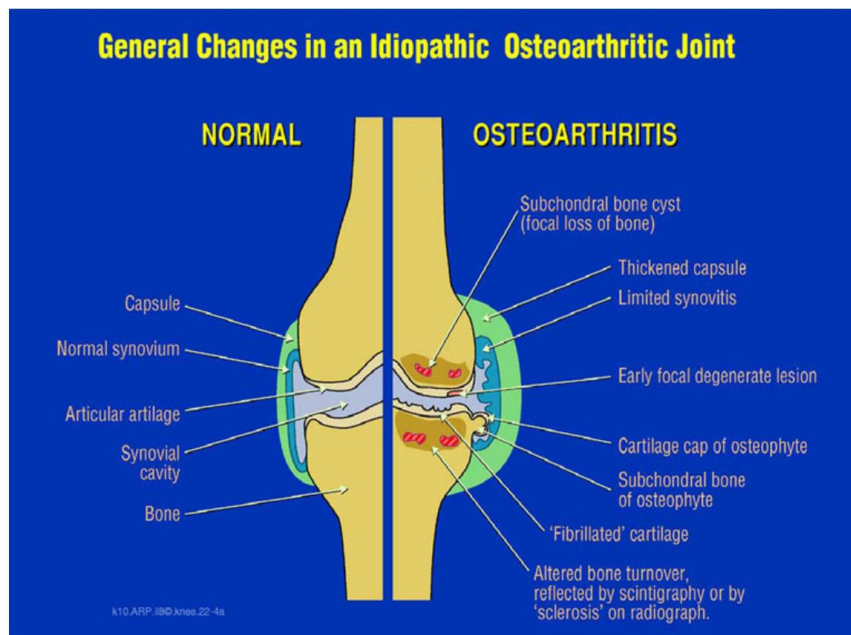
Figure 1: Osteoarthritis is manifested by changes in all the tissues in the joint. The disease involved degeneration of cartilage, subchondral bone as well as other supporting structures of the joint. Figure taken from Poole et al. [3]

The progress of research on comprehensive OA treatments is hindered by the difficulty in replicating the effects of repeated mechanical stresses within the joint under *in vivo* conditions [2]. Currently, two approaches are used to study the mechanisms and treatments options related to OA:

1) *in vivo* animal models in which laboratory animals (typically mice and rats) are encouraged to over-exercise to the point of OA-like damage to the joint. This approach is limited by the researchers' ability to ethically encourage the animals to exercise to the point of damage; and although destabilizing surgeries, chemical interventions or genetic modifications can be used to initialize damage of the joint, such approaches do not accurately mimic the conditions of long-term harm seen in OA.

2) *in vitro* models in which cartilage tissue is cultured and mechanical loading is applied directly to the tissue pieces. The limit of this approach is that it does not account for the biomechanical structure of the joint nor the biochemical interaction between various tissues in the joint. Consequentially this results in non-realistic stress distributions across the tissues.

The limitations of both approaches have made it difficult to study OA and develop effective treatment schemes for it. Therefore, there exists a strong motivation to develop and investigate alternate approaches to study OA pathology and treatments.

1.2 Problem Statement

In order to make significant progress in the research towards treating OA, it is necessary to study the progression of OA and potential treatment options in a representative yet controlled setting. An *in vitro* system, where whole joints can be cultured and subjected to conditions which result in OA-like injury of the joint structure would provide a novel approach to studying the progression and treatment of OA. The successful development and employment of such a system could have life-changing impacts on future OA patients.

1.3 Research Objectives

The ultimate goal of this work has been to develop an independent system that may be used by biomedical researchers, with ease, to study OA pathology and screen treatment options. As such the scope of this work has been fitted to include not only mechanical design of the system, but to develop all supporting hardware and software components, necessary analytical models, and experiment protocols. To achieve these goals, the following research objectives were pursued and completed:

(i) Design and fabricate a system capable of applying cyclic motion and active mechanical loading profiles to explanted murine stifle joints, while maintaining joint viability;

(ii) Development of analytical models for the system that describes the loading state of the stifle joint during the loading cycle as a function of mechanical actuator inputs;

(iii) Development and implementation of closed-loop control systems for controlling the flexion angle of the stifle in concert with a specified loading profile at the joint;

(iv) Investigation of the effect of different flexion cycle frequency profiles on explanted mouse stifle joints using the developed system.

1.4 Organization of the Dissertation

This dissertation presents a full record of the development of a novel system for the study of OA in a murine model. Beginning with Chapter 2, a review of the past literature will outline the anatomy and function of the human knee joint, the pathological features of OA, the current state of research and treatment options for combating the disease, and a detailed history of the development and use of knee simulating systems for various research applications. Chapter 3 describes the development and use of a first generation system for studying OA *in-vitro*, capable of actuating an amputated murine stifle joint over a predefined flexion profile. The effects of glucose concentration in the culture medium on the health of the joints will be presented and discussed. Chapter 4 presents the development of a second-generation system, addressing several shortcomings of the system described in the previous chapter. This chapter will cover the electromechanical design, analytical modeling, control system design and experimental use of the system to investigate the effects of flexion cycle profile on health of amputated murine stifles. Chapter 5 presents methods of extending the functionality of the second-generation device to include the application of controlled force profiles at the stifle joint. Chapter 6 presents concluding discussions and remarks, as well as limitations of the current system and suggestions for future work.

2

Review of Literature

2.1 Overview of Knee Joint Anatomy

The knee is a critical component of the human body, providing stability and mobility. It is also one of the most mechanically intricate joint structures in the body, effectively consisting of two asymmetrical bearing surfaces, the cartilage coated tibial and femoral condyles. The patella (commonly referred as the "kneecap") is a third bone on the anterior side of the joint. The compliant medial and lateral menisci lie between the tibial and femoral condyles. The anterior cruciate ligament (ACL), posterior cruciate ligament (PCL), lateral collateral ligament (LCL) and medial collateral ligament (MCL) are the most important of a collection of fibers and ligaments that connect and stabilize the joint structure [4]. The ligaments are composed of parallel running collagen fibers. In particular the cruciate ligaments are fundamental in maintaining mechanical stability of the knee [5]. The joint components are enclosed in a capsule and synovial fluid is secreted between the articular surfaces providing lubrication. Healthy operation of the knee joint is contingent on the integrity of all the components. See Figure 2 for a full schematic representation of the human knee.
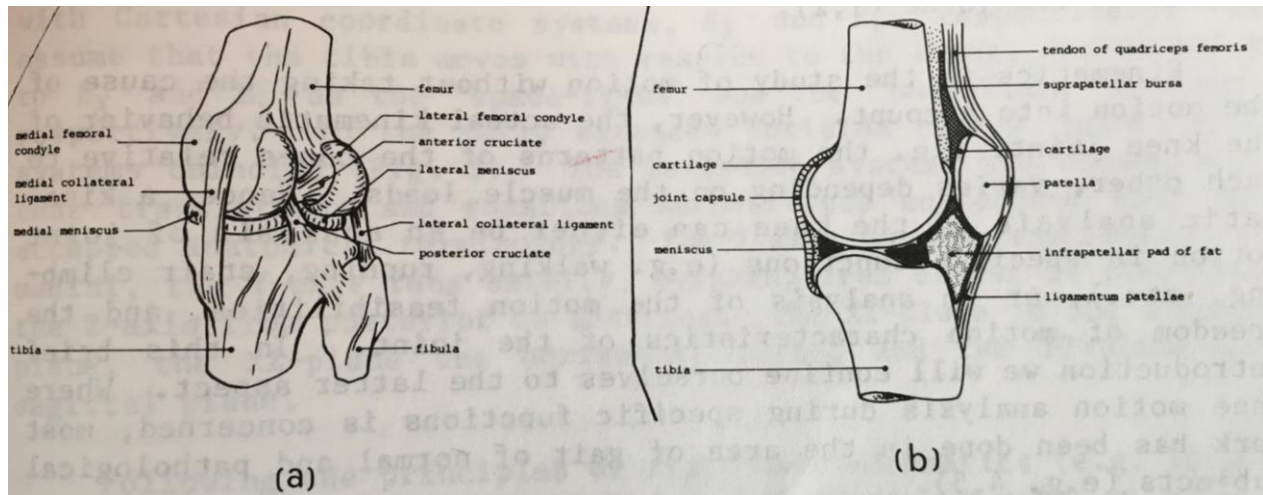
Figure 2: a) Postero-medial view of the knee joint showing major components. b) sagital section of the knee joint with major components. Figure taken from Girgis et al. [6].

The knee primarily moves in flexion, but provides a significant amount of exo-endorotation, (rotation around the tibial axis) [4] and limited yet measurable motion in all other directions. Effectively it can be thought of as a "modified hinge" [7]. Motion is actuated by a system of muscles: the knee extensors, flexors, adductors and abductors [5] (see Figure 3). The physical state of the knee is primarily determined by the flexion angle, and additionally described by internal/external rotations (i.e. rotation of the femur relative to the tibia along the tibial axis), anterior/posterior (AP) displacement and medial/lateral (ML) displacement. The knee flexion angle is defined as the supplementary angle of the internal angle between the femur and tibia. In humans, the knee's natural envelope of motion ranges from a flexion angle of 0° (i.e. full extension) to 145° [8].
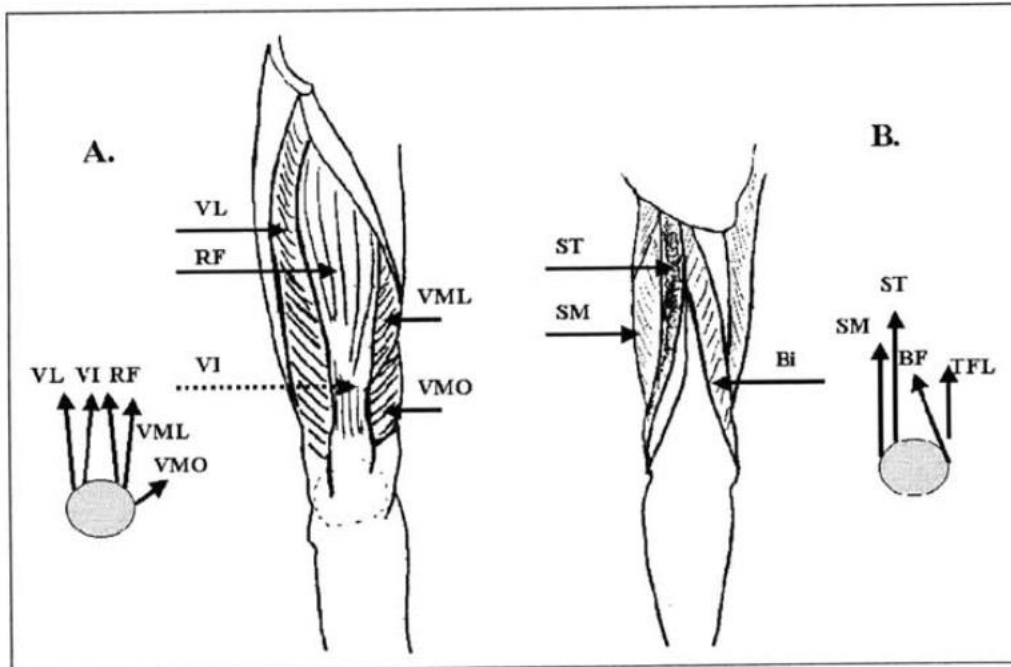
Figure 3: The major muscles of the knee joint: A. Anterior view of major muscles of the knee: Quadriceps group (VL, vastus lateralis; RF, rectus femoris; VM/ VML, vastus medialis; VI, vastus intermedius; VMO, vastus medialis oblique fibers). B. Posterior view of the major muscles of the knee: Posterior thigh muscles (ST, semitendinosus; SM, semimembranosus; Bi; biceps; TFL, tensor facia lata). Figure and caption taken from Most [5].

The knee joint experiences loads in all three spatial dimensions, leading to a total of six independent possible loads (including both linear and rotational loads). Researchers have quantified these loads for various activities including walking [9-11], running [9, 12], stair climbing [10, 13] and cycling [14-16] using a variety of methods. The knee typically experiences compression in the range of two to eight times the body weight of the host during such activities. However, a healthy joint structure is capable of transmitting and directing these loads without causing injury to the host. Further details of the knee as a mechanical system can be found in [4].

2.2 Osteoarthritis in Humans

OA is a degenerative disease of the articular joints. In humans, the knee is most commonly affected joint in the body. The disease is painful and debilitating, causing a significant and progressive decrease in the quality of sufferers' life [17]. The progression is often patient specific and can involve a single or multiple joints [2]. Often the disease progresses to a point where function of the affected joints is completely inhibited. Although classically thought to only affect the articular surface, OA is now understood to affect nearly all components of the joint (see Figure 1) [17]. However, cartilage degeneration is the primary symptom of OA.

The disease is caused by a number of factors; combinations of genetic, biological, environmental and mechanical elements contribute to the development of OA. Commonly cited risk factors include obesity, old age, prior joint injury, and occupations involving high activity levels [18]. The disease pathway and progression is highly complex and still the subject of extensive research. However, the role of joint mechanics and the production of high or abnormal stresses within the joint structure are believed to be a significant antecedent. Driban et al. [18] identified that participation in certain sports such as soccer, distance-running, weight-lifting and wrestling are associated with the development of knee OA likely due to: 1) higher joint loads and, 2) higher incidence of joint injury. Both causes result in what can be considered abnormal stress conditions of the joint. Abnormally high loads clearly result in abnormally high stresses, and joint injury can result in a redistribution of stresses throughout the joint structure resulting in an unnatural (i.e. abnormal) stress distribution. In 2013 Felson [19] argued that abnormal mechanics are a direct cause of OA. Furthermore, it was shown that the presence of abnormal stresses and development of OA results in a cyclic process of joint degradation. As the joint degrades over the course of the disease, the stress distribution evolves to account for changes in the

spatial structure and new articular surface. This redistribution of stresses in turn results further joint damage leading to a vicious cycle of stress redistribution and joint damage, Figure 4.
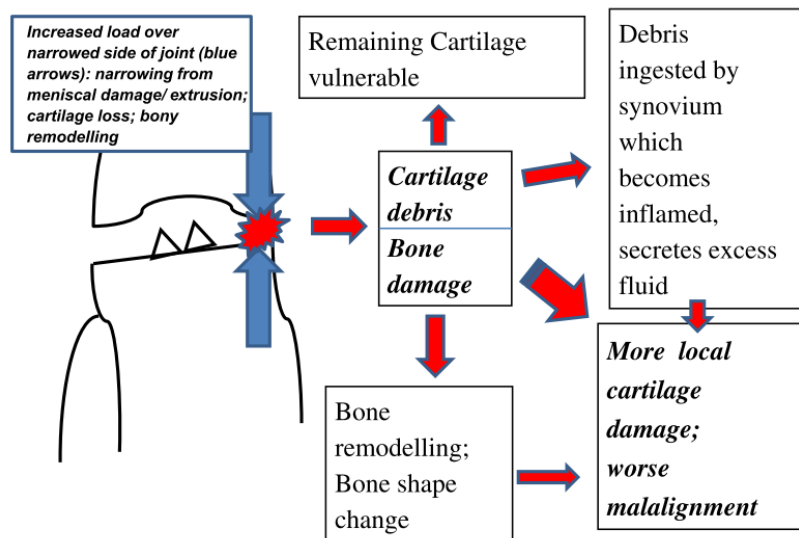
Figure 4: The vicious cycle of joint damage caused by malalignment. Figure and caption taken from Felson [19]

OA is one of the most common diseases in the human population [2]. It is estimated that 55.7 million cases doctor-diagnosed OA existed in 2015 within the United Stated population. That number is expected to rise to 67 million cases by 2030, accounting for 25% of the adult population [20]. With such a high prevalence of the disease, it is expected that 25 million people will have some level of arthritis-attributed activity limitations [20]. Table 1 summarizes predictions of OA in the U.S. from 2005 to 2030 by Hootman et al. published in 2006.

Table 1: Projections of OA in the US. Table adapted from Hootman et al. [20].

Year	Estimated US population, in thousands	Projected prevalence of doctor-diagnosed arthritis, in thousands	Projected prevalence of arthritis-attributable activity limitations, in thousands
2005	216,096	47,838	17,610
2010	227,762	51,879	19,117
2015	238,154	55,725	20,601
2020	247,775	59,409	22,052
2025	257,469	63,209	23,565
2030	267,856	66,969	25,043

Despite the high prevalence and alarming predictions, there are few treatments for OA. For less severe cases, patients are encouraged to exercise, practice physiotherapy and lose weight. The role of pharmacological intervention is primarily directed towards symptom relief consisting of corticosteroid injections at the affected joints and general use of non-steroidal anti-inflammatory drugs. For more severe cases, surgical treatments are used to either change the stress distribution in the joint (i.e. osteotomy) or to completely replace the affected joint with a prosthetic implant [2].

The lack of comprehensive OA treatment has been at least partially attributed to a deficiency in the knowledge of the disease pathology [2]. Current research approaches rely on *in vitro* cell models, which although highlighting cellular and molecular mechanisms, fail to accurately model the three-dimensional structure of joints. On the other hand, the use of *in vivo* animal models does account for the effects of OA within the entire joint structure. However, the development of chronic stress induced OA in laboratory animals is difficult, and typically involves chemical or surgical intervention to promote joint degradation. Such interventions limit the relevance of the models as a method to study OA in humans. A detailed discussion of the advantages, disadvantages and current states of *in vivo* and *in vitro* OA research can be found in [2]

The motivation to develop a novel system to study OA pathology and potential treatments is clear. The proposed research is to develop an *in vitro* system capable of

inducing OA-like pathology in explanted mouse joints. The goal is to effectively develop a knee simulating system capable of dynamically actuating and loading knees in a controlled manner while maintaining viability of the joint capsule and surrounding tissues. The successful development of such a system will allow researchers to investigate both OA pathology and treatments on a mouse model under controlled and known conditions.

2.3 A History of Knee Simulating Systems

The development and use of knee simulating systems is not entirely novel. However, their use in biological and medical relevant applications has been highly limited in the past, and to date, no knee simulators have been reported that maintain viability in explanted joints over extended periods of time. Regardless, it is helpful to consider the history of knee simulating systems.

The use of mechanisms to simulate knee motion and loading has been reported in the literature throughout the past four decades. This section serves to summarize the history of published research where investigators have developed or acquired systems that simulate aspects of natural knee motion and loading. In general, three classes of knee simulators are identified: Oxford style simulators [21-34], robotic arm driven simulators [5, 35-40], and unique simulators [8, 41-57, 63-65]. Unique simulators, simply put, are devices that are not driven by robotic arms and are not of a form-factor comparable to Oxford-style devices. Each class of knee simulators will be discussed in further detail in coming sections. A timeline of major studies involving knee simulation is presented in Figure 5 and a general overview of each study is shown in Table 2.

The majority of past knee simulators have been developed to study human models, using either cadaver knees, cadavers implanted with total knee replacements, or total knee

replacements directly mounted onto the simulation devices. Similarly, the majority of research has focused on measuring and modeling the complex biomechanics of knees and implants, or quantifying the wear and performance of total knee replacements and their constitutive materials. The nature of these studies therefore does not require *living* tissue. In cases where natural knees are studied, research focuses on biomechanical characterization in which the knee is subjected to forces and displacements comparable to those encountered in human activity. The measurement of forces, displacements or strains is typically the output of such experiments. Since these kinds of experiments focus only on the mechanical behavior of the knee joint as a mechanical system and have no interest in determining the biological response of tissues, no effort is made to culture the knee. In many instances defrosted knees from frozen cadavers are utilized as well, leading the assumption that the tissue is effectively dead.

A comparatively small number of systems have been developed to study animal models too. Studies have been performed using *in vitro* bovine [42, 63, 65], *in vitro* porcine [57], *in vitro* murine [64] and *in vivo* murine [52, 53, 55] models. The bovine and porcine modeled investigations focus on investigating cartilage wear due to repeat loading, and in one case the effects of passive motion loading on tissue biology. The research on *in vitro* murine joints focused on measuring joint friction in a cultured stifle. In the case of the *in vivo* murine models, the research goals were to investigate the effects of passive motion loading on tissue following invasive knee surgeries. These represent the only studies found where a knee simulation device is used in a diagnostic or medical capacity and where there is an explicit effort in measuring the biological response. The methodology and mechanisms used in these studies will be expanded upon in coming sections.

Figure 5: Timeline of majors published works related to knee simulators
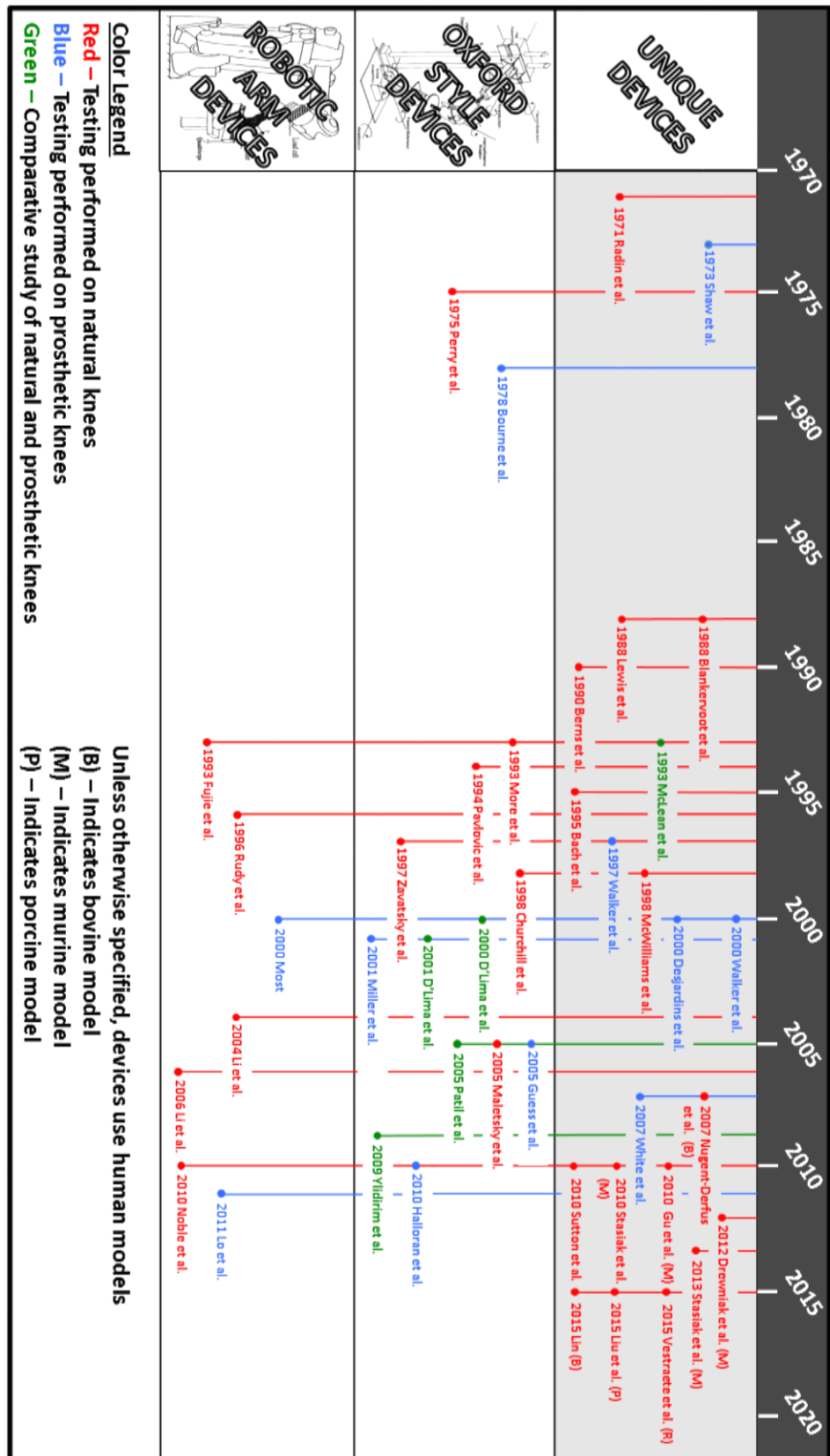
Table 2: Summary of significant published works related to knee simulators (*Study does not report usage on intended specimen)

Year	Author	Animal Model	Specimen Type	Test Specimen Environment	Area of Study	Rig Style
1971	Radin et al. [41]	Bovine	Tissue	Lubricant bath	Cartilage wear	Unique
1973	Shaw et al. [42]	Human	Implant (mounted on cadaver)	Not enclosed	Implant testing	Unique
1975	Perry et al. [21]	Human	Tissue	Not enclosed	Knee biomechanics	Pre-Oxford
1978	Bourne et al. [22]	Human	Implant	Not enclosed	Implant testing	Oxford
1988	Blankervoort et al. [43]	Human	Tissue	Not enclosed	Knee biomechanics	Unique
1988	Lewis et al. [44]	Human	Tissue	Not enclosed	Knee biomechanics	Unique
1990	Berns et al. [45]	Human	Tissue	Not enclosed	Knee biomechanics	Unique
1993	McLean et al. [46]	Human	Implant and Tissue	Not enclosed	Implant testing and Knee biomechanics	Unique
1993	More et al. [24]	Human	Tissue	Not enclosed	Knee biomechanics	Oxford
1993	Fujie et al. [35]	Human	Tissue	Not enclosed	Knee biomechanics	Robotic arm
1994	Pavlovic et al. [23]	Human	Tissue	Not enclosed	Knee biomechanics	Oxford
1995	Bach et al. [8]	Human	Tissue	Not enclosed	Knee biomechanics	Unique
1996	Rudy et al. [36]	Human	Tissue	Not enclosed	Knee biomechanics	Robotic arm
1997	Walker et al. [47]	Human	Implant	Not enclosed	Implant testing	Unique
1997	Zavatsky et al. [26]	Human	Tissue	Not enclosed	Knee biomechanics	Oxford
1998	MacWilliams et al. [48]	Human	Tissue	Not enclosed	Knee alignment	Unique
1998	Churchill et al. [25]	Human	Tissue	Not enclosed	Knee biomechanics	Oxford
2000	Desjardins et al. [49]	Human	Implant	Lubricant bath	Implant testing	Unique
2000	Walker et al. [50]	Human	Implant	Lubricant bath	Implant testing	Unique
2000	Most [5]	Human	Implant	Not enclosed	Implant testing	Robotic arm
2000	D'Lima et al. [27]	Human	Implant and Tissue	Not enclosed	Knee vs. Implant biomechanics	Oxford
2001	D'Lima et al. [29]	Human	Implant and Tissue	Not enclosed	Knee vs. Implant biomechanics	Oxford
2001	Miller et al. [28]	Human	Implant (mounted on cadaver)	Not enclosed	Implant testing	Oxford
2004	Li et al. [37]	Human	Tissue	Not enclosed	Knee biomechanics	Robotic arm
2005	Patil et al. [30]	Human	Implant and Tissue	Not enclosed	Knee vs. Implant biomechanics	Oxford
2005	Guess et al. [31]	Human	Implant*	Not enclosed	Implant testing	Oxford
2005	Maletsky et al. [32]	Human	Tissue	Not enclosed	Knee biomechanics	Oxford
2006	Li et al. [38]	Human	Tissue	Not enclosed	Knee biomechanics	Robotic arm
2007	White et al. [51]	Human	Implant	Not enclosed	Implant testing	Unique
2007	Nugent-Derfus et al. [65]	Bovine	Tissue	Culture medium	Medical	Unique
2009	Ylidirim et al. [33]	Human	Implant and Tissue	Not enclosed	Knee vs. Implant biomechanics	Oxford

2010	Stasiak et al. [52]	Murine	Tissue	*in vivo*	Medical	Unique
2010	Gu et al. [53]	Murine	Tissue	*in vivo*	Medical	Unique
2010	Halloran et al. [34]	Human	Implant	Not enclosed	Implant testing	Oxford
2010	Noble et al. [39]	Human	Tissue	Not enclosed	Knee biomechanics	Robotic arm
2010	Sutton et al. [54]	Human	Tissue	Not enclosed	Knee biomechanics	Unique
2011	Lo et al. [40]	Human	Implant (mounted on cadaver)	Not enclosed	Implant testing	Robotic arm
2012	Drewniak et al. [64]	Murine	Tissue	Culture medium	Knee biomechanics	Unique
2013	Stasiak et al. [55]	Murine	Tissue	*in vivo*	Medical	Unique
2014	Lin [63]	Bovine	Tissue	Culture medium	Validation of culture system	Unique
2015	Liu et al. [56]	Porcine	Tissue	Lubricant bath	Cartilage wear	Unique
2015	Vestraete et al. [57]	Human	Tissue*	Not enclosed	Knee biomechanics	Unique

2.3.1 Unique Simulators

Radin et al. [41] reported the development of one of the earliest knee simulation and testing devices in 1971. The system, shown in Figure 6, was built to investigate the wear properties of cartilage using thawed bovine metacarpal-phalangeal joints. The system was based on a modified anthrotripsometer, a device used to measure the instantaneous coefficient of friction between two surfaces. The knee was maintained in a veronate buffer lubricant bath, with the intent of the simulating synovial fluid present in the natural joint. The authors investigated the effects of combined oscillation, static loads up to 1000 lb and intermittent impact loading on the rate of wear of cartilage. Static load application was accomplished by hanging weights, and dynamic impact loads were realized through a pneumatic cylinder. The experiments were run for up to 500 hours at a time.
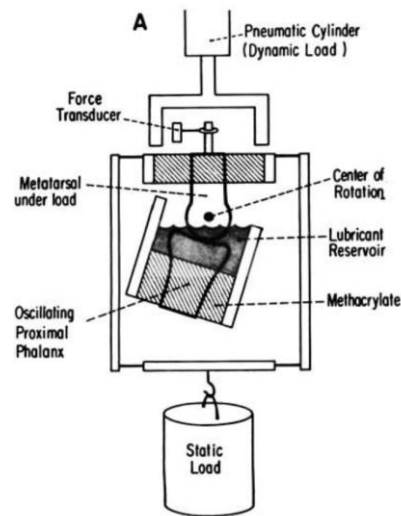
Figure 6: Cartilage wear testing system; an early knee simulation system developed by Radin et al. Figure adapted from Radin et al. [41]

In 1973 Shaw et al. [42] reported on a device used to test total knee replacements installed on human cadaver legs. The system, shown in Figure 7, was developed to simulate the walk gait cycle and was designed based on the understanding that two classes of physiological forces act on the knee: (1) forces transmitted that accelerate the body mass; (2) forces from muscle groups acting on the knee to control motion. The device has effective hip and ankle joints with flexion controlled by a hydraulic cylinder and chain system. Ultimately the device was used to study the effects of tolerance in implant placement and how it affects the mechanics of the joint.
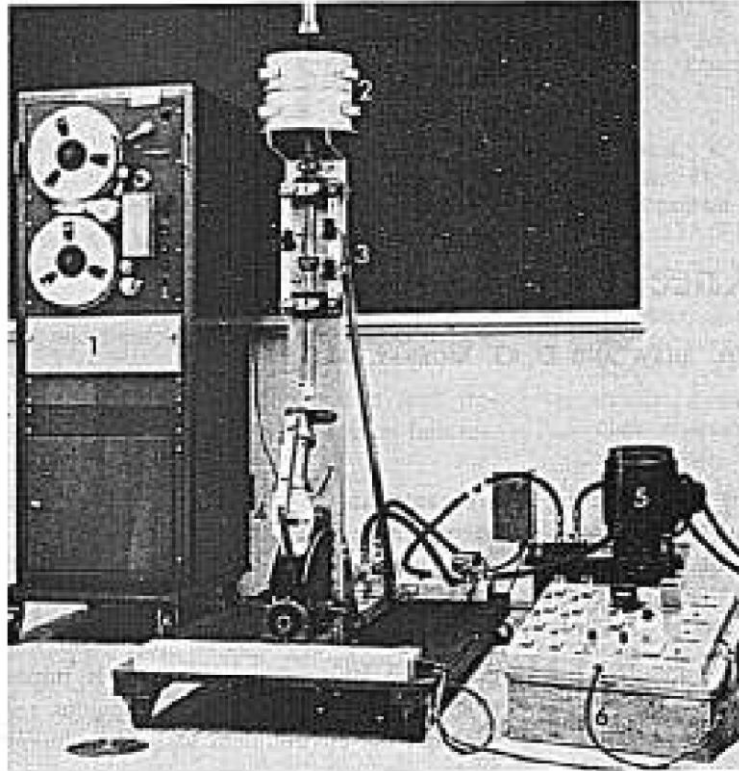
Figure 7: Shaw et al. Knee Joint Simulation: (1) load cell instrument recorder; (2) lead weights; (3) micro-switches; (4) cadaver joint and prosthesis; (5) hydraulic pump; (6) logic control circuitry, Figure and caption taken from Shaw et al. [42]

In 1988, Blankervoot et al. [43] measured the passive envelopes of knee motion. This was accomplished by constructing a system for mounting cadaver knees, which left the joint free in six degrees-of-freedom. By applying external loads and torques to the joint (i.e. tibial torques, axial forces and anterior-posterior forces), the authors were able to measure the passive displacement envelopes of the knee.

In the same year, Lewis et al [44] studied *in vitro* knee ligament mechanics by applying similar external loads to cadaver knees. The developed apparatus is presented in Figure 8. Loading is accomplished with pneumatic cylinders. Ligament forces were measured using buckle transducers, constructed of steel frames instrumented with strain gauges. Three-dimensional joint motion is measured using an instrumented spatial linkage system, consisting of six joints and seven links. Utilizing potentiometers at the joints, the

authors were able to measure the relative angles of the linkage system and derive the
linkage geometry, directly related to the joint geometry.
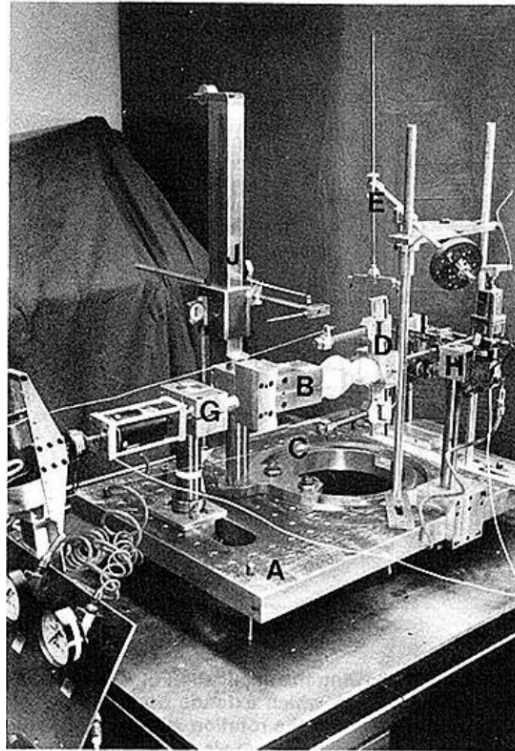
Figure 8: Component parts of load apparatus: (A)-baseplate, (B)-femoral clamp, (C)-dovetail groove allowing flexion of specimen joint, (D)-tibial clamp (E)-counterbalance weight assembly, (F)-control panel for regulators and pressure angles, (G)-joint compression load assembly, (H)-anterior load assembly, (I)-rotational load assembly, (J)-mechanical pointer. Figure and caption taken from Lewis et al. [44].

In 1990 Berns et al. [45] reported on a system to study combinations of loads on the
knee. Shown in Figure 9, the system clamps the tibia and femora and can be used to load
the knee in all axes. The flexion angle is fixed between 0 and 45 degrees and loads can be
applied independently in five degrees of freedom. A system of linear and rotary variable
differential transformers (LVDTs & RVDTs) are used to measure displacements, rotations

and ligament elongation. Using this system, the authors were able to prove that the knee loading response is effectively non-linear with respect to the applied loads. In other words, it is necessary to apply all physiological loads to the joint simultaneously in order to accurately determine the response.
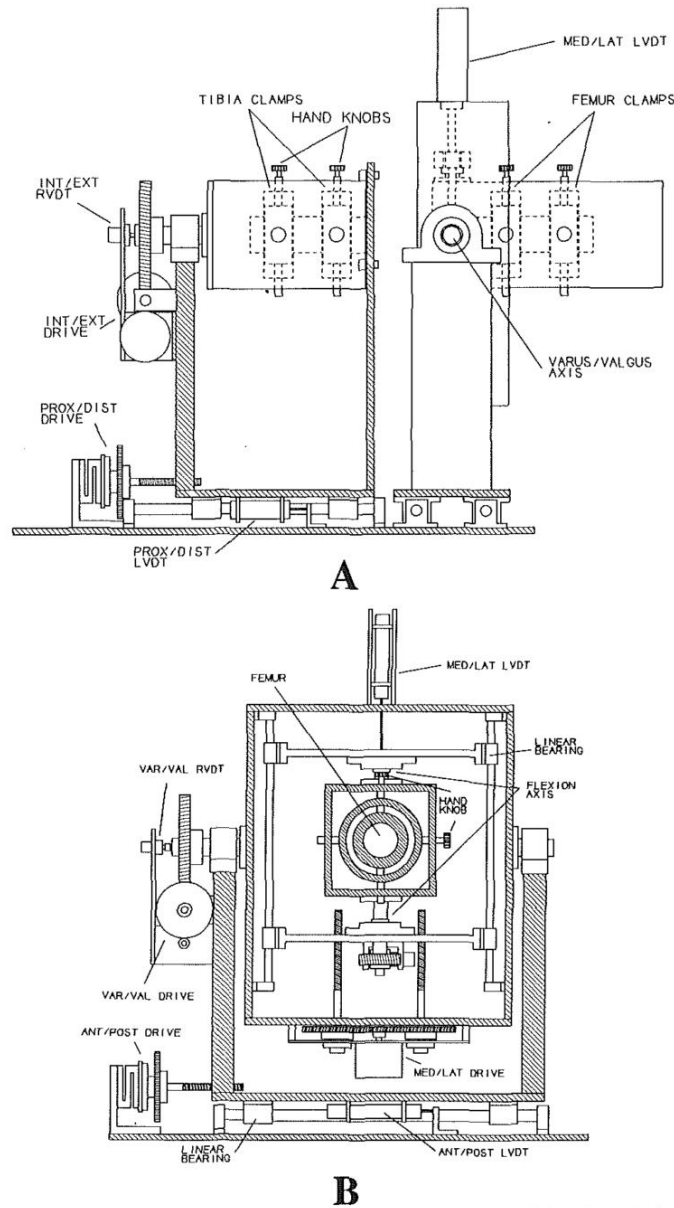
Figure 9: Berns et al.'s knee simulation device schematic showing major components. A. Side view. B. Femoral view. Figure taken from Berns et al. [26]

In 1993, McLean et al. [46] developed a system that simulated the gait cycle for cadaver knees. The system, shown schematically in Figure 10, used hydraulic actuators and stepper motors to apply specified time-histories of the flexion angle, flexion-extension moment, and tibial axial force on the mounted knee. The parameters are controlled using closed-loop feedback to adjust actuator action. The independent control of these three parameters allows for the simulation of multiple activities. The authors tested the system using frozen cadaveric knees and were able to match the human gait cycle with relatively low error.
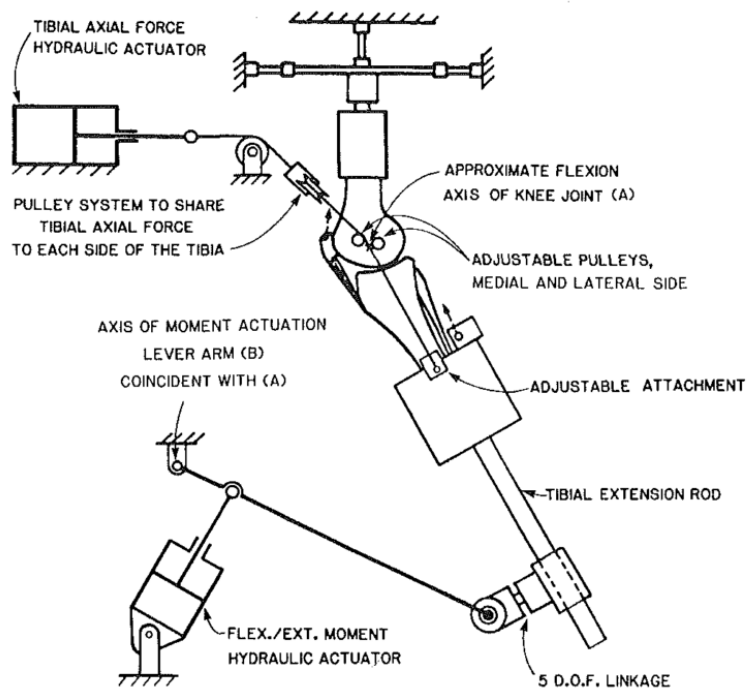
Figure 10: McLean's Knee Actuation System - Developed to simulate gait cycle on cadaver knees. Stepper motors and hydraulic actuators are used to control a flexion angle profile with closed-loop feedback. Figure taken from McLean et al. [46]

In an effort to study ligament injuries seen in skiing accidents, Bach et al. [8] developed a unique system in 1995. Shown schematically in Figure 11, and photographed in Figure 12, the simulator uses linear pneumatic cylinders to apply muscle-like loads to the knee joint in addition to external loads like those described in [46]. Linear actuators apply linear external loads; rotary actuators apply external moments; and a stepper motor controls flexion angle. Strain gauge dynamometers are used measure forces and torques, while an LVDT and RVDT measure displacement and rotations respectively. These measurements are used for closed-loop feedback control of actuators.
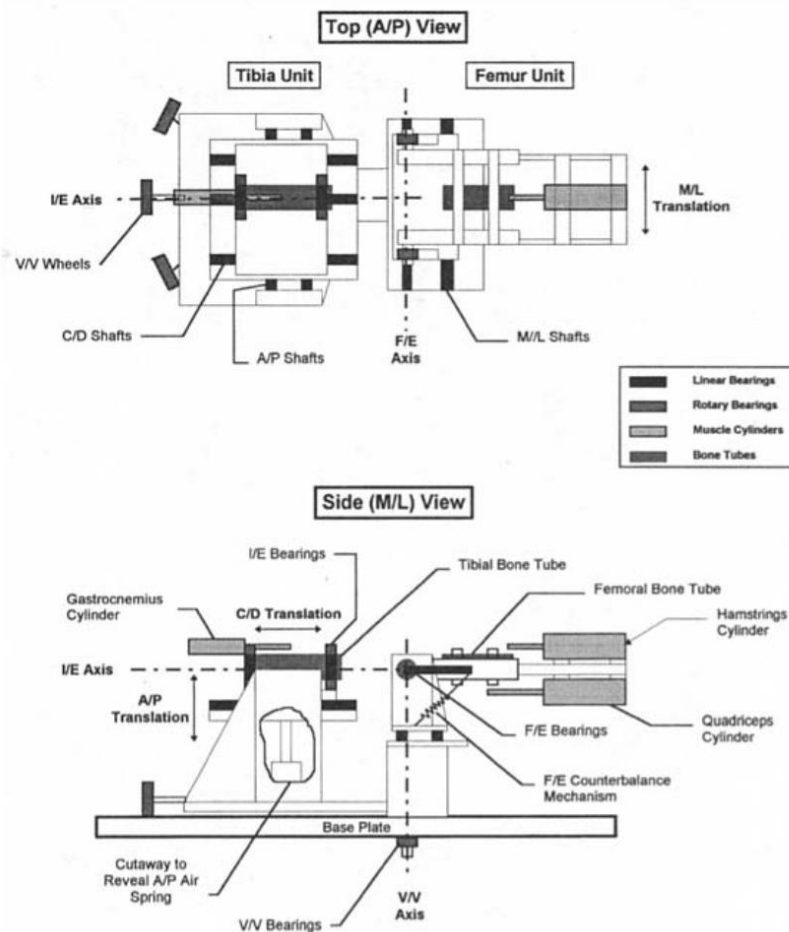
Figure 11: Schematic Representation of Bach et al.'s Device - The system employed additional pneumatic actuators to apply muscle-like loads on the knee. Figure taken from Bach et al. [8].
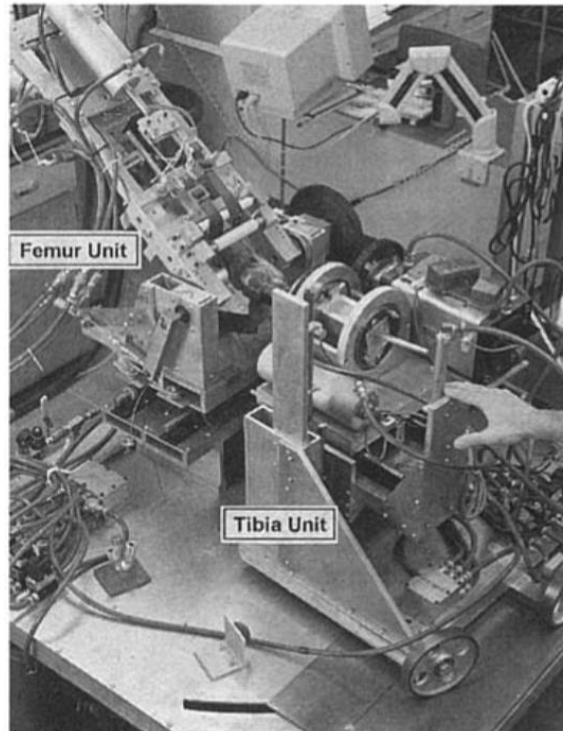
Figure 12: Bach et al.'s Knee Simulator - Figure taken from Bach et al. [8].

In 1997, Walker et al. [47] developed a system for implant testing that did not require the implantation of the replacement on a cadaver, shown in Figure 13. Rather the system applies loads directly to a total knee replacement implant for wear and load bearing testing. The system also attempts to simulate the soft tissue constraints of the *in vivo* environment using elastomeric bumpers. The device controls the axial tibial force, the anterior-posterior force and the tibial moment, similarly to the previous devices discussed. Walker and associated researchers expanded the initial device into a four-station tester used for comprehensive testing of knee implant materials in 2000 [49, 50]. The expanded device, named the Stanmore/Instron KC simulator, is identical to Walker's preliminary device, with the exception that it can run up to four implant test simultaneously and keeps the implant materials in a lubricant bath.
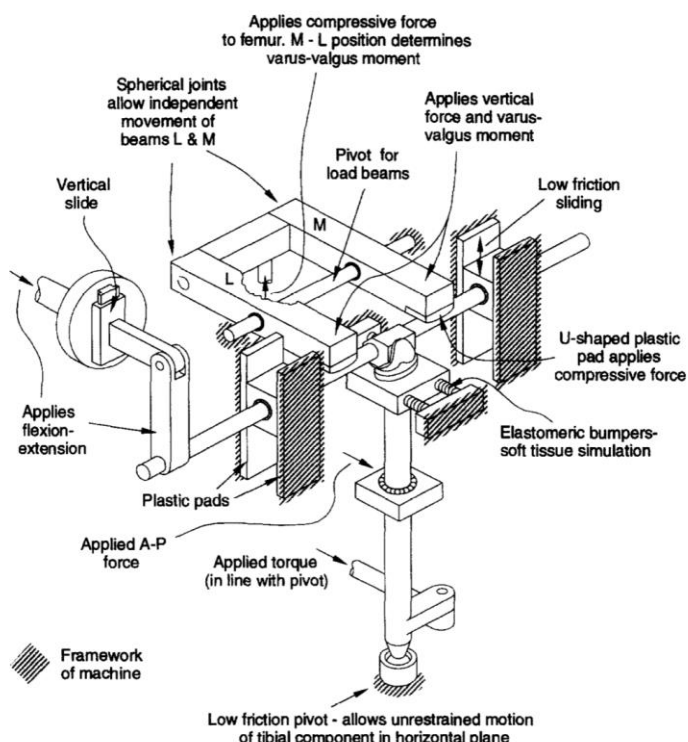
Figure 13: Walker's Knee Simulator for Implant Testing - The addition of elastomeric bumpers simulated the effects of soft tissue constraints. Figure taken from Walker et al. [47].

Walker's device represents an early example of soft-tissue constraints being used to simulate the *in vivo* environment of knee implants. However, given the non-linear nature of biological tissue elastic behavior, the use of linear elastic springs fails to adequately simulate soft tissues. White et al. [51] addressed this issue in 2007, by designing a "virtual soft tissue" controller for knee simulation. The group attempted to capture the non-linear behavior of soft tissue by implementing active force PID control. By referencing look-up tables the pneumatic actuators were controlled to load total knee replacements with soft-tissue like forces which are non-linearly dependent on the physical state of the knee (e.g. flexion angle, tibial rotation angle etc.).

In 1998, MacWilliams et al. [48] identified a significant source of error common to knee simulation systems. The authors claim that alignment of cadaver specimens in knee

systems varies due to variation between knees and human error. The team quantified the amount of misalignment by developing a knee alignment fixture, shown in Figure 14, and repeated alignment of the same knee specimen by five researchers. The group found that the aligned orientations of the tibia and femur varied by 2.2° from the mean, leading up to a 4.7° variation in tibio-femoral rotation during flexion.

Figure 14: Portable alignment jig with knee specimen. Figure and caption taken from MacWilliams et al. [48].

In 2010 Sutton et al. [54] investigated the response of natural cadaver knees to ISO testing standards used for implants. By applying standard loading profiles using a custom-built knee simulator, shown in Figure 15, the authors found that the natural knee's motion deviated significantly from the displacement standards specified by ISO. The simulator

controls flexion angle, anterior-posterior displacement or force, tibial rotation or torque and tibia axial force through closed loop PID control.
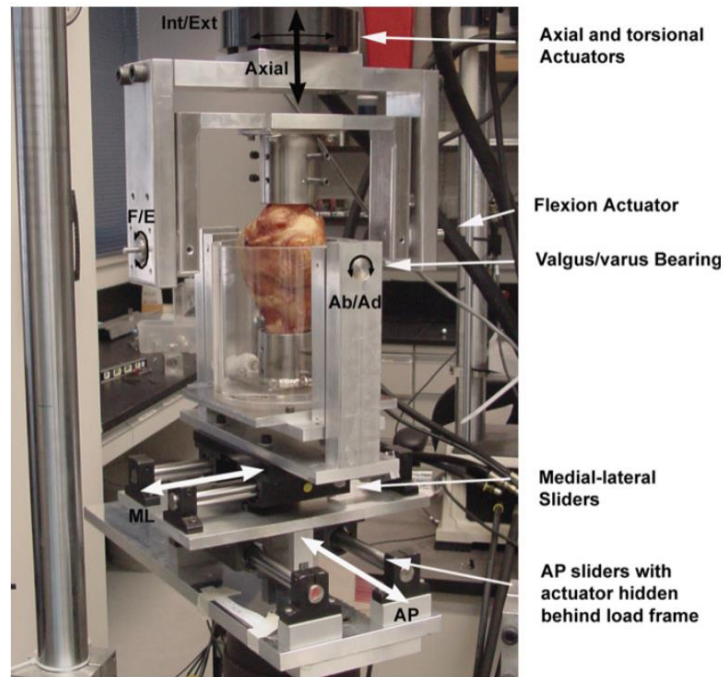
Figure 15: Sutton's Knee Simulator - Mechanism used to test ISO standards for knee implants on cadaveric knees. Figure taken from Sutton et al. [54].

A recent publication by Vestraete et al. [57] in 2015 describes a new knee simulation system. The authors aimed to develop a system that is not limited to simulating a single activity. The design is shown schematically in Figure 16. The device actuates the knee joint by simulating muscle forces with pulley systems engaged by linear servo-motors, while controlling the position of the "ankle". The system simulates the action of hamstrings and quadriceps on the knee. Operation is based on three PID control loops, shown in Figure 17. Using muscle force and ankle position data from the literature, the authors are able to apply controlled motion to a knee analog with relatively low error.
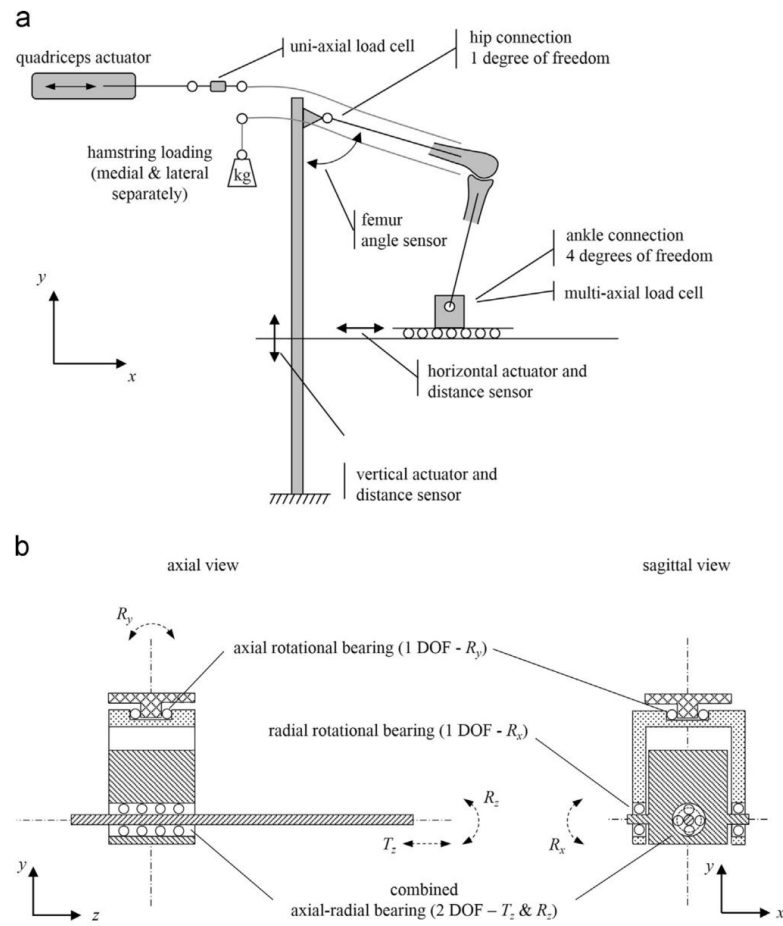
Figure 16: Schematic representation of knee simulator (a) and detail of ankle mechanism (b). Figure and caption taken from Vestraete et al. [57].
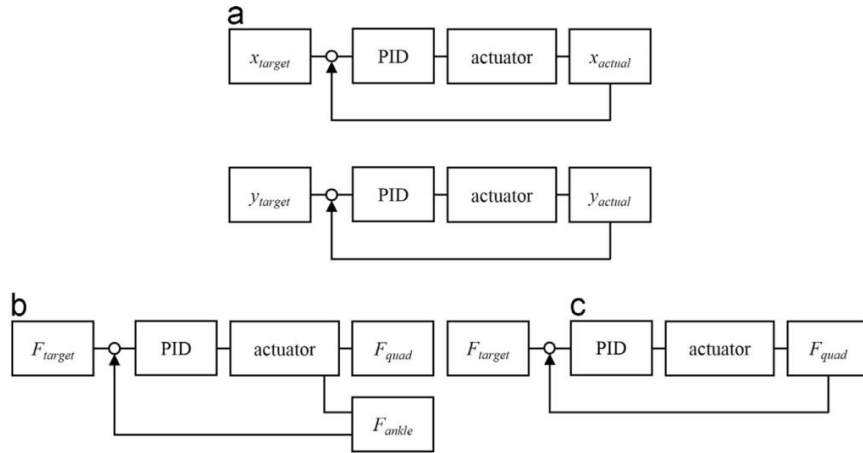
Figure 17: Overview of control loops for ankle positioning (a) and quadriceps actuator with controlled ankle force (b) and controlled quadriceps force (c). Figure and caption taken from Vestraete et al. [57].

Liu et al. [56] reported in 2015 on the use of an industrially manufactured knee simulator to investigate the wear of articular cartilage in porcine cadaveric knees. The group used a knee simulator developed by Simulation Solutions (Figure 18) with the ability to control the axial load force along the tibia, flexion angle, adduction-abduction, anterior-posterior displacement and tibial rotation. In order to investigate the wear properties of the knee specimens, the authors applied both simple and complex loading and motion patterns to the knee (Figure 19).
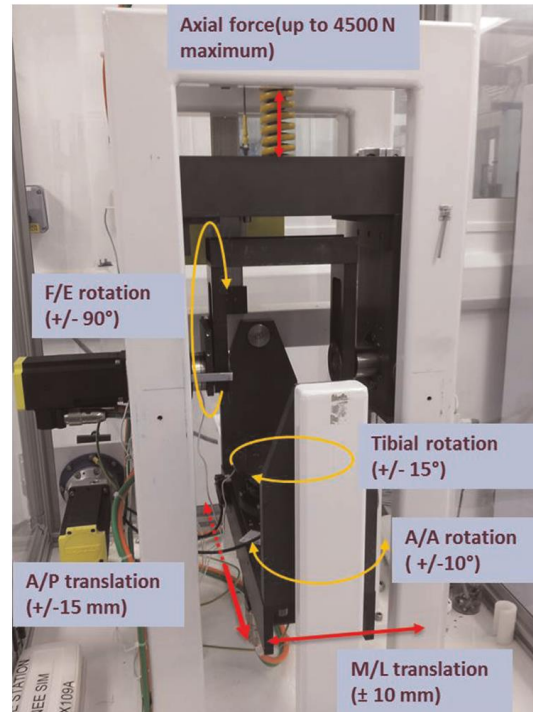
Figure 18: Overview of the single station natural knee simulator. Figure and caption taken from Liu et al. [56]
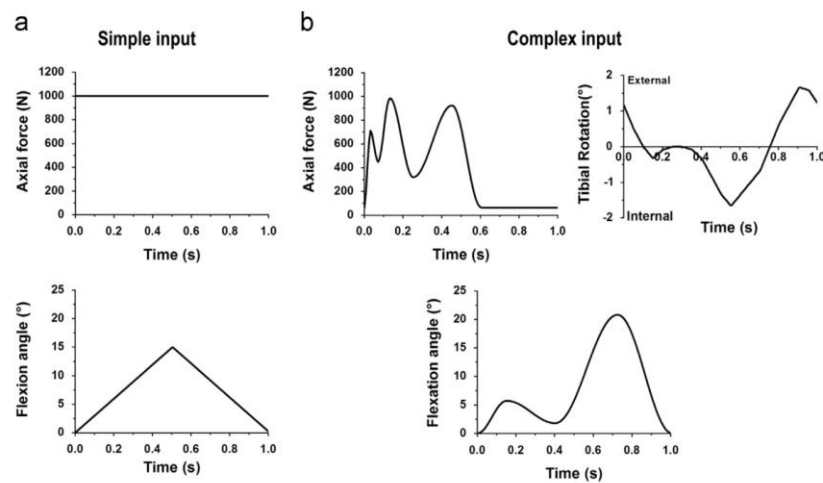
Figure 19:Kinematic input profiles. (a) Simple input profile: a constant load of 1000 N and flexion/extension from 0° to 15° (b) complex input profile: based on a standard dynamic gait cycle and appropriately scaled for a porcine knee joint. Figure and caption taken from Liu et al. [56]

Until recently, with the exception of Radin et al.'s and Liu et al.'s work, unique knee simulators had been developed to study human models for either cadaveric experiments or implant testing. A common goal of the past work summarized up to this point was the characterization of the knee as a mechanical system. Specifically, the wear rates, displacement profiles and ligament strains were measured for knees or implants undergoing activity-like loading or displacement. Such research does not rely on the viability of the knee since it is generally accepted that it has no effect on the knee as a mechanical system. Furthermore, these systems are not designed to simulate knee motion over multiple cycles, since force and displacement readings are assumed to be cycle independent (with the exception of wear studies). However, recent studies focusing on rehabilitation therapy following knee ligament injury have led to the development of *in vivo* knee simulators for rat models which investigate repetitive loading and motion to simulate long-term use of the knee.

In 2010 Stasiak et al. [52] reported on the development of such an *in vivo* knee simulator. Stasiak's device, shown in Figure 20, used a stepper motor-drive linear actuator to drive flexion motion of the knee, while an LVDT provides feedback for position control. A load cell is employed to measure the forces present across the soft tissues of the knee. The intended use of the device was to study the effects of the mechanical stimuli on tendon to bone healing following ACL reconstruction. However, for research purposes, the authors investigated the compliance of the mechanical system. In addition, the authors investigated the general usability of the system by exercising 15 Sprague-Dawley rats at 50 cycles per day for 10 consecutive days. No detrimental effects were noted in the mechanism and the authors concluded that the rats were fully capable of handling daily anaesthetization for the duration of the study.
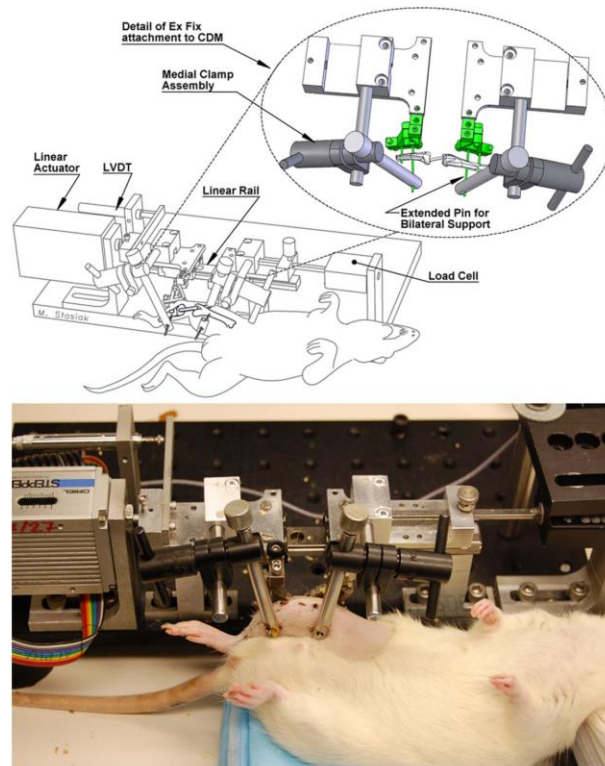
Figure 20 Stasiak's in vivo Rat Joint Loading System – Developed in 2010, the device was used to actuate anesthetized rat knees in vivo. Top: schematic; Bottom: photograph Figure taken from Stasiak et al. [52].

In 2013, Stasiak et al. [55] reported on a redesigned device (see Figure 21). With the same research intent, the revised device includes a rat bed for the animal and the relocation of the load cell to measure horizontal force between the linear actuator and point of contact with the rat (i.e. posterior ankle joint, parallel to the plantar sole). The revised device was used in a pilot study on two Sprague-Dawley rats for a flexion-extension cycle of 100° for 25 cycles a day for 10 days without incident. The team measured the required load to move the knee joint through the desired flexion profile. The resulting load versus flexion angle curves are shown for a single rate over multiple days in Figure 22. The authors account for machine frame stiffness and inertia by subtracting the load required to induce the same motion on the device when no rat is mounted. The results show that a maximum roughly 1.5 N of horizontal force is required to push the rat knee

through the flexion range. The relatively high variation between daily load versus flexion angle profiles is unaddressed by the authors. Since there seems to be no obvious trend (i.e. increasing/decreasing load over consecutive days) the error appears random, likely reflecting difference in the mounting orientation of the rat knee for each loading regiment.
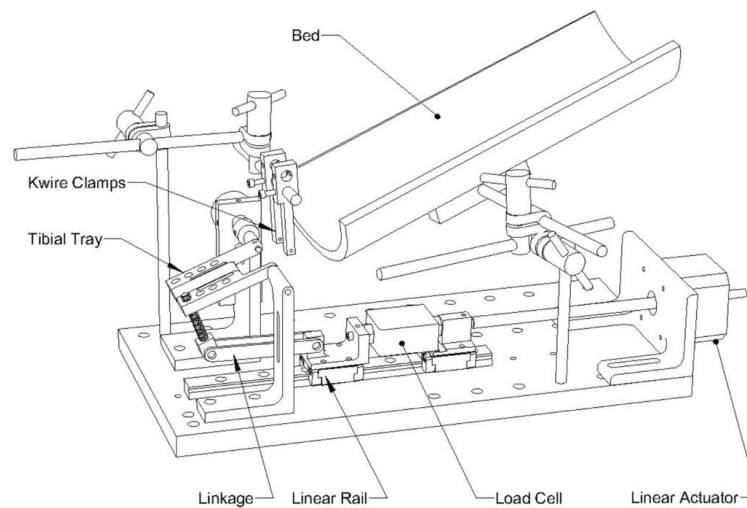
Figure 21: Stasiak's Updated in vivo Rat Joint Loading System – Updated in 2013, the system has the same working principle as the earlier device, but features the addition of a bed for the rats. Figure taken from Stasiak et al. [55]
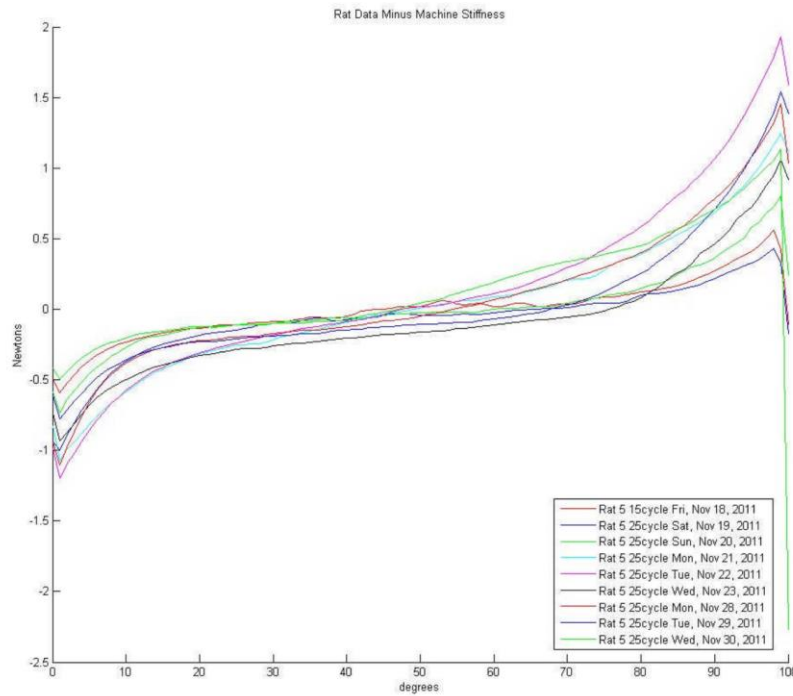
Figure 22: Representative daily load verse flexion angle data from the first rat of the pilot study. The machine stiffness has been subtracted. Figure and caption taken from Stasiak et al. [55].

Gu et al. [53] reported on a similar system in 2010, dubbed the Joint Motion Loading System (JMLS). The device is comparable in function to Stasiak's devices with the exception that it has the ability to apply a constant axial force along the tibial centerline. Shown in Figure 23, the system also uses a linear actuator to drive flexion of the rat knee. An angular encoder is used to sense the flexion angle and closed-loop feedback control is employed to drive the linear actuator to achieve the desired flexion angle time profiles. A constant axial load is applied to the tibia normal to the plantar sole of the rat by miniature springs. The load can be adjusted by a screw and is measured by a miniature load cell.
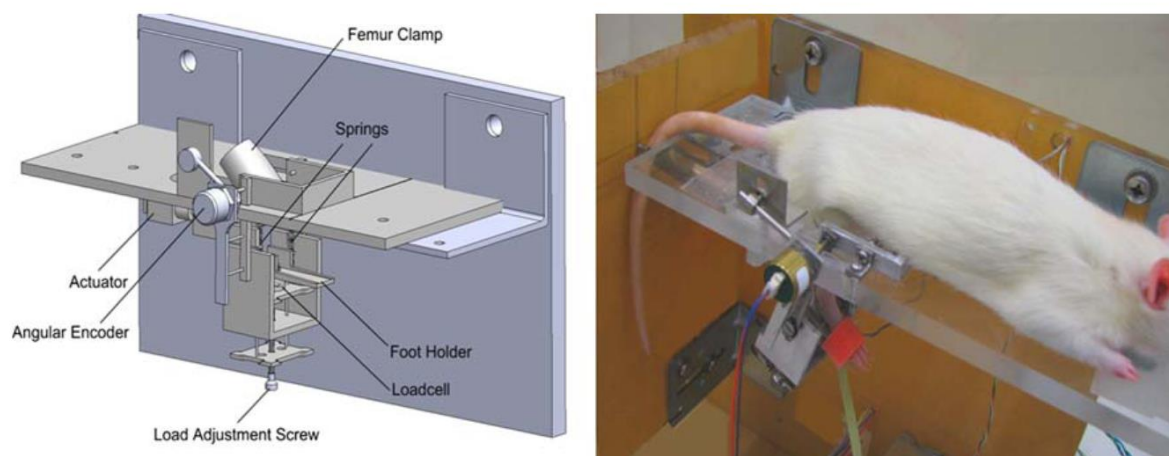
Figure 23: (Left) The schematic diagram of the JMLS design and (Right) Photograph of the experimental setup with an animal undertaking the motion and loading protocol. Figure and caption taken from Gu et al. [53].

Gu and their colleagues' methods and results are rare in the literature in that they relate mechanical motion of the rat knee to the biological response. Following a series of validation experiments on the device, which show that the knee could be driven through a desired flexion profile with relatively low error assisted by the designed control system, the authors investigate the tissue response the joint cartilage when subjected to different loading conditions. The method involved testing five groups of five Sprague-Dawley rats: (1) control group of rats in free cage activity (CTL); (2) a sham control group of rats that were anaesthetized and mounted in the device but not subject to motion or loading (SHAM); (3) an immobilization group where the rats were immobilized in for 6 hours in a cast with the knee at full flexion (115°); (4) a group of anaesthetized rats immobilized for 2.5 hours, driven through flexion from 65° to 115° at 2 RPM for 1 hour and immobilized again for 2.5 hours (PML); (5) a group identically treated as (4) except with axial compressive loading of twice the body weight of the animal, roughly 1 kg (CML). The authors then measure MMP-13 and Collagen II gene expressions in chondrocytes extracted from the knee joint of each rat. The results, shown in Figure 24, suggest that the

PML condition is similar to the natural free activity of the rats. Additionally, the SHAM, IMM and CML conditions all result in a catabolic state of the cartilage, indicating that the articular structure begins to breakdown.
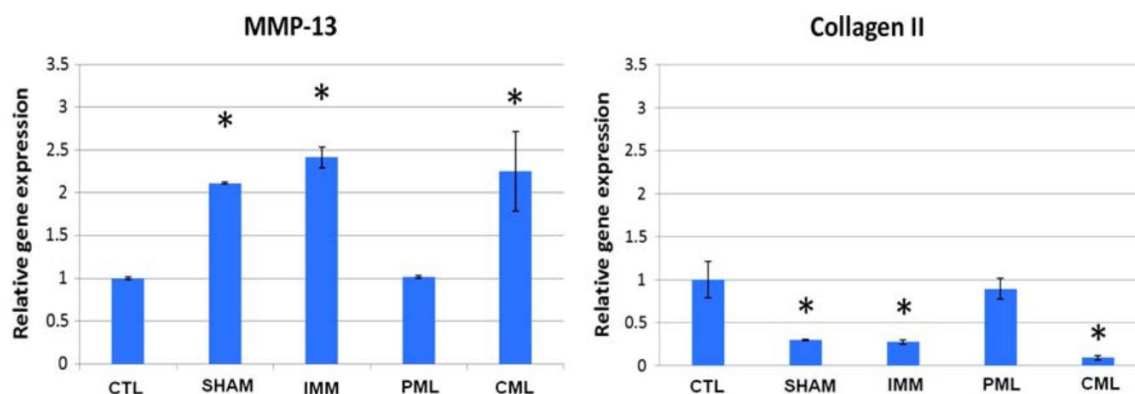
Figure 24: Gene expressions of pro-inflammatory effector MMP-13 and major structural protein in cartilage Collagen II in response to immobilization (IMM), moderate passive motion loading (PML), and compressive motion loading conditions (CML). The results showed that IMM and CML groups exhibited an up-regulation of MMP-13 and a down-regulation of Collagen II, while PML reversed the catabolic responses caused by immobilization by showing reduced gene expression of MMP-13 and increased gene expression of Collagen II. Figure and caption taken from Gu et al. [53].

In parallel with the development of systems for *in vivo* models, several researches have realized systems based on culturing explanted joints for *in vitro* study. Such systems are perhaps the most relatable the presented research and goals. Although these systems share similarities with the work presented in this dissertation, their intended uses and capabilities are not in-line with our goals.

In 2007 Nugent-Derfus et al. [65] presented a bioreactor system for the culture and locomotion of whole bovine stifle joints. The system, shown in Figure 25, was used to investigate the effects of continuous passive motion (CPM) on chondrocyte proteoglycan 4 (PRG4) synthesis in an effort to understand the benefits of rehabilitative activity. As an *in vitro* model, the explanted joint was cultured and actuated for 24 hours. Culturing was

achieved by maintaining the joint in a flexible enclosure and circulating Dulbecco's modified Eagle's medium (DMEM) through the enclosure.
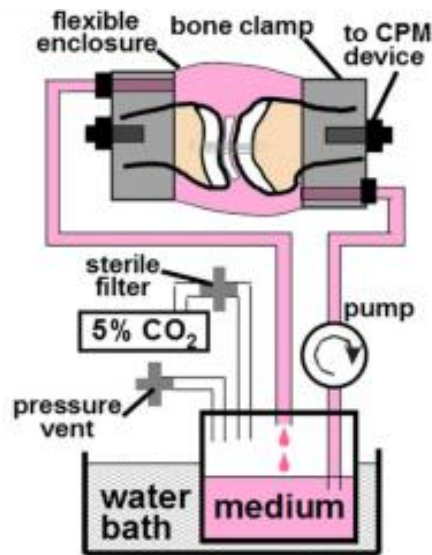
Figure 25: CPM bioreactor system for whole joints. Schematic of system for maintaining tissue-culture conditions during CPM stimulation of the joint. Figure and caption adapted from Nugent-Derfus et al. [65].

Drewniak et al. [64] reported on a system in 2012 used to investigate the frictional properties of mouse stifle joints. The system is based on a pendulum style design, Figure 26, where the explanted joint is mounted in a custom block and a hanging weight can be used to swing the femur relative to the tibia. By measuring the motion profile of the pendulum after release from an initial angle, the research group was able to quantify the friction between the femoral and tibial mating surfaces. Using a modified system, as seen Figure 26B, the stifle was also actively actuated using a DC motor and linkage system connected to the pendulum arm. During actuation, the explanted joint was cultured in DMEM over a period of up to 26 hours. The purpose of actuation was to investigate the

effects of continuous motion on the friction within the joint, with the group showing that the cyclic driven motion resulted in a measurable increase of friction.
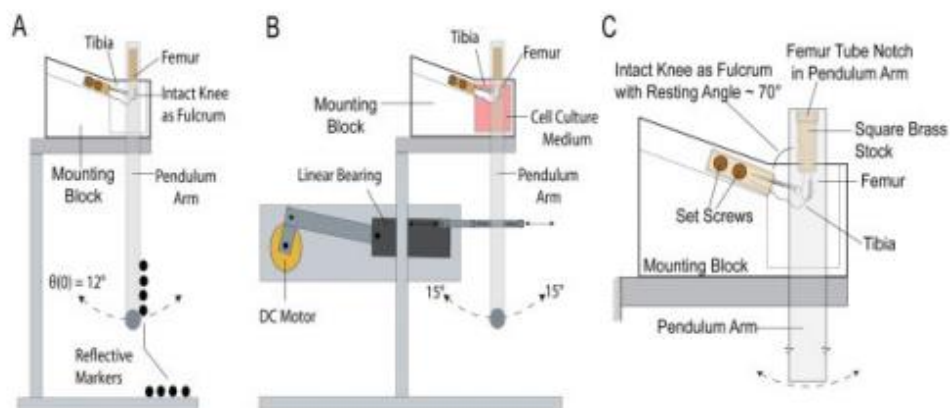
Figure 26: Schematic diagrams of the 2 pendulum systems used in the experiment. A) Passive pendulum system used to measure the coefficient of friction. B) Active pendulum system used for cyclic loading. C) Illustration of how each mouse knee joint was positioned in the mounting block. Figure and caption taken from Drewniak et al. [64]

Both Nugent-Derfus et al.'s and Drewniak et al.'s systems are unique in their ability to culture explanted joints *in vitro.* However, neither system demonstrated the ability to culture tissues over an extended period time as necessary for the study of OA, with maximum culture times of 24-26 hours reported in each study. An effective system for OA investigation requires culture and actuation periods of at least a week to reliably model the long-term effects of motion and loading.

A dissertation completed in 2014 by Lin [63] addresses this issue. Lin presented a project on the development of a long-term joint culture system using Bovine metatarsophalangeal joints. The developed system was able to culture joints and demonstrate viability for up to 4 weeks under various conditions. The dynamic system was fabricated as shown in Figure 27, consisting primarily of components scavenged from

existing systems. Lin's work primarily focused on demonstrating the validity of the system as a culture mechanism and demonstrated that dynamic actuation resulted in superior chondrocyte viability after 4 weeks when compared to a static culture.
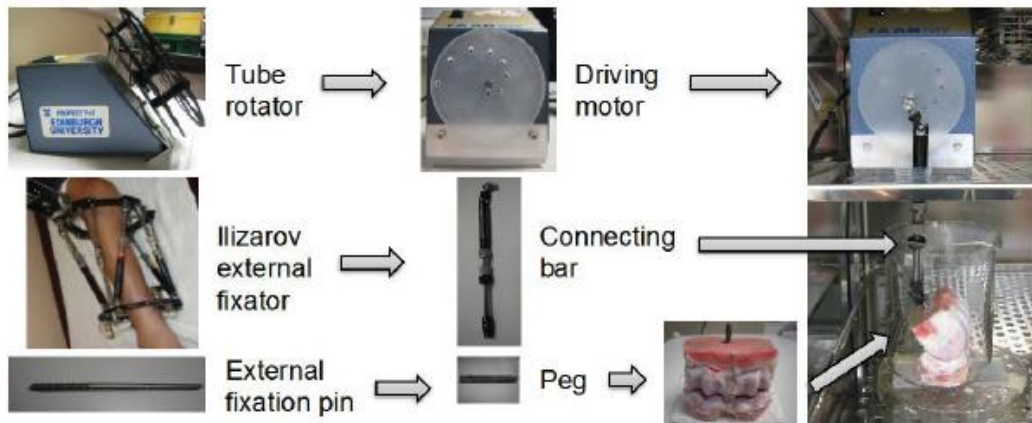
Figure 27: Breakdown of Lin's Dynamic Joint Culture System. Figure taken from Lin [63]

Lin's work is valuable in demonstrating that a dynamic culture can be used to effectively maintain viability in an explanted joint. However, the system cannot be adapted for the needs of studying OA in a mouse model. The size scales between the bovine metatarsophalangeal joints and murine stifle joints are not comparable. Furthermore, Lin's system only demonstrates ability to maintain viability, but does not look into the control repeatability of the mechanical motion and forces at the joint interface. Such factors must be tightly controlled for in a system to study OA, given their known contributions to OA development.

Despite the wide range of form factors, sizes and scopes-of-use of the discussed unique knee simulators, none can be directly modified to suit the needs of our research objectives. In addition to unique simulators, there exist two classes of knee simulating

devices commonly reported in the literature. The following two sections will summarize the Oxford-style simulators and robotic arm driven simulators.

2.3.2 Oxford-Style Simulators

The Oxford rig was a knee simulating system first realized in 1978 at Oxford University, U.K. by Bourne et al. [22], as an improvement of a knee simulator designed in 1975 by Perry et al. [21]. Although initially used by Bourne to study knee implants, it has been recreated and rebuilt by various researchers in the international community for investigation of both implant and natural knee mechanics. This section serves to summarize major works done using Oxford-style simulators.

The general structure of an Oxford-style simulator is shown in Figure 28. The rig simulates the flexed-knee stance, similar to that encountered in activities such as cycling, rising from a seated position, squatting or stair climbing [26]. The knee is generally unconstrained in six degrees of freedom. These styles of simulators consist of two primary components: an "ankle" and a "hip". The ankle assembly provides free spherical motion for the tibia, namely: flexion-extension, adduction-abduction, and tibial rotation. The hip assembly allows for flexion-extension and adduction-abduction of the femur about the hip joint. The hip assembly may also be vertically displaced. The uniqueness of the Oxford rig and similar simulators is that for a determined vertical height, the knee can be perfectly balanced and remain in a mechanically stable position, allowing for static studies of knee mechanics. By actuating vertical motion of the hip assembly one can simulate activity cycles of the knee and study the dynamic mechanics of the knee. The versatile nature of the system has allowed researches to investigate various facets of natural and prosthetic knee behavior under different conditions.
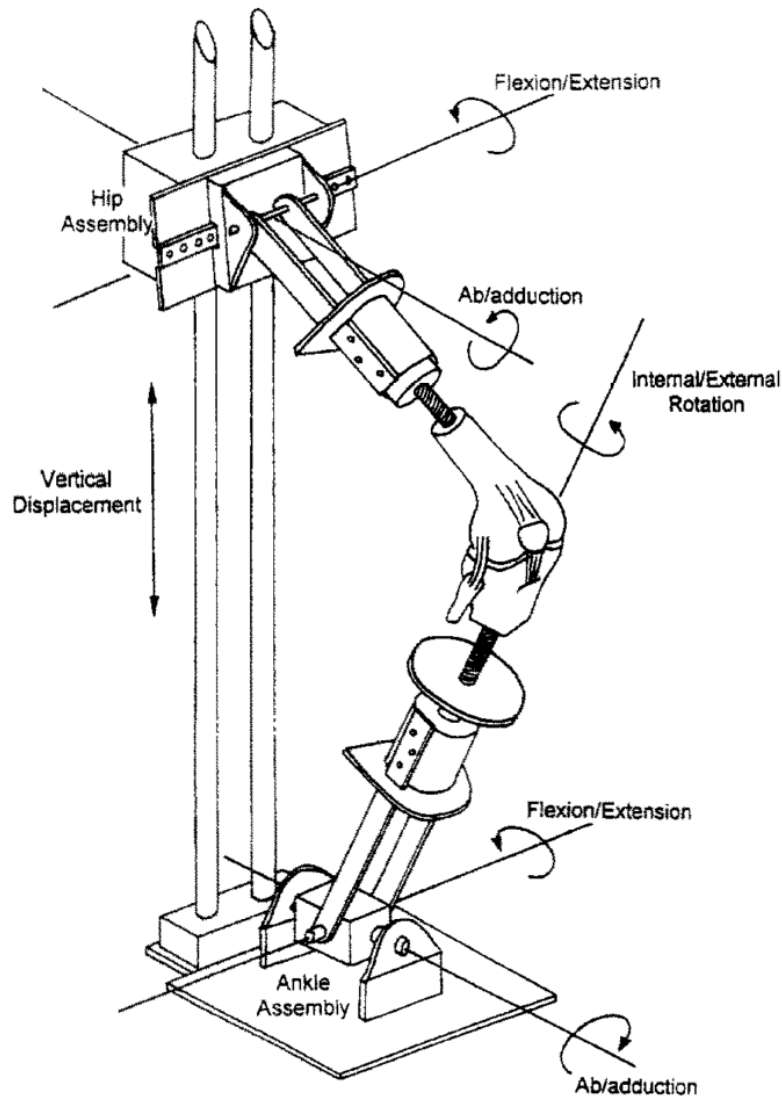
Figure 28: The Oxford Knee-Testing Rig. The ankle assembly allows flexion/extension, abduction/adduction, and internal/external tibia1 rotation. The hip assembly allows flexion/extension and abduction/adduction. In addition, the hip assembly can move vertically relative to the ankle assembly. Figure and caption taken from Zavatsky et al. [26].

Bourne's initial experiments with the original Oxford rig involved testing knee implants mounted in a fixed-flexion stance and loaded with weights. In other words the system was not dynamically actuated. Throughout the 1980's, various researchers had modified the system and used it to research natural knee mechanics such as tibial rotation,

pressure distributions in the joint contact areas, the effects of quadriceps force and the effects of external loads [59-62]. By 1989, Povlovic et al. [23] had developed their own Oxford-style system, complete with an actuated hip joint and muscle (hamstring and quadriceps) force simulators. Their device is shown in Figure 29. Muscle forces are applied using servo-pneumatic actuators, while translations are accomplished using servo-electric actuators.
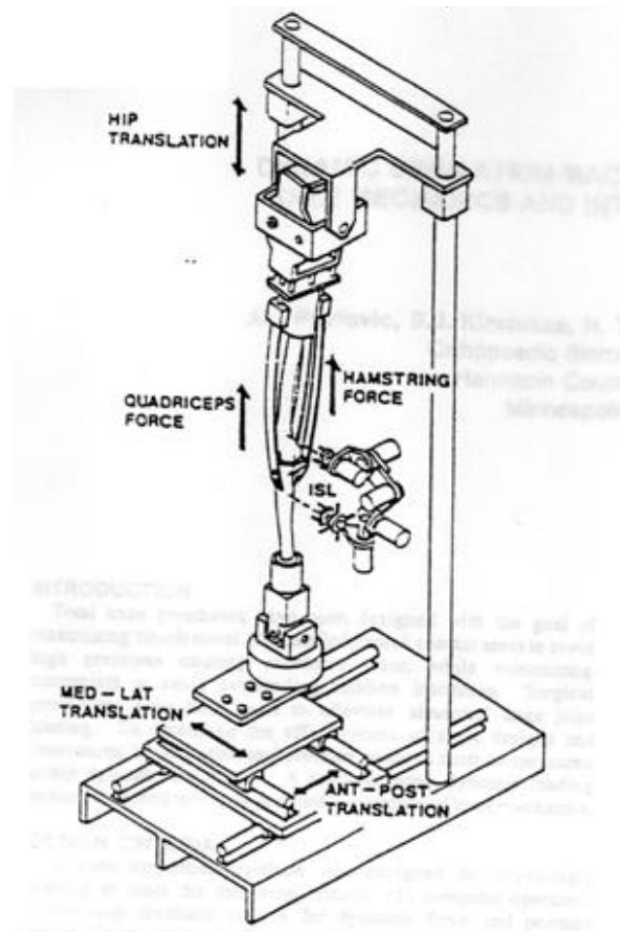
Figure 29: Oxford-style Simulator with Muscle Actuation. – Addition of servo-pneumatic actuators to the Oxford model gives the ability to apply muscle-like actuation profiles. Figure taken from Pavlovic et al. [23].

The addition of muscle actuators has allowed multiple researchers to investigate the effects of muscle action on natural knee dynamics using cadavers. More et al. [24] studied the effects of hamstring loading on femoral rollback and tibial rotation. Churchill et al. [25] investigated the effects of combined hamstring and quadriceps loading on tibial rotation. Similarly, researchers have used the system to investigate the dynamics of knee replacements, typically implanted on a cadaver leg [28]. Guess et al. [31] developed the Kansas Knee Simulator, Figure 30, (used in 2005 with an analog knee [31], and 2010 with implants [34]) and Maletsky et al. [32] developed the Purdue Knee Simulator, Figure 31, both based on the Oxford rig, to study knee implant mechanics. Finally, Oxford-style systems have allowed for several comparative studies between natural cadaver knees and prosthetic fitted cadaver knees [27, 29, 30, 33].
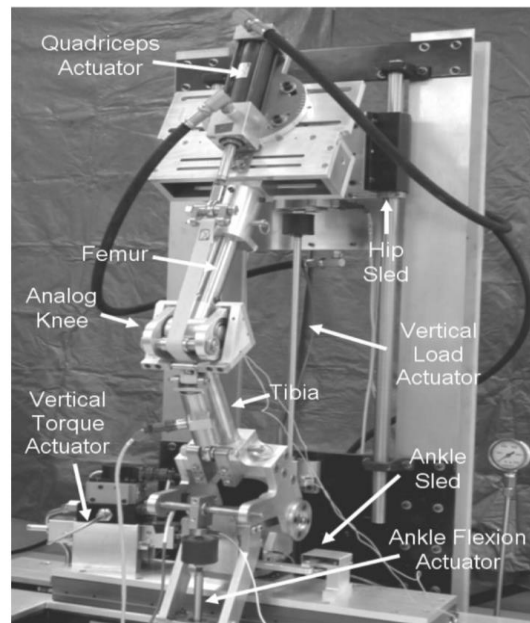
Figure 30: Kansas Knee Simulator – A variation of the Oxford system. Figure taken from Guess et al. [31].
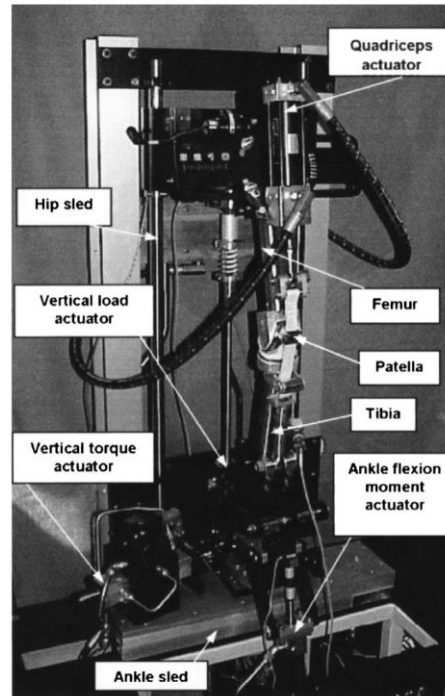
Figure 31: Purdue Knee Simulator – A second variation of the Oxford system. Figure taken from Maletsky et al. [32]

Oxford-style knee simulators are generally accepted as effective tools for investigating certain conditions of knee mechanics. Through modification, researchers have simulated squatting, cycling and walking motions. The development of active force and displacement control as well as muscle action simulation makes these systems attractive for researching knees under numerous conditions. However, there are obvious limitations: (1) Oxford-style rigs cannot be easily modified to investigate knees in an enclosed environment, preventing any investigation of *ex vivo* specimens or researching the biological response of tissues; (2) this simulator style is unsuitable for smaller animal models as down-scaling the system is impractical. Ultimately, the primary use of these simulators is in the study of human model knee biomechanics.

2.3.3 Robotic Arm Simulators

In parallel with Oxford style knee simulators, researchers have developed systems that use robotic arms to manipulate cadaveric knees, either with natural knee joints or implanted with prosthesis. The introduction of commercially available robotic arms in the early 1990's allowed researchers to begin assessing their ability as knee simulators. Robotic arms are attractive because they can provide force, torque or displacement control in six degrees of freedom at the gripper location. Furthermore, their commercial accessibility and relative ease of use has allowed investigators to forgo the process of designing, fabricating and characterizing custom fixtures.

The first reported study utilizing a robotic manipulator for knee simulation was performed by Fujie et al. [35] in 1993. The group used a commercially purchased robotic arm (Mitsubishi Electric, RV-MIS-P2) in concert with a universal force sensor to manipulate a knee. The set up is shown in Figure 32. By clamping the femur and tibia, the knee was maintained at a flexion angle of 30° and loaded in a physiological manner in force-control mode to induce anterior-posterior translation at the joint.
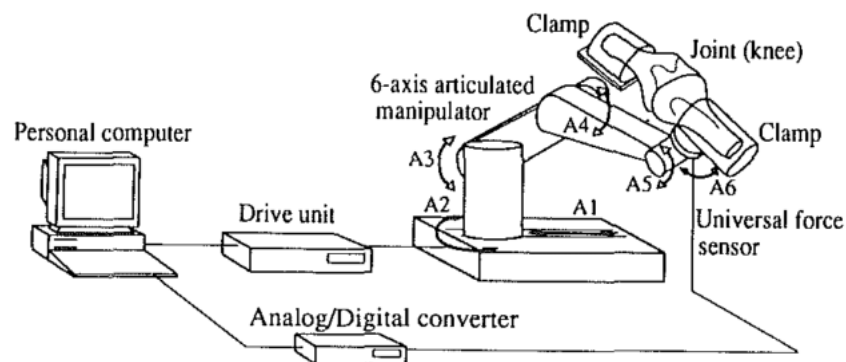
Figure 32: Robotics system as used to test a human cadaveric knee (A1, A2, A3, A4, A5, and A6 are the axes of the manipulator). A closed feedback loop for position and force control (hybrid control) was employed. Figure and caption taken from Fujie et al. [35].

Further work on investigating knee kinematics using robotic manipulators and a similar set up was reported in 1996 by Rudy et al. [36]. In 2004 and 2006 Li et al. [37, 38] published results of experiments utilizing a robotic arm to knee kinematics at high flexion angles and the effects of ACL reconstruction of knee kinematics. Li's system is unique in that it utilized hanging weights to simulate hamstring and quadriceps force (Figure 33). Although not used as extensively, some researchers have applied this approach to investigation of knee implants [5, 21].
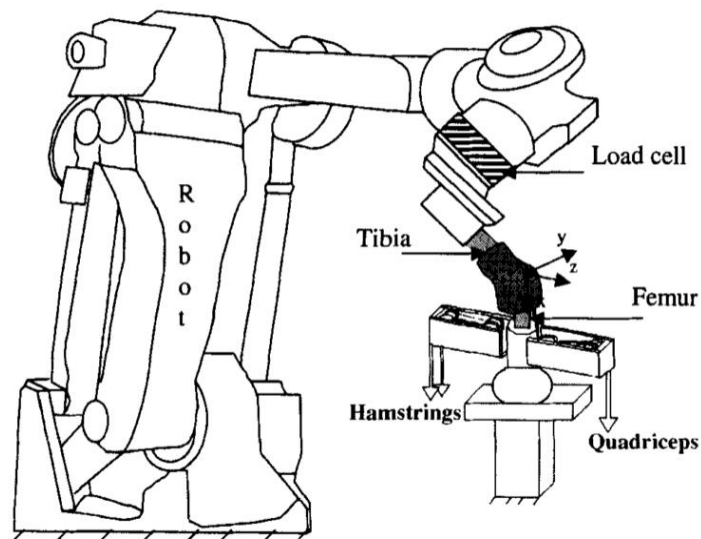
Figure 33: Li et al.'s Robotic Arm Manipulator – The set-up was used for knee simulation researching quadriceps and hamstring loads. Figure taken from Li et al. [37].

Similar to the Oxford-style systems and majority of unique systems, robotic arm driven simulators have been primarily used as a means to study knee mechanical actions. To date, no works has been found that neither utilizes a robotic arm on non-human knees, nor under conditions capable of maintaining tissue viability.

2.4 Conclusions

Overall the field of knee simulators has been dominated by research into systems designed to study the knee joint as a mechanical system. The knee is effectively subjected to mechanical inputs and the resulting mechanical outputs are measured. These have tended to include the impartment/measurement of stresses, forces, torques, rotations and displacements. Such a model ignores the knee as a biological system and the effects of biological, chemical and environmental inputs in favor of defining the mechanical parameters of the knee (Figure 34A). Such a model is valid in considering the pure mechanics of the knee; however, when considering OA pathology it is imperative to consider the knee as a complexly coupled mechanical and biological system, where mechanical inputs can result in biological responses (Figure 34B).
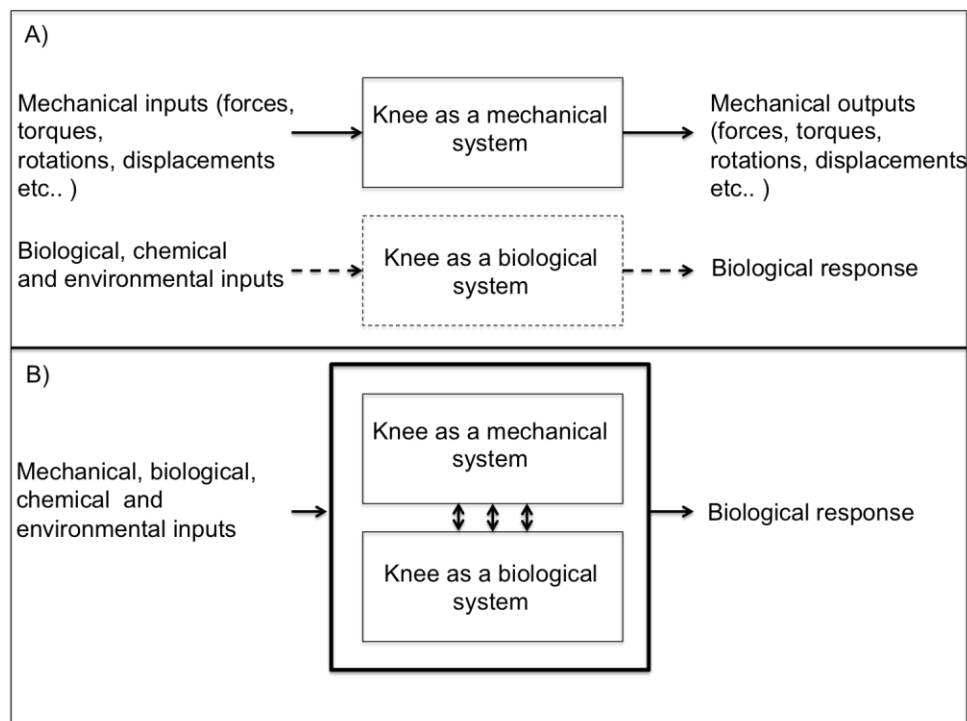
Figure 34: The Knee as a Coupled Mechanical and Biological System - A) The segregation of the knee as a mechanical system and biological system considered in traditional knee simulators; B) The consideration of the knee as a coupled mechanical and biological system, necessary when considering the pathology and treatments of OA.

The presented research demonstrates the development a system and methodology to study the knee as this coupled model. Essentially, the effects of combined mechanical, biological, chemical and environmental inputs can be examined for their effects on the development of OA-like damage of the knee joint, an inherently biological response.

3

First-Generation Joint-in-Motion System

3.1 Introduction

In order to develop a reliable system to model and study OA in a murine model, initial investigation was conducted using a preliminary device. Dubbed the First Generation Joint-in-Motion system, or JM1, the device was initially developed as a prototype by Dr. Thomas James, at the time a professor in the Tufts University Department of Mechanical Engineering, and Dr. Li Zeng, a professor in the Tufts University Sackler School of Graduate Biomedical Sciences. Although this initial device presented several limitations, this prototype was used to perform numerous preliminary experiments to determine suitable culture conditions.

The purpose of this chapter is to describe the design and use of the JM1. The following subjects will be addressed:

1. Mechanical design of the JM1.

2. The supporting hardware and software components.

3. Analytical modeling of the device with the goal of evaluating the mechanical state of mounted joints.

4. Experiments aimed at determining an appropriate concentration of glucose in the culture medium.

5. The limitations of the system.

The JM1 proved useful as a prototype device for initial experiments. However, the limitations of the system prove that it cannot reliably achieve the research goals. Regardless, the system is presented here because it was an effective stepping-stone in the development of the more robust system, presented in Chapters 4 & 5.

3.2 JM1 System Overview

3.2.1 Mechanical Design

The JM1, shown in Figure 35, was designed to flex and extend an amputated murine stifle joint through a predetermined range of motion, while keeping the joint submerged in a reservoir containing culture medium. The system consists of a medium reservoir attached to a backing plate. A servomotor (SG9 Micro Servo, TowerPro) is used to actuate the joint through action of a wire. Upon explantation, the femur is mounted into the bottom anchor by a marine adhesive (Fast Cure 5200, 3M, MN, USA). The bottom anchor is rigidly attached to the base of the system on the lower plane of the reservoir. The tibia is mounted to the top anchor using the marine adhesive. A full mounting configuration is shown in Figure 35C, and a fully set-up device is shown in Figure 35D.
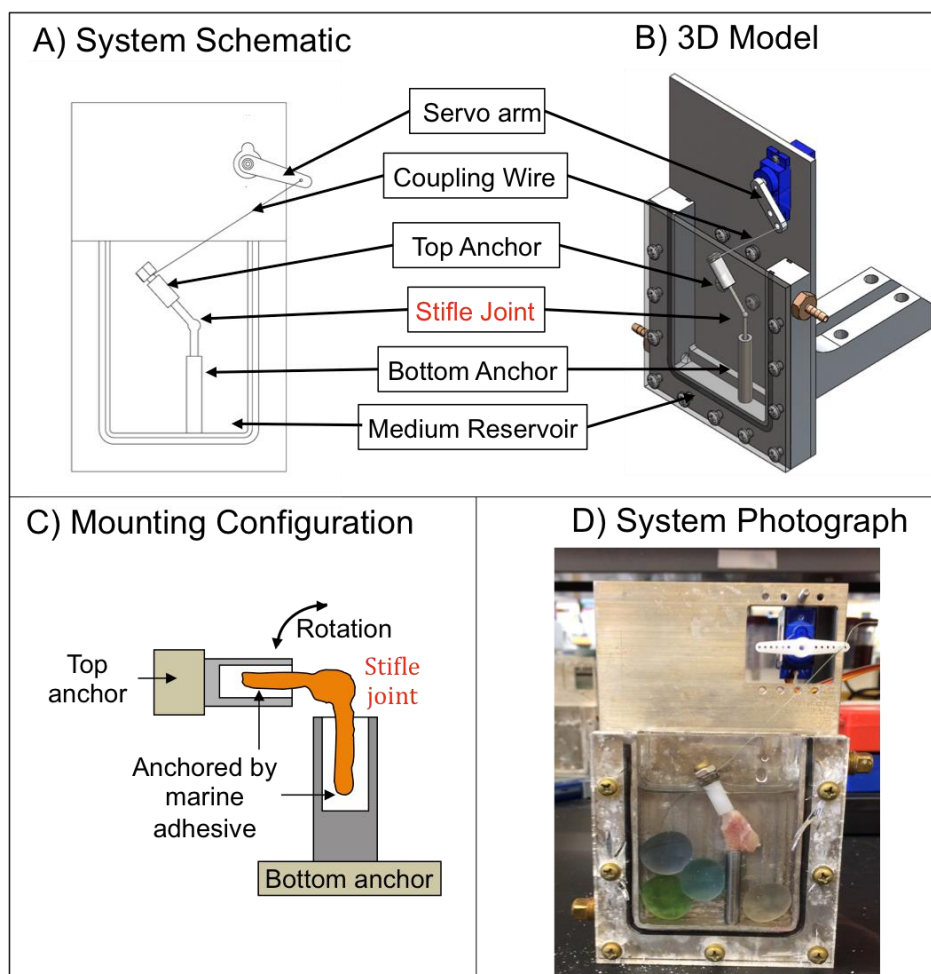
Figure 35: JM1 System - The first generation device used to actuate amputated mouse knees. The rocking motion of the servo arm is used to flex and extend the knee joint through the action of a coupling wire. A) 2D Schematic; B) CAD model; C) Mounting Configuration; D) Photograph of system with stifle joint mounted

Overall the device measure approximately 15x10x4 cm in size. The backing plate and reservoir are custom fabricated from 6061 aluminum. The reservoir is enclosed by a custom fabricated clear acrylic front plate. An O-ring seal (9407K21, McMaster-Carr, NJ, USA) is fitted between the front plate and mating reservoir surface to prevent culture medium leakage. An unmodified 18-8 stainless steel 1.25" long 6-32 unified course (UNC) female-threaded standoff is used as the bottom anchor (91125A230, McMaster-Carr, NJ, USA), and an unmodified nylon 0.5" long 6-32 UNC female-threaded standoff used as the top anchor (96110A570, McMaster-Carr, NJ, USA). The device is supported

by an L-bracket on the rear side of the backing plate. The reservoir is also designed with two fluid valves for the option of circulating culture media. However, these valves were not utilized and remained sealed for all experiments.

3.2.2 JM1 Hardware and Software Support

In order to actuate the system, an Arduino Uno microcontroller is used to control the servomotor. The system does not provide any state feedback so all control is performed in open-loop, with the controller scheme diagramed in Figure 36.
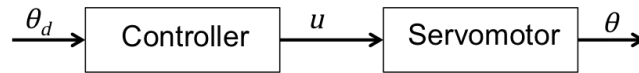
Figure 36: JM1 Controller Scheme - The system is controlled in open-loop with no feedback. The controller drives the servo motor to a desired angular position that is updated regularly to result in a continuous motion of the servo arm.

The controller scheme is based on intermittently updating the desired angular position, θ_d, of the servo arm in increments of $d\theta$, at a defined time interval, dt. By changing the duration of the interval, the angular velocity, ω, can effectively be controlled with the following relationship:

$$\omega = \frac{d\theta}{dt}$$
(3.1)

The controller itself makes use of the pre-built open source Arduino Servo library. As such, no controller design steps were taken and the library was used as developed.

3.3 JM1 Dynamic Analysis

In order to fully characterize the actuation of the JM1 device, a mathematical model was developed to evaluate the range of motion and mechanical loads experienced by the joint.

3.3.1 Derivation of Flexion Angle Profile

First it is necessary to derive a relationship between the flexion angle of the joint and the angle of the servo-arm. Consider the annotated diagram of the system shown in Figure 37. Point *A* is defined as the servomotor shaft, *B* is the point at which the wire attaches to the servo-arm, *C* is the point at which the wire attaches to the top anchor, and *J* is the point of relative rotation between the tibia and femur of the joint.
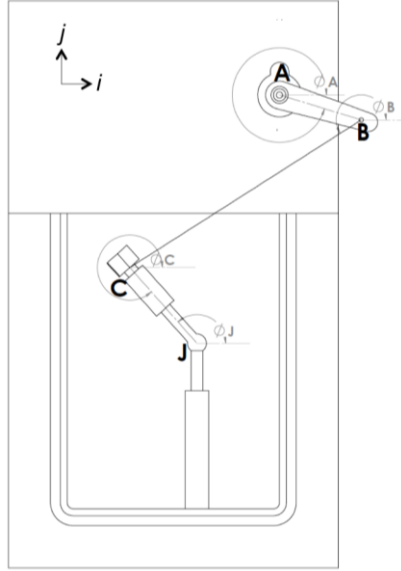
Figure 37: Annotated Schematic of JM1 – Definition of mechanical joints A, B, C and J, as well as their respective angles defined relative to a global coordinate system i-j.

A global coordinate system, *i-j*, is defined as shown and the origin is placed at point *A*.

Angles are defined as follows using a right-handed coordinate system:

- ϕ_A is the angle from the horizontal direction *i* to vector $\overrightarrow{AB}$

- ϕ_B is the angle from the horizontal direction *i* to vector $\overrightarrow{BC}$

- ϕ_C is the angle from the horizontal direction *i* to vector $\overrightarrow{CJ}$

- ϕ_J is the angle from the horizontal direction *i* to vector $\overrightarrow{JC}$

- $\phi_{flexion}$ is the flexion angle of the joint

Additionally, relevant lengths are defined as follows:

- L_{AB} is the length of vector $\overrightarrow{AB}$, also the length of the servo-arm

- L_{BC} is the length of vector $\overrightarrow{BC}$, also the length of the wire

- L_{CJ} is the length of vector $\overrightarrow{CJ}$, also the distance from the center of rotation of the joint to the wire-top anchor point of contact

- L_{JA}^x is the length of the *i*-component of the vector $\overrightarrow{JA}$

- L_{JA}^y is the length of the *j*-component of the vector $\overrightarrow{JA}$

In order to determine the relationship between the servo angle, ϕ_A, and the flexion angle $\phi_{flexion}$, it is necessary to look at the vector formulation of the system geometry. Recalling that *A* is defined as the origin, the vectors defining the positions of points *A, B, C,* and *J* can be written as:

$$\overrightarrow{A} = \begin{bmatrix} 0 \\ 0 \end{bmatrix}$$

$$\overrightarrow{B} = \begin{bmatrix} L_{AB} \cos(\phi_A) \\ L_{AB} \sin(\phi_A) \end{bmatrix}$$

$$\overrightarrow{C} = \begin{bmatrix} -L_{JA}^x + L_{CJ} \cos(\phi_J) \\ -L_{JA}^y + L_{CJ} \sin(\phi_J) \end{bmatrix}$$

$$\overrightarrow{J} = \begin{bmatrix} -L_{JA}^x \\ -L_{JA}^y \end{bmatrix}$$

The distance L_{BC} can be written as the magnitude of the difference between $\overrightarrow{B}$ and $\overrightarrow{C}$:

$$L_{BC} = |\overrightarrow{C} - \overrightarrow{B}| \tag{3.2}$$

Which can be re-written as:

$$(\vec{C} - \vec{B})(\vec{C} - \vec{B}) - L_{BC}^2 = 0 \tag{3.3}$$

Substituting the definitions for $\vec{B}$ and $\vec{C}$ yields:

$$\left(-L_{JA}^x + L_{CJ}\cos(\phi_J) - L_{AB}\cos(\phi_A)\right)^2 + \left(-L_{JA}^y + L_{CJ}\sin(\phi_J) - L_{AB}\sin(\phi_A)\right)^2 - L_{BC}^2 = 0 \tag{3.4}$$

Expanding and simplifying Equation 3.4 gives:

$$L_{JA}^{x\,2} + L_{JA}^{y\,2} - L_{BC}^2 + L_{CJ}^2 + L_{AB}^2 + L_{JA}^x L_{AB}\cos(\phi_A) + L_{JA}^y L_{AB}\sin(\phi_A)$$
$$+ \left(-2L_{JA}^x L_{CJ} - 2L_{CJ}L_{AB}\cos(\phi_A)\right)\cos(\phi_J)$$
$$+ \left(-2L_{JA}^y L_{CJ} - 2L_{CJ}L_{AB}\sin(\phi_A)\right)\sin(\phi_J) = 0 \tag{3.5}$$

Equation 3.5 can be regrouped as:

$$A_3 = A_1\cos(\phi_J) + A_2\sin(\phi_J) \tag{3.6}$$

Where:

$$A_1 \overset{\text{def}}{=} \left(2L_{JA}^x L_{CJ} + 2L_{CJ}L_{AB}\cos(\phi_A)\right)$$

$$A_2 \overset{\text{def}}{=} \left(2L_{JA}^y L_{CJ} + 2L_{CJ}L_{AB}\sin(\phi_A)\right)$$

$$A_3 \overset{\text{def}}{=} {L_{JA}^x}^2 + {L_{JA}^y}^2 - L_{BC}^2 + L_{CJ}^2 + L_{AB}^2 + L_{JA}^x L_{AB}\cos(\phi_A) + L_{JA}^y L_{AB}\sin(\phi_A)$$

By consider Equation 3.6 as a sine term with a phase lag, ϕ_J can be expressed as:

$$\phi_J = \sin^{-1}\left(\frac{A_3}{\sqrt{A_1^2 + A_2^2}}\right) - \tan^{-1}\left(\frac{A_1}{A_2}\right) \tag{3.7}$$

Finally, the flexion angle, $\phi_{flexion}$ can simply be found by realizing that:

$$\phi_{flexion} = \phi_J - 90^o \tag{3.8}$$

3.3.2 Comparison of Derived and Observed Flexion Angle Profile

Equation 3.8 can be used to determine the flexion angle profile as a function of the servomotor angle. A full cycle is actuated by rotation of the servomotor angle, ϕ_A, from 0° to -90° and returning to 0° as shown in Figure 38.
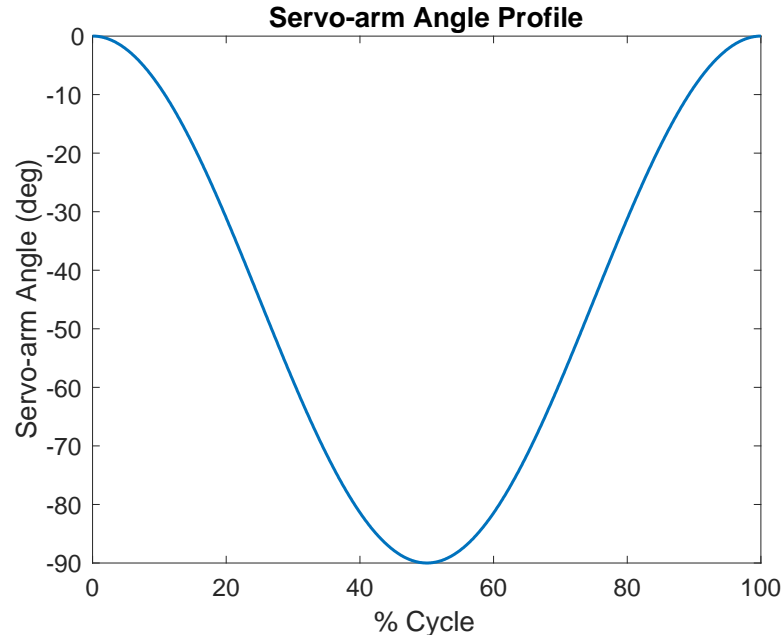
Figure 38: JM1 Servo-arm Angle Profile – The motion of the JM1 servo when actuated follows a quarter rotation from 0 to -90 degrees.

By solving for $\phi_{flexion}$ using the typical system parameters summarized in Table 3, the flexion angle profile is found and shown in Figure 39.

Table 3: Typical Parameters of a JM1 Device

Symbol	Parameter	Value (m)
L_{AB}	Distance from servomotor shaft to servo-arm/wire coupling point	0.0120
L_{BC}	Length of wire	0.0750
L_{CJ}	Distance from center of joint's rotation to wire/top anchor coupling point	0.0225
$L_{JA}{}^{x}$	Horizontal distance between center of joint to servomotor shaft	0.0223
$L_{JA}{}^{y}$	Vertical distance between center of joint to servomotor shaft	0.0765
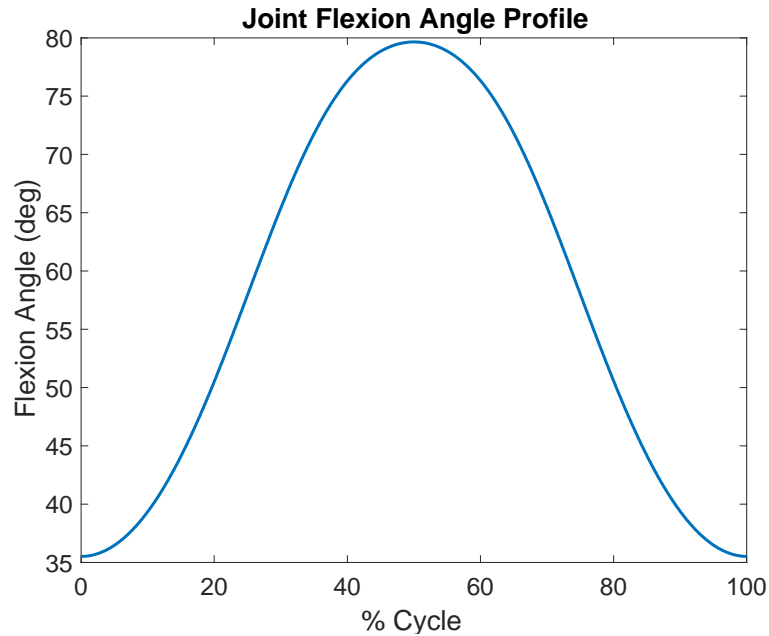
Figure 39: Joint Flexion Angle Profile in JM1 - The joint goes through a motion range of ~ 45 degrees with minimum and maximum flexion angles of 35 and 80 degrees respectively.

In order to further investigate and validate the range of motion, fluoroscopic video was taken of a single joint using a custom fabricated, X-ray friendly JM1 device. Flouroscopy was performed using an *in vivo* CT imaging system (IVIS SpectrumCT, PerkinElmer, MA, USA). Still images from the fluoroscopic video are presented in Figure 40, showing the state of the joint at various points in the cycle.
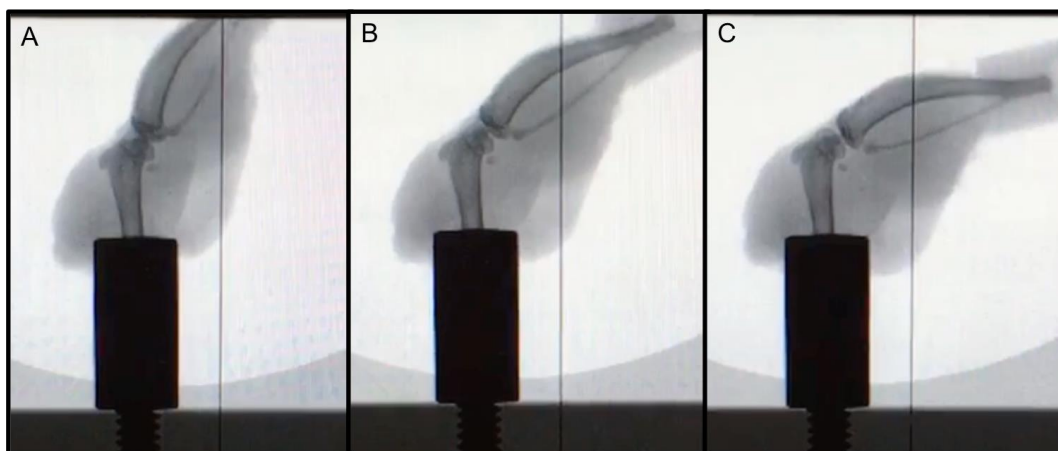
Figure 40: X-Ray Images of Stifle Joint Actuated by JM1 – The full range of an actual joint mounted in a CT-compatible JM1 device. A) 0% of Cycle (Minimum Flexion); B) 25% of Cycle; C) 50% of Cycle (Maximum Flexion)

Figure 40A and Figure 40C show the minimum and maximum flexion states of the stifle joint when actuated by the JM1, respectively. Qualitatively, the x-ray images indicate that the joint generally follows the profile calculated by the mathematical model presented. There is clear curvature of the tibia, meaning that there is no direct way to assign a flexion angle based on the relative angles between the tibia and femur. The definition of the geometric flexion angle is shown in Figure 41. Two lines are defined, AB and CD. Points A and B are assigned at the furthest anterior and posterior points of the distal end of the femur. Point C is anterior-most point of the tibial cartilage. Point D is assigned on a posterior protruding point of the fibula as shown. The flexion angle is defined between the lines perpendicular to AB and CD. By identifying the same features in all the x-ray images, the achieved flexion angles can be measured and compared to those predicted by modeling, Table 4.
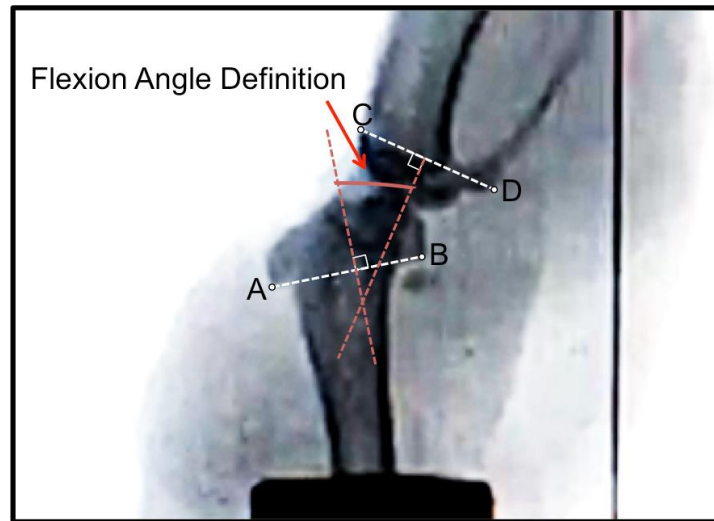
Figure 41: Geometric Definition of Flexion Angle – Due to the curvature of the tibia, a geometric definition was created to measure a representative flexion angle of actual mounted joints.

Table 4: JM1: Measured flexion angles and predicted flexion angles

% Cycle	Predicted Flexion Angle	Measured Flexion Angle +/- 1°
0	35°	36°
25	58°	50°
50	79°	67°

The results in Table 4 indicate that the flexion profile is matched with minimal error for lower flexion angles but lags increasingly as the flexion angle increases. Although an offset would be expected given the fact that the predicted angle is based on a simplified geometric assumption, the trend of increasing error with increasing flexion angle suggests that there is distortion of the joint bones during flexion. Comparing Figure 40 A and B, there is clearly an increase in the curvature of the tibia as the joint flexes. This increase in curvature would account for the lower than expected flexion angle as measured at the joint interface.

3.3.3 Estimation of Loads at the Tibia-Femur Interface

In addition to understanding the motion of the joint, it is helpful to derive an estimation of the mechanical loads at the joint surface as a function of the servomotor position. This is accomplished by analyzing a quasi-static model of the tibia and deriving the necessary reaction forces at the joint surface to maintain equilibrium. A free body diagram of the tibia and top anchor in an arbitrary position during the flexion cycle is shown in Figure 42.
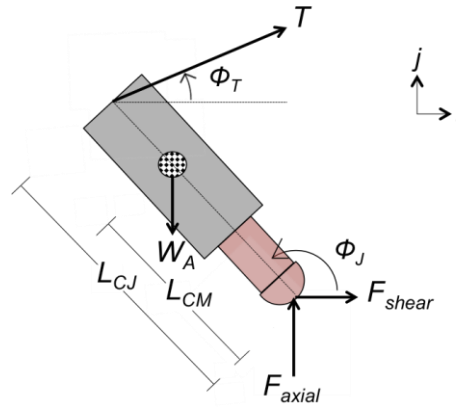
Figure 42: Free Body Diagram of Tibia and Top Anchor Assembly – The shown free body diagram is used to derive shear and axial loads at the joint.

The same global coordinate system, *i-j*, is used as in the analysis in Section 3.3.1. Furthermore the definitions of ϕ_J as the relative angle between the tibia and horizontal and L_{CJ} as the distance between the joint center and top anchor/wire connection point still hold true. The distance L_{CM} is defined as the distance between the joint center and the center of mass of the joint and top anchor assembly. The forces acting on the joint are defined as:

- T: wire tension,

- W_A: apparent weight of the tibia and top anchor assembly accounting for buoyancy in the culture medium

- F_{shear}: horizontal component of force at the tibia-femur interface

- F_{axial}: vertical component of force at the tibia-femur interface

F_{shear} and F_{axial} are also the shear and axial forces within the joint in the femoral reference frame. The wire tension, T, acts in the directions of the wire, given by ϕ_T relative to the horizontal. ϕ_T is related to ϕ_B by:

$$\phi_T = \phi_B - 180^o \tag{3.9}$$

ϕ_B can be derived by considering the i-component of $\vec{C}$ from two different directions:

$$\vec{C} \cdot i = -L_{JA}^x + L_{CJ} \cos(\phi_J) \tag{3.10}$$

$$\vec{C} \cdot i = \vec{B} \cdot i + L_{BC} \cos(\phi_B) \tag{3.11}$$

By equating Equations 3.10 and 3.11, and solving for ϕ_B:

$$\phi_B = \cos^{-1}\left(\frac{-L_{JA}^x + L_{CJ} \cos(\phi_J) - L_{AB} \cos(\phi_A)}{L_{BC}}\right) \tag{3.12}$$

In order to solve for the unknown forces, T, F_{shear} and F_{axial} one can sum forces in the i and j directions and moments about point J and solve for the static equilibrium condition as follows:

$$\sum F_i = F_{shear} + T\cos(\phi_T) = 0 \tag{3.13}$$

$$\sum F_j = F_{axial} + T\sin(\phi_T) - W_A = 0 \tag{3.14}$$

$$\sum M_J = -W_A L_{CM}\cos(\phi_J) - T L_{CJ}\sin(\phi_J - \phi_T) = 0 \tag{3.15}$$

Solving Equations 3.13, 3.14 and 3.15 for the unknown forces results in:

$$T = -\frac{W_A L_{CM}\cos(\phi_J)}{L_{CJ}\cos(\phi_J - \phi_T)} \tag{3.16}$$

$$F_{shear} = -T\cos(\phi_J) \tag{3.17}$$

$$F_{axial} = W_A - T\sin(\phi_J) \tag{3.18}$$

The apparent weight of the tibia and top anchor assembly, W_A, is estimated as:

$$W_A = g \left(\frac{1}{2} m_{joint} + m_{topa} - m_{dispfluid} \right) \tag{3.19}$$

Where $m_{dispfluid}$ is the mass of displaced fluid when the joint is placed in the culture medium, m_{topa} is the mass of the top anchor, m_{joint} is the mass of the explanted joint and g is the acceleration due to gravity. Values for masses and the displaced fluid were measured and summarized in Table 5. The center of mass of the tibia and top anchor assembly is assumed to be half the distance L_{CJ}.

Table 5: Relevant Masses in JM1 Model

Symbol	Number of Measurements	Mean Value (g)	Standard Deviation (g)
m_{joint}	9	0.85	0.07
m_{topa}	3	3.20	0.02
$m_{dispfluid}$	1	0.15	N/A

The solutions for the axial and shear joint forces are plotted in Figure 43 and Figure 44 respectively. For comparison, the solution to a separate model that takes into account the dynamics of the system (i.e. accelerations and inertial forces) is shown as well. For the sake of brevity a derivation of the dynamic model is not presented. In addition, the maximum error between the dynamic and quasi-static model is on the order of 10^{-3} gram-force, or ~0.6%.
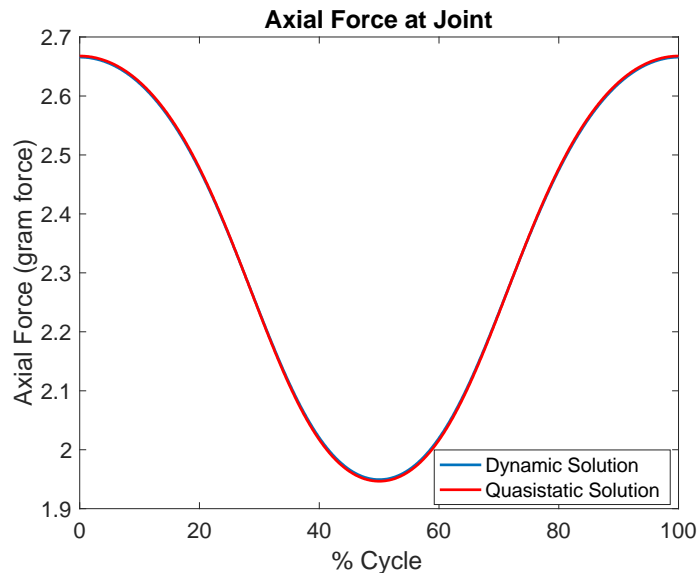
Figure 43: Axial Force of the Joint – The resulting axial force in the femoral frame under JM1 actuation as predicted by both quasistatic and dynamic models. Agreement between the two models indicates that system masses are the primary contributors to loads.
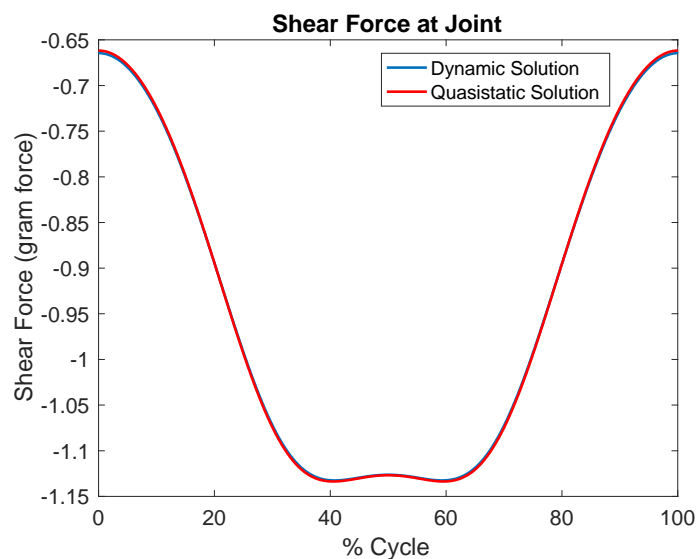
Figure 44: Shear Force of the Joint – The resulting shear force in the femoral frame under JM1 actuation as predicted by both quasistatic and dynamic models. Agreement between the two models indicates that system masses are the primary contributors to loads.

The model estimates that the joint experiences between 2.65 and 1.95 gram-force of axial compression 0.66 and 1.14 gram-force of shear throughout the cycle. The relatively low discrepancy between the dynamic and quasi-static model suggests that inertial forces are negligible and that the mass of the top anchor is the primary contributor in loading the joint.

3.4 Experimental Use of the JM1 – Investigation of Culture Medium Glucose Concentration

The JM1 provided a framework and system to determine suitable culture conditions for maintaining adequate viability of the explanted joints. As a requisite of a successful joint culture system, joint viability must be maintained over an extended period of time. This investigation focused on varying the concentration of glucose in Dulbecco's modified Eagle's medium (DMEM), a common culturing solution previously utilized in joint tissue culture [62], and evaluating the resulting histological response of joint tissue after a 7-day culture under JM1 actuation.

3.4.1 Joint Preparation

Eight-week-old NF_kB/Balb C mice were sacrificed using CO_2 exposure followed by cervical dislocation for confirmation of euthanasia. The rear stifle joints were freshly harvested and isolated by surgical removal. Both male and female mice, and left and right joints were used. The femur and tibia were severed approximately halfway between the stifle joint and hip and ankle joints respectively. All fur and skin was removed from the tissue to prevent possible contamination. Isolated joints are maintained in individual petri

dishes and hydrated in 10X phosphate-buffered saline (PBS) solution while awaiting culture preparation.

3.4.2 Sterility Measures

In order to prevent contamination, several sterility measures where taken during experimental set-up. All components of the JM1 device and tools used for assembly are individually sterilized using a 10 % bleach solution wash, followed by a de-ionized (DI) water rinse, and subsequently sprayed with a 70% ethanol solution. Finally, all components are placed under direct ultraviolet (UV) light exposure for >15 minutes. Following the steps outline in Section 3.4.1 for joint preparation, all samples are mounted into their appropriate culture conditions in a sterile cell culture hood. Extra care is taken to prevent the introduction of contaminants into the preparation environment.

3.4.3 Culture Conditions

The culture conditions are the variable for these experiments. Several runs were performed to test different levels of glucose concentration, where each run consisted of four to six joints mounted into JM1 devices, dubbed a 'dynamic' condition, four to eight joints are placed into petri dishes and set on a rotating table, dubbed a 'rotation' condition, and four to five joints are placed into petri dishes on static surface, dubbed a 'static' condition. See Figure 45 for a summary of conditions. The reason for employing both static and rotational conditions is to gain insight into the effects of both joint actuation and agitation of culture medium, which is a side effect of joint movement in the JM1 device. Effectively, the static condition controls for both actuation and fluid agitation, while the rotational condition only controls for actuation. All joints were cultured for a period of 7

days and immersed in DMEM solution with varying levels of glucose: 1.0 mg/ml, 4.5 mg/ml or 9.0 mg/ml referred to as low, moderate and high levels respectively. A breakdown of samplers per condition is presented Table 6.
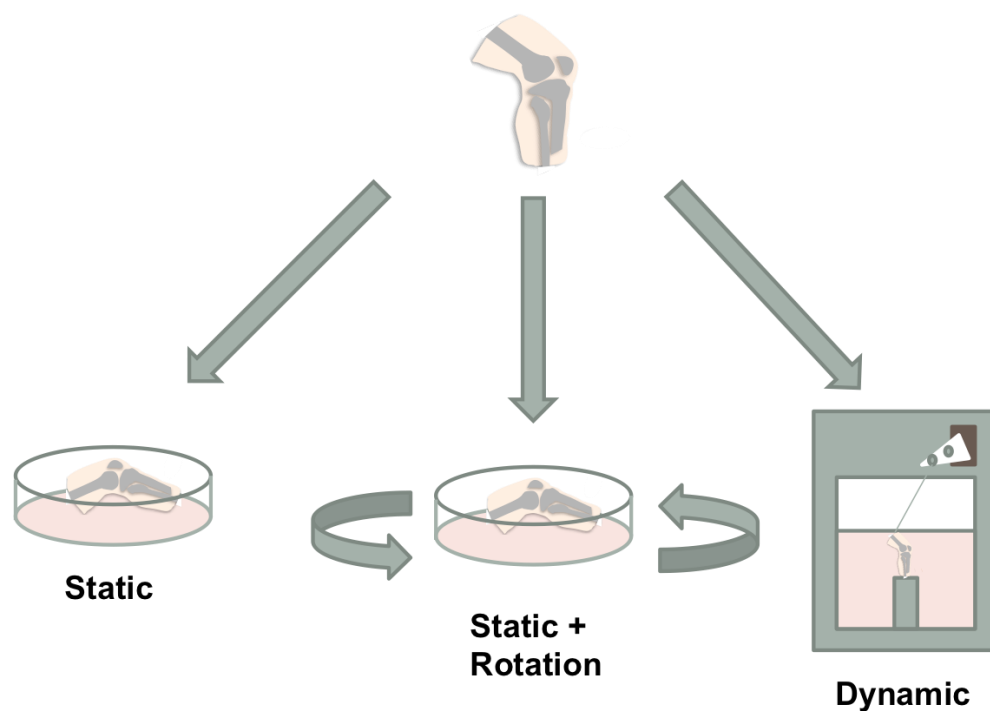
Figure 45: Glucose Investigation Culture Conditions - Left: static joints are maintained in cell culture dishes on a stationary surface; Center: rotational joints are maintained in cell culture dishes on a rotating platform; Right: dynamic joints are mounted into the JM1 device and acutated

Table 6: Glucose Investigation - Number of Samples per Condition

Culture Condition Glucose Concentration	Static	Rotation	Dynamic
1.0 mg/ml (low)	5	5	5
4.5 mg/ml (moderate)	5	5	4
9.0 mg/ml (high)	5	4	6

In total, 44 joints were cultured under the different conditions. Dynamic samples were subject to a 0.5 Hz cycle frequency and actuated for 8 hours/day, followed by a 16-hour static "resting" period. DMEM solution was changed once for each sample over the course of the seven-day culture, on either the third or fourth day following culture initiation.

3.4.4 Histological Assessment Methods

Following culture, joints are removed from their respective conditions and processed for histology. Each sample is fixed in paraformaldehyde (PFA) and decalcified. Excess muscle and bone are trimmed off, and samples are mounted in paraffin and sectioned laterally into 5 um-thick sections. A complete processing protocol is shown in Appendix B.

Sections from each sample are stained with a Safranin-O/Fast Green protocol for cartilage. The full protocol can be seen in Appendix C. The stain shows: cartilage matrix in red, underlying bone in green and cell nuclei in black. Stained samples are imaged using an optical microscope. Representative sections from each condition are qualitatively evaluated by inspecting the strength of Safranin-O stain on the articular cartilage surfaces and growth plates of the tibia and femur. See Figure 46 for a typical Safranin-O stain image.
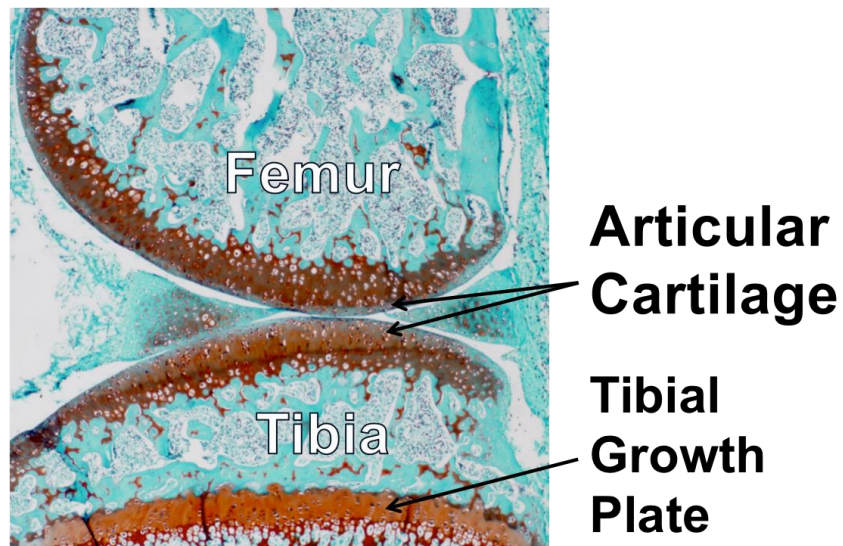
Figure 46: Typical Safranin-O Stained Mouse Stifle Joint – Red staining indicated cartilage, found primarily on the articular surface and growth plates; blue counterstain shows various tissues and bone.

Stained samples are also analyzed quantitatively. For each section, each articular surface (i.e. tibial and femoral) is assigned a score from 0 to 12 in accordance with a standard Osteoarthritis Association Research Society International (OARSI) developed scoring system [66]. The system is outlined in Figure 47 and is applied by observation of the staining strength in the region from the articular surfaces up to the calcified cartilage, indicated by the tidemark. The region is cut off approximated two-thirds into the menisci, Figure 48. All scoring was performed blindly from unmarked, randomized images.

What Type of Loss?

Partial Loss (Scores 1-6)

Complete Loss (Scores 7-12)

≤ ½ depth (Scores 1-3)

> ½ depth (Scores 4-6)

≤ ½ depth (Scores 7-9)

> ½ depth (Scores 10-12)

1 if ≤ 1/3 of surface

2 if ≤ 2/3 of surface

3 if > 2/3 of surface

4 if ≤ 1/3 of surface

5 if ≤ 2/3 of surface

6 if > 2/3 of surface

7 if ≤ 1/3 of surface

8 if ≤ 2/3 of surface

9 if > 2/3 of surface

10 if ≤ 1/3 of surface

11 if ≤ 2/3 of surface

12 if > 2/3 of surface
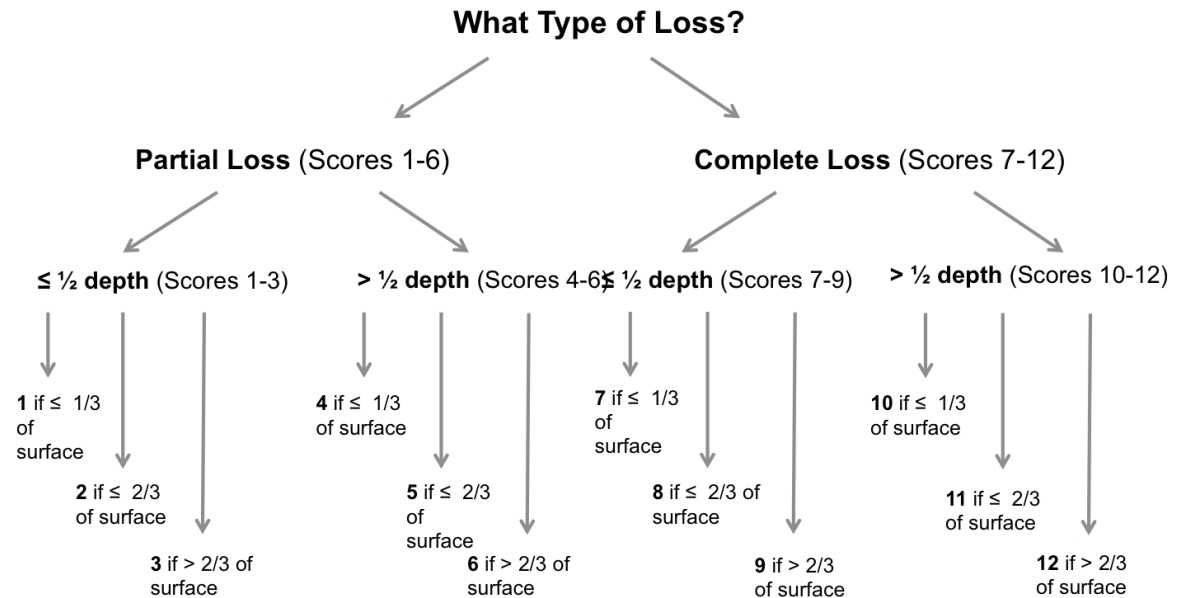
Figure 47: Flowchart for Determining OARSI Score – An integer score of 0-12 is assigned to each articular surface in accordance with the flowchart. Higher scores represent a greater degree of staining loss and hence greater degree of damage to the articular cartilage.

Figure 48: OARSI Scoring Region – Only the show outline of articular surface is used to derive OARSI scores.

A higher score represents a higher degree of loss of cartilage matrix and overall poorer joint health. Each joint sample is assigned an average score for the femur, tibia and total joint (femur + tibia) as the mean score of several sections (between 3 and 12 sections per joint). The average scores of all joints cultured under a certain condition are then averaged again to give the mean OARSI score per condition. The score reduction process is outline in Figure 49.
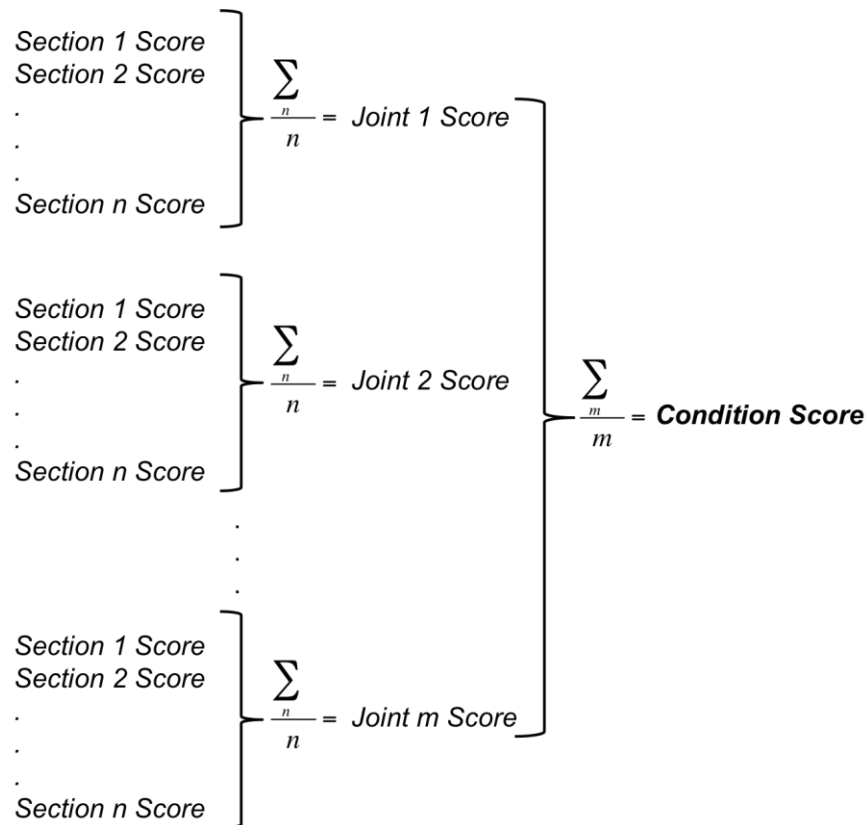
Figure 49: OARSI Score Reduction Method – Individual sections are scored initially and sections from a single joint are averaged to give a "Joint Score". All the joint scores for samples cultured under each of the glucose and motion conditions are then averaged to give the final "Condition Score".

The mean OARSI scores of each condition are compared to determine effects of the culture condition on joint heath. Significant differences are determined by performing select comparisons using the Mann-Whitney U test, with p-values below 0.05 considered statistically significant. Statistical testing was performed using GraphPad Prism (GraphPad Software, CA, USA).

3.4.5 Results

Representative Safranin-O stained sections of each culture are shown in Figure 50. Qualitative observation initially suggests that the dynamic low glucose concentration condition results in the strongest staining, implying a higher quality of joint health. This observation is particularly obvious when inspecting the tibial growth plate. The strongest growth plate staining is seen in the dynamic low glucose condition, followed by the static low glucose condition. Clear loss of staining in the growth plate is observed in the both high/moderate glucose and static/rotation interactions. Some growth plate staining is recovered for both high and moderate glucose under the dynamic condition. The dynamic moderate and high glucose samples also appear to have the most staining loss on the articular surface.

| Condition | Static | Rotation | Dynamic |
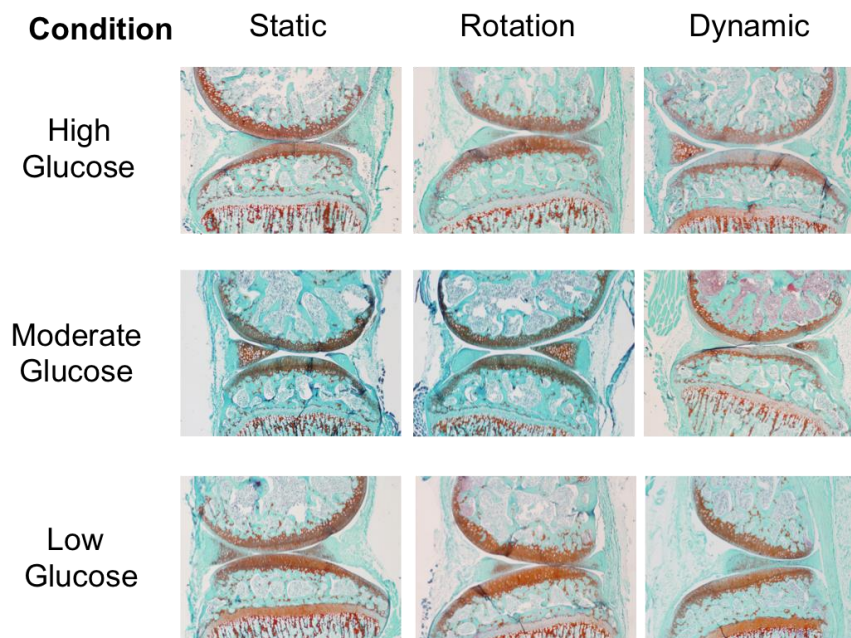
Figure 50: Representative Safranin-O Stains of Glucose Investigation Samples – Qualitative observation indicates that low glucose samples tend to have stronger staining, particularly on the tibial growth plate.

In order to quantify the observations seen in Figure 50, the OARSI scoring method described in Section 3.4.4 was used. The following figures summarize the mean OARSI scores for each condition in the tibia (Figure 51) and femur (Figure 52). A comparison of scores of rotational and dynamic high glucose cultures is shown in Figure 53 as well. Significant differences are marked with p-values as shown and error bars indicate the standard error of the mean. Significance was only calculated between groups sharing the same condition for either motion type or glucose level. For example, all samples in low glucose medium were compared; and the static high glucose condition was not tested against the dynamic low glucose condition.
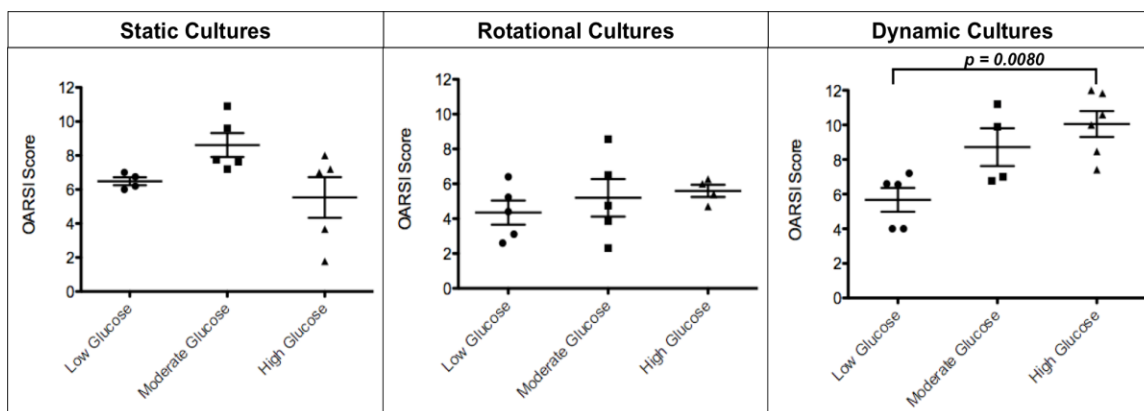
Figure 51: Glucose Investigation Summary of OARSI Scores for Tibia – Dot plots of tibial scores showing observations, mean score per condition and standard error of the mean as error bars; significant differences of interest are shown in the dynamic culture. Dynamic culture shows an effect where increasing glucose concentration results in an increased mean score that is significant when comparing low and high glucose cultured samples.
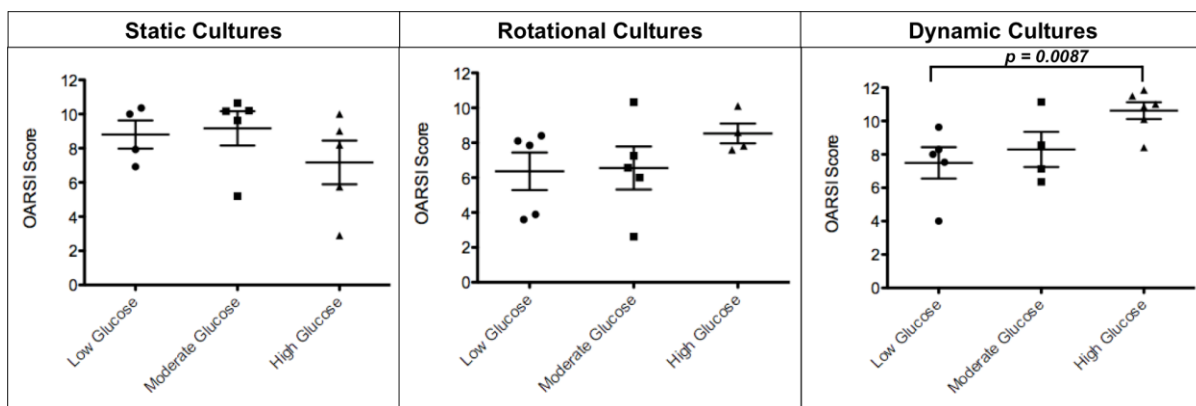
Figure 52: Glucose Investigation Summary of OARSI Scores for Femur – Dot plots of femoral scores showing observations, mean score per condition and standard error of the mean as error bars; significant differences of interest are shown in the dynamic culture.
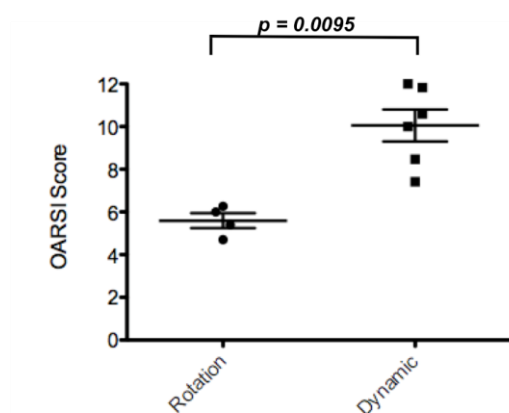
Figure 53: Comparison of Rotational and Dynamic Cultures Under High Glucose Culture - When cultured in a high concentration of glucose, a significant increase in tibial score is seen when samples are dynamically actuated.

Quantitative analysis reveals several trends in the culture conditions. First, samples cultured under in low glucose medium tended to a lower mean OARSI score. This trend is exaggerated in the dynamic loading condition, particularly visible in the mean tibia scores shown in Figure 51, where the dynamic low glucose condition is significantly lower than both dynamic high glucose culture ($p = 0.0080$). However, the rotational cultures show the same trend of decreased score with decreasing glucose concentration as well, although no significance is established. Dynamic cultures also tend to a higher mean score in general. However, the increase in score is only significant when comparing the high glucose dynamic and rotational cultures' tibial scores ($p = 0.0095$).

3.4.6 Discussion

The results provide several insights into the effects of the tested culture conditions on joint health. Joints cultured statically do not show a clear relationship between the OARSI score and glucose concentration. Although there is some statistical significance within the total and tibial scores between the moderate and low glucose static conditions, there is no measurable effect when increasing to a high glucose level, in part due to relatively high standard deviation of the static high glucose mean score (~50% in the case of the tibial score). Qualitative observation of the representative images in Figure 50 only shows a stronger staining in the low glucose condition compared to higher levels for the static samples, but no clear distinction between the moderate and high concentrations.

The role of glucose is more apparent in the rotational and dynamic conditions. This suggests that there is an increased amount of mass transfer between the culture medium and joint due to agitation of the fluid. Hence, any effects of glucose concentration are cultivated in the rotational culture and exaggerated in dynamic culture. The results indicate that the high level glucose is detrimental to joint health and results in a higher OARSI score, significantly so in samples under dynamic loading when compared to their low glucose counterparts. The results also suggest a steady decrease in mean score with decreasing glucose concentration. However significance has only been established in limited pairings under dynamic culture.

Another important observation is the increase in score between rotational and dynamic samples. It can be expected that the dynamic loading causes an increased amount of damage to the joint cartilage. However, this increase is only significant for samples cultured in a high concentration of glucose suggesting that the presence of excessive glucose may act as promoter of joint damage. This is consistent with a widely suspected link between OA and diabetes mellitus (DM) [67]. Past work has suggested that the

increased level of glucose in bodily fluids of diabetic patients acts to promote development of advanced glycation end products (AGEs), oxidative stress and inflammation [68, 69], resulting in initiation or worsening of OA. The low, moderate and high glucose levels used in the presented work correspond to physiological levels of a healthy, severely hyperglycemic and diabetic hyperosmolar individuals respectively, Table 7. In fact the high level of glucose used is beyond what would be required for a human individual to enter a diabetic coma (>6 mg/ml), and hence beyond the range seen medically.

Table 7: Medical Equivalence of Glucose Concentrations Tested

Culture Condition	Glucose Concentration (mg/ml)	Medical Equivalent
Low Glucose	1.00	Healthy
Moderate Glucose	4.50	Severely Hyperglycemic
High Glucose	9.00	Non-physiological/extreme

Finally, there are some observations made which relate to the validity of the assessment methods selected. There is general agreement between the qualitative and quantitative analyses. The quantitative analysis suffers from the fact that it does not take into account the strength of staining on the growth plate. Furthermore, there is a tendency for scores taken from the tibial surface to be more consistent than those taken from the femoral surface. This can be seen by the clearer trends in Figure 51 as opposed to Figure 52. This is due to the relatively thinner area of articular cartilage on the femur. As a result, staining loss tends to go through the full depth of the articular surface more frequently. Incidentally, scores taken from the femur tend to fall in the score ranges associated with >½ depth loss (4-6, 9-12), with approximately 80% of all scores falling in those ranges, Figure 54. The tibial articular cartilage however is relatively deeper resulting in a more even distribution of scores, Figure 55.
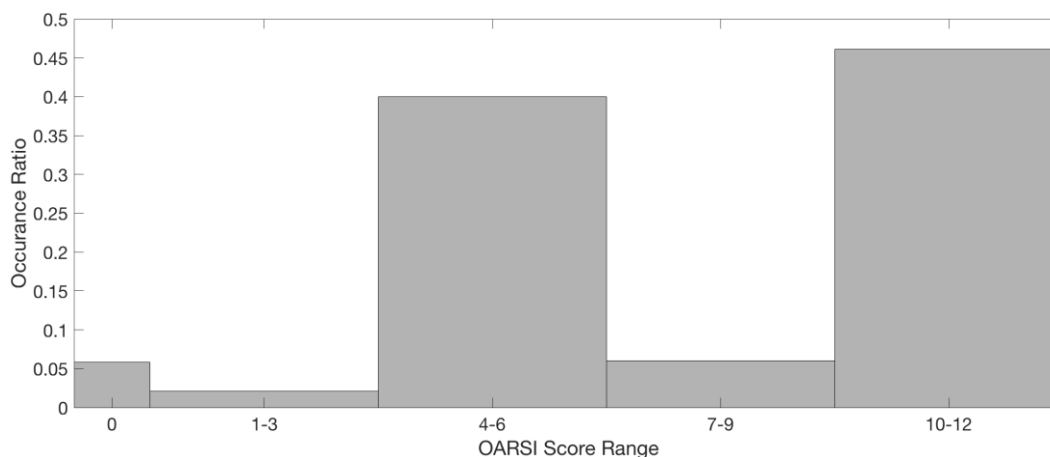
Figure 54: Distribution of Femur Scores in Glucose Investigation – Femur scores tend to aggregate in categories associated with full depth staining loss (4-6, 10-12) making them unsuitable for drawing conclusive results.
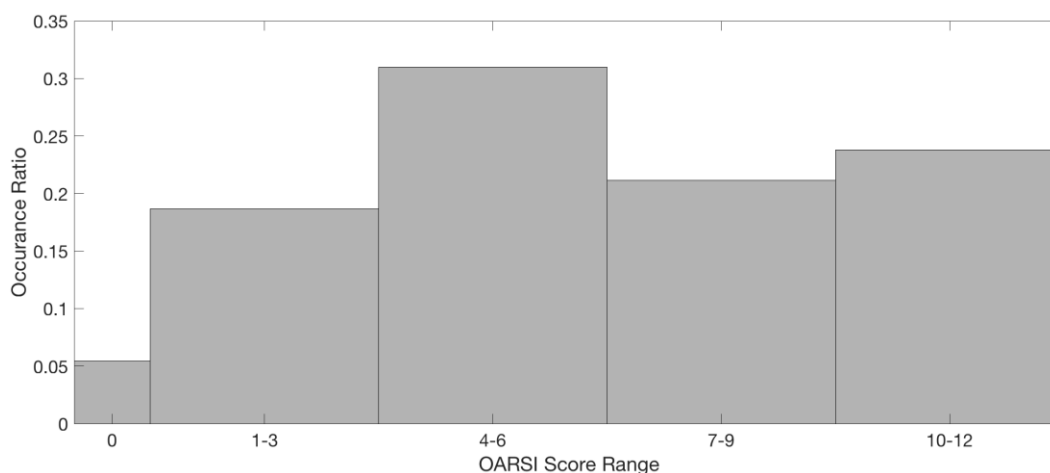
Figure 55: Distribution of Tibia Scores in Glucose Investigation – Compared to femoral scores, the tibia scores display a more even distribution.

The distribution of femur scores calls into question the validity of their use in making conclusions about the culture conditions. Figure 55 indicates that the tibia score is a more suitable indicator and provides a higher level of precision in categorizing staining loss. The observations discussed earlier are in fact most prevalent in the tibial scores shown in

Figure 51, supporting the argument that these provide a superior measure of subtle differences in the articular cartilage staining.

In summary, the following conclusions are drawn from results of this investigation:

1. In situations where mass transfer is promoted between the joint and culture medium, increasing glucose concentration in the medium results in a higher degree of staining loss as measured by the OARSI scoring method;

2. Dynamic actuation of the joint during culture leads to an increase in staining loss when a sufficient concentration of glucose is present, suggesting that glucose promotes degeneration of the cartilage matrix;

3. Quantitative assessment of the tibial articular surface staining is effectively a more sensitive method of categorizing sections and determining joint damage.

The low glucose medium provides the best environment for further testing the effects of dynamic loading on articular cartilage degeneration. However, limitations of the JM1 system had to be addressed in order to move into an investigation focusing on the effects of different levels of dynamic actuation on joint health.

3.5 Limitations of the JM1

The JM1 showed promising results for the development of a valid *in vitro* OA modeling system. However, the system has several limitations that made it unsuitable for further investigation. The limitations fall into two major categories: 1) component

limitations, and 2) design limitations; both of which in addition to limiting the reliability and repeatability of the system, result in several usability concerns.

3.5.1 Component Limitations

The primary component limitation is the lack of reliability of the servomotors used to actuate the joint. The servomotors are unreliable in the incubator environment, with lifetimes ranging from several days to as low as a few hours. It was necessary to continually replace motors during the duration of experiments, resulting in downtime during flexion/extension cycles and inconsistent actuation patterns. This creates an unnecessary burden on researchers using the device, as they require constant monitoring to ensure continued functionality. A suitable system needs to operate autonomously in order to be of value to researchers. The steps taken to overcome this are discussed in the following chapter.

3.5.2 Design Limitations

Three major design limitations are also addressed. The first is the adhesive based joint mounting system. The required use of adhesive creates a difficult situation for users, as the systems must be set up and allowed to cure for several hours before it can be run. On several occasions the mounting position was unsuitable and the system needed to be set up again. Again, this is a burden on the user and can cause delays in running experiments. Furthermore, the mounting system provides no means of assuring repeatability in the joint position. Effectively, variations in the joint position lead to differences in the system geometry.

The second design limitation is the use of a wire to interface the joint and servomotor. The wire is attached during set up and tied by the user, leading to variations in length. Again this contributes to changes in the system geometry, which in turn result in a deviation of the flexion angle profile. The effect is compounded by errors in the joint mounting. For example, shows two flexion angle profiles for two wire lengths: nominal 75 mm and 76 mm.
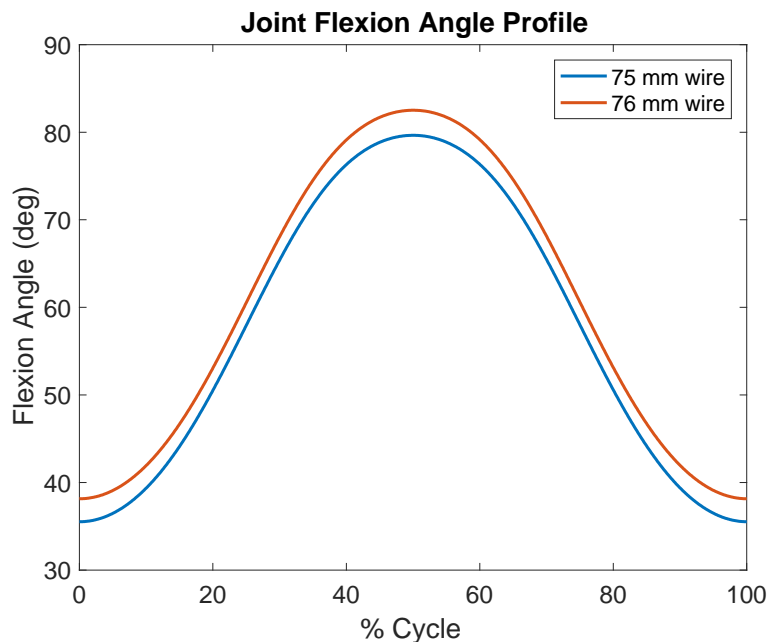
Figure 56: Flexion Angle Sensitivity to Wire Length - Comparison of flexion angle profile under two wire lengths; as much as a 1 mm deviation in wire length between two devices can lead to several degrees of error in the flexion angle.

A 1 mm error in the wire length results in several degrees of error in the flexion angle profile. This error in wire length is likely lower then what the user can achieve. Compounded with the effects of mounting errors, one can expect that the relative motion profiles of two systems would deviate significantly. The sensitivity of the profile to error indicates that tight control of the geometry is crucial to repeatability.

The final limitation is the lack of controlled and adaptive loading on the joint. The JM1 system can only provide one loading profile in terms of shear and axial force at the joint surface, as shown previously in Figure 43 and Figure 44. Although adjusting the weight of the top anchor can alter the magnitudes of these loads, there is no method change the profile to alter the load as a controlled function of the cycle position. The addition of such functionality is discussed in Chapter 5.

3.6 Conclusions

Despite the drawbacks of the JM1 system, it provided a successful test bed of initial investigation. The system was designed as a prototype with the purpose of investigating culture conditions and determining suitable culture medium glucose levels for future experiments. The concentration of glucose in culture medium was found to have a significant effect on joint health and promoted degeneration of the articular cartilage matrix under higher concentrations. The application of dynamic loading of samples in the JM1 inflated this effect and suggests that high level of glucose primes the joint surface for damage.

However, working with the JM1 device led to the realization that an improved system needed to be developed to satisfy the overall research objective. The second-generation joint-in-motion system is the subject Chapter 4, and addresses the several limitations in functionality and usability of the JM1 system.

4

Second-Generation Joint-in-Motion System

4.1 Introduction

The second-generation Joint-in-Motion system, or JM2, was developed to address the limitations of the JM1 system. The JM2 design process was approached with the goal of addressing reliability, repeatability and usability issues identified in its predecessor. The system was designed from concept through fabrication as part of this research. This chapter primarily discusses the design and testing of the JM2 as a joint actuator with tight control of the flexion angle. The JM2 system was used to investigate the effects of flexion cycle rate and duration on the health of joint samples. Development of extending the functionality of the JM2 to support controlled loading of the stifle joint is discussed in Chapter 5.

The purpose of this chapter is to address:

1. Mechanical design and fabrication of the JM2.

2. The design and implementation of a robust controller system to control the joint flexion angle profile with respect to time.

3. Development of an analytical model to describe system dynamics.

4. Use of system to investigate the effects of actuation rate and activity duration on articular cartilage degeneration.

4.2 JM2 System Overview

4.2.1 Design Requirements and Concept Generation

The JM2 was designed to overcome the shortcomings of the JM1. The design process was driven by the identification of five specific design requirements, summarized in Table 8.

Table 8: JM2 Design Requirements and Solutions

	Design Requirement	Solution		Accomplished in JM1?
1	Whole stifle joint must be cultured and the system must support cell viability.	-	The joint is kept in a reservoir of culture medium.	Yes
2	Joint flexion angle must be controlled as a function of time.	- -	Include the stifle as a mechanical joint in a well defined, closed loop mechanical linkage system. Develop a mechanical clamping system that securely holds the joint in place within the device.	Partially
3	The mechanical load on the joint must be actively controlled and be potentially variable within in a single flexion/extension cycle.	- -	Joint loading is accomplished using a secondary actuator that can function independently of the flexion/extension cycle. Develop a well-coordinated digital control system to control outputs of both actuators.	No
4	System components must be able to withstand the environment of the incubator.	- -	Test mechanical components and actuators for incubator lifetime. Use actuators suited for continuous, long-term use (e.g. DC gear motors).	Partially
5	The system must be simple and relatively inexpensive to fabricate and implement to allow for multiple devices to run in parallel.	- -	The design must primarily be composed of aluminum and acrylic plate components. The system footprint and volume must be relatively small (~<6"x6"x6") in order to fit multiple devices in the incubator.	Yes

The first requirement regarding supplying culture medium to the joint was accomplished in the JM1 by maintaining the joint in a reservoir and thus was conceptually unchanged. In order to tightly control the flexion angle profile, the second requirement, it was determined that the joint must be maintained as part of a rigid linkage system. Additionally, a robust mounting system had to be developed in order to repeatedly mount the joint and ensure maintenance of the geometry. The third requirement addresses the addition of controlled loading capability. This is achieved by adding a second actuator to the system. The details of the loading system are the subject of Chapter 5. The fourth requirement addresses the issue of reliability of components in the incubator environment. This is approached by extensive prototyping and testing of the system to gauge component lifetimes. The last requirement ensures that the system remains low-cost and easy to manufacture, in order to maintain the advantage of parallel usage of several devices.

The JM2 was designed around the concept of two actuated four-bar linkage systems coupled through a fulcrum, or shared joint, with the intent of moving the stifle joint in a bicycle-like motion while simultaneously applying a controlled compressive or tensile load. The design concept is shown in Figure 57. The four-bar linkage system OABC, termed the *drive linkage system*, defines the flexion angle of the knee. OABC operates as a crank-rocker mechanism, where an actuator at joint A rotates link AB resulting in a rocking motion of link OC about joint O. For a defined set of link lengths, AB, BC, CO and OA, the angles between each sequential link pair (e.g. AB & BC) will be defined as a function of the rotational angle of AB. The stifle joint is mounted as part of the linkage system and makes up mechanical joint C.
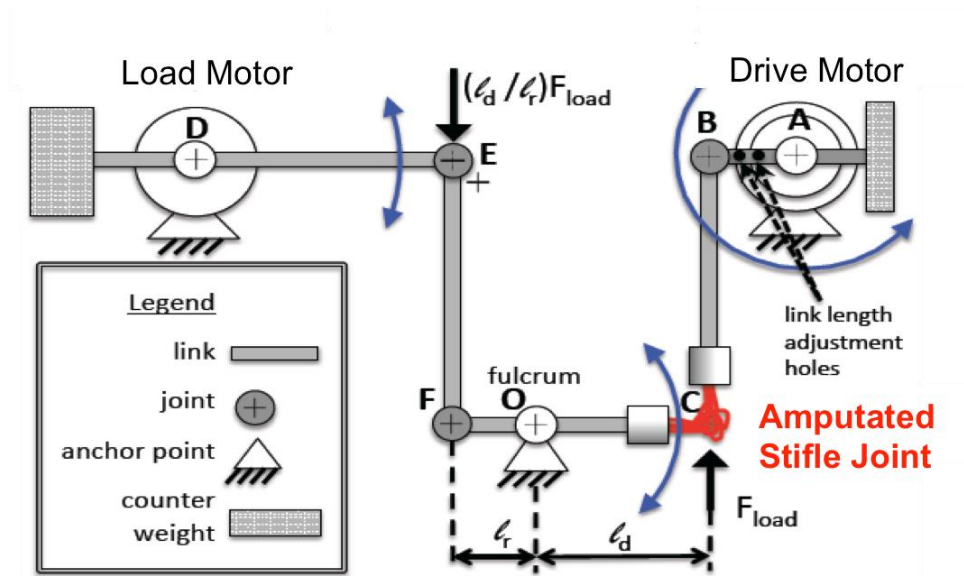
Figure 57: Conceptual Schematic of JM2 Design – The system is based on the concept of two coupled four-bar linkage systems. ABCO acts as a crank-rocker mechanism, where rotation of AB results in a rocking of CO and hence control of the joint flexion angle, with the stifle joint mounted at C. ODEF allows a torque applied at D to result in a controlled force at the stifle joint.

The second four-bar linkage system ODEF, termed the *loading linkage system*, operates as a rocker-rocker mechanism and contributes to controlling the load at the knee. A rocking motion of FO about O results from the coupling with OABC through the fulcrum, and is transmitted resulting a rocking motion of DE about D. Although the motion of OABC defines the motion of ODEF, it is possible to apply compressive or tensile loads at joint C (the joint) by controlling a torque of an actuator at joint D.

4.2.2 Mechanical Design

The JM2 system is shown in Figure 58. Note that Figure 58C only shows the system with the drive linkage system assembled and thus the stifle joint is decoupled from the

loading actuator. The loading linkage system will be detailed and discussed extensively in Chapter 5. Several design features are displayed in detail in Figure 59.
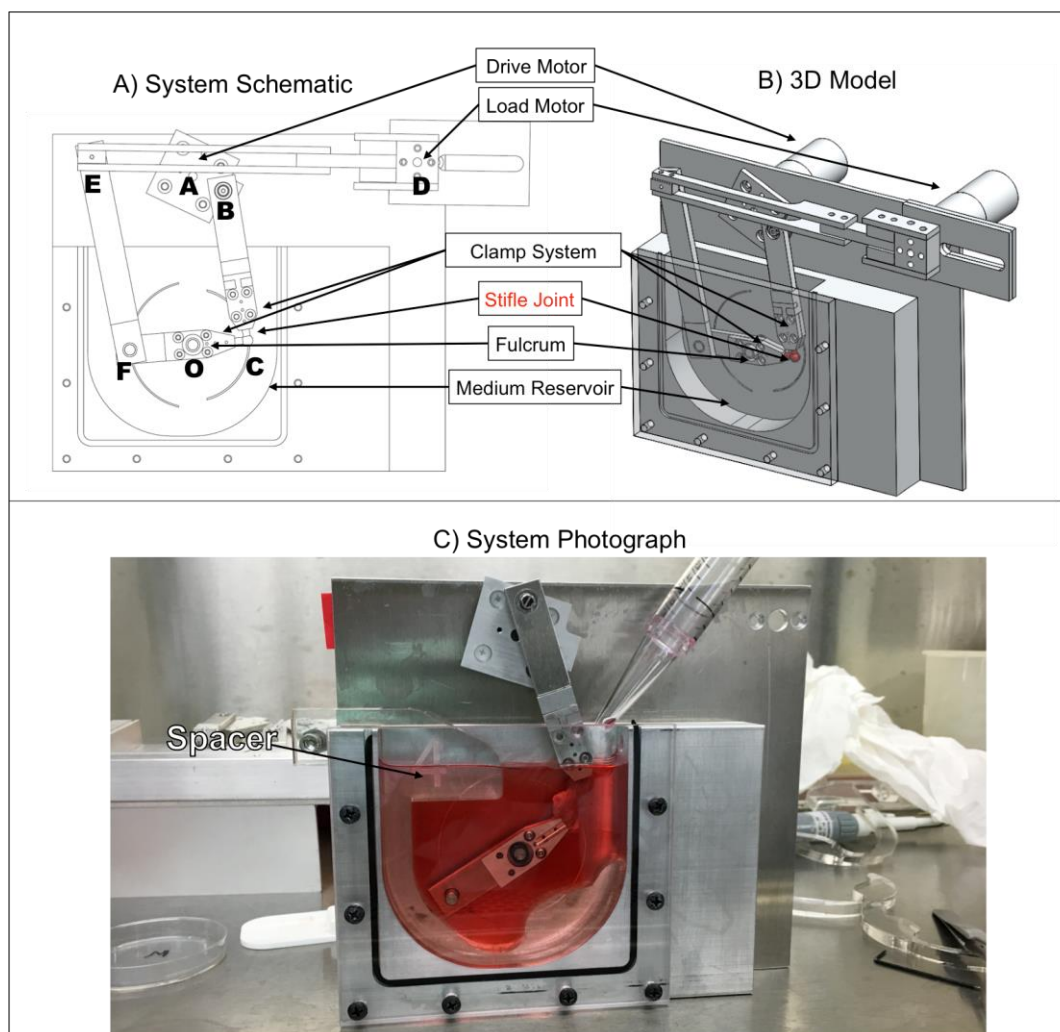
Figure 58: JM2 System - A) 2D Schematic; B) 3D CAD Model; C) Photograph showing drive linkage system
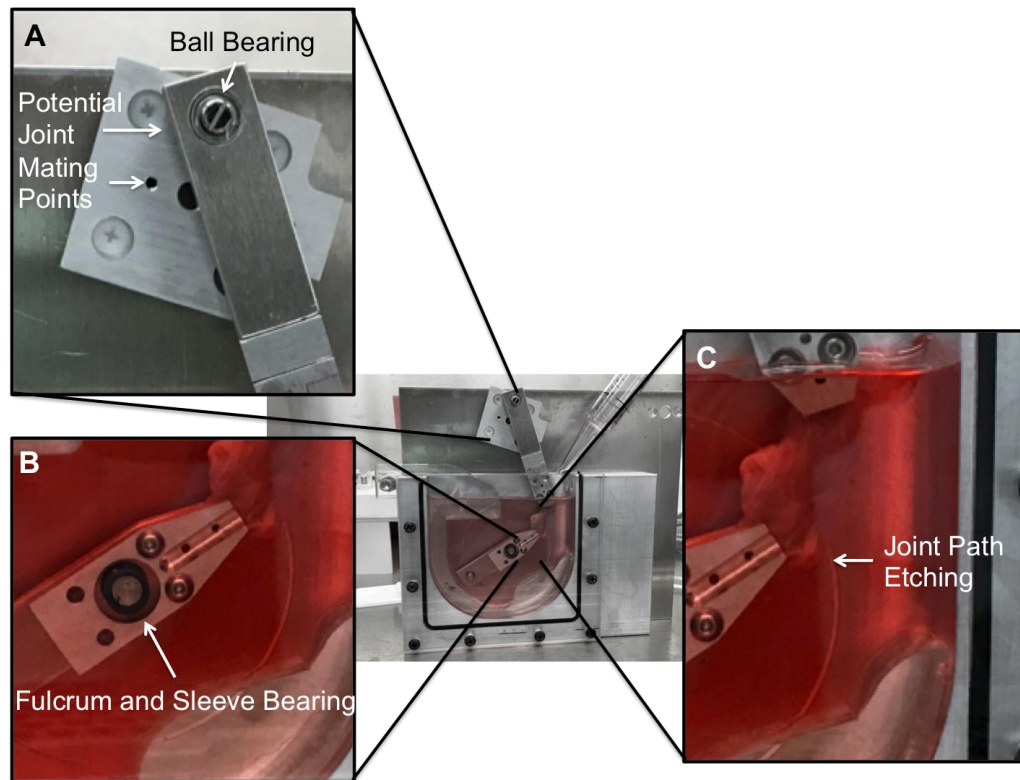
Figure 59: JM2 Design Detail - A) Alternate mating points allow for change of the effective link length/flexion angle range; B) Submerged fulcrum and specialty sleeve bearing; C) Etching of joint path on reservoir

The main system components are fabricated from 6061 aluminum and clear acrylic sheets. Stainless steel double shielded ball bearings (57155K381, McMaster-Carr, Robbinsville, NJ, USA) are used at joints B and E and do not make contact with the culture medium, seen at joint B in Figure 59A. For the immersed joints at O and F, rotational motion is sustained by stainless steel shafts coupled with polyether ether ketone (PEEK) chemically resistant sleeve bearings (6627K402 & 6621K113, McMaster-Carr, Robbinsville, NJ, USA), Figure 59B. An O-ring seal between the front plate and reservoir blocks culture medium leakage. The face of the reservoir is etched to indicate the stifle joint path during the actuation cycle, Figure 59C. This marking allows the user to ensure that the stifle joint is correctly placed within the geometry of the linkage system. DC gear

motors are used as the actuators at A and D. The motor at A, the flexion drive motor, has a ~47:1 output to input gear ratio (2285, Pololu Robotics & Electronics, Las Vegas, NV, USA) while the motor at D, the loading control motor, has a ~34:1 output to input gear ratio (2284, Pololu Robotics & Electronics, Las Vegas, NV, USA). These gear ratios were selected by considering the expected speeds and loads required. Both motors are equipped with 48 count per revolution Hall-effect encoders. The motors were tested in the incubator environment by running them at constant speed for 21 days straight and monitored intermittently. There were no instances of motors ceasing to run due to degradation of component quality in the incubator. A custom fabricated acrylic spacer can be seen in the reservoir in Figure 58C. Its purpose is to simply consume reservoir volume when the system is set up without he loading linkage system assembled, effectively reducing the amount of culture medium required to fully submerge the stifle joint. Overall the system measures approximately 18x15x5 cm.

4.2.3 Linkage Geometry Design

In order to satisfy the requirement of effective control of flexion angle, the linkage system OABC was designed to obtain a desired range of knee flexion angles. Consider the four-bar linkage shown in Figure 60 a), showing it at an arbitrary state. Link AB can rotate about A and forms an angle θ_A relative to the horizontal. Link OA is fixed as the machine frame.
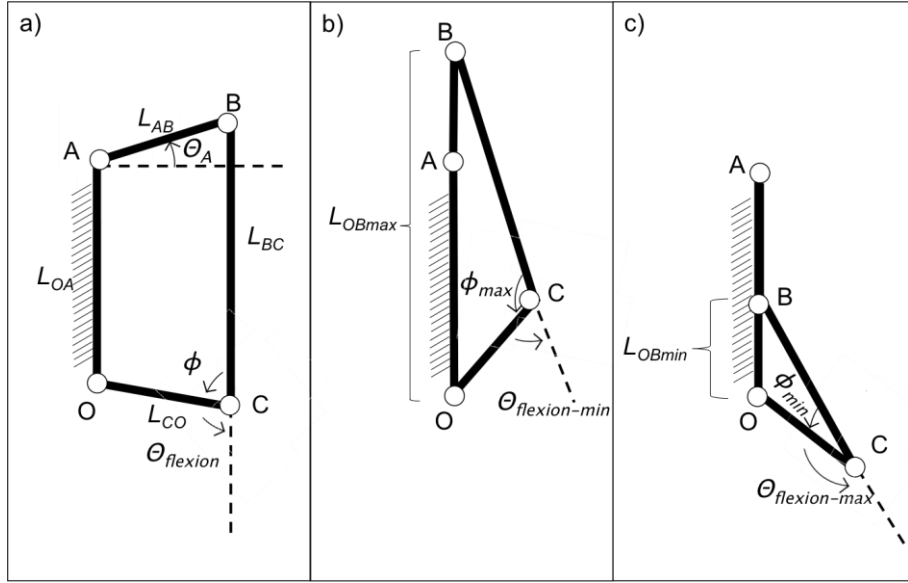
Figure 60: Four-bar Linkage Geometry - a) arbitrary state; b) state for maximum internal angle at joint C; c) state for minimum internal angle at joint C.

In the JM2, the stifle is effectively joint C and the knee flexion angle, $\theta_{flexion}$, is the supplementary angle of the internal angle at C, ϕ.

$$\theta_{\text{flexion}} = 180° - \phi \tag{4.1}$$

The law of cosines can be applied to determine the distance between joints O and B, L_{OB}, as either a function of θ_A (Equation (4.2)) or ϕ (Equation (4.3)).

$$L_{OB}^2 = L_{OA}^2 + L_{AB}^2 - 2L_{OA}L_{AB}\cos(90° + \theta_A) \tag{4.2}$$

$$L_{OB}^2 = L_{CO}^2 + L_{BC}^2 - 2L_{CO}L_{BC}\cos(\phi) \tag{4.3}$$

From Equation (4.3) it is clear that ϕ is maximum when L_{OB} is maximum and minimum when L_{OB} is minimum. By Equation (4.1), this corresponds to a minimum and maximum case for the value of $\theta_{flexion}$ respectively. The maximum and minimum values of L_{OB} occur in the configurations shown it Figure 60 b) and Figure 60 c) respectively, when joint B is collinear with joints A and O. This is clear from Equation (4.2) as well, corresponding to the cases of $\theta_A = 90^o$ and $\theta_A = 270^o$. Considering this, two special cases of Equation (4.3) can be written as:

$$(L_{OA} + L_{AB})^2 = L_{CO}^2 + L_{BC}^2 - 2L_{CO}L_{BC}\cos(\phi_{max}) \qquad (4.4)$$

$$(L_{OA} - L_{AB})^2 = L_{CO}^2 + L_{BC}^2 - 2L_{CO}L_{BC}\cos(\phi_{min}) \qquad (4.5)$$

Equations (4.4) and (4.5) are two independent equations making it is possible to set two link lengths as variables which may be calculated for a defined maximum and minimum value of ϕ (or $\theta_{flexion}$). L_{AB} and L_{BC} are set as variables, as they are both outside the culture medium and therefore relatively easy to replace or adjust, while L_{CO}, L_{OA}, ϕ_{max}, and ϕ_{min} are considered constants. L_{AB} and L_{BC} can now be solved for any set of constants. Such a relationship allows us to derive suitable lengths for L_{AB} and L_{BC} for a desired range of flexion angles. Subtracting (4.5) from (4.4) yields:

$$4L_{AB}L_{OA} = 2L_{BC}L_{CO}(\cos(\phi_{min}) - \cos(\phi_{max})) \qquad (4.6)$$

Solving (4.6) for L_{AB} yields:

$$L_{AB} = \frac{L_{BC}L_{CO}}{L_{OA}}(cos(\phi_{min}) - cos(\phi_{max})) = \kappa L_{BC} \qquad (4.7)$$

Where:

$$\kappa \stackrel{\text{def}}{=} \frac{L_{CO}}{L_{OA}}(cos(\phi_{min}) - cos(\phi_{max}))$$

Equation (4.7) can now be substituted into (4.5):

$$L_{OA}^2 + 2\kappa L_{BC}L_{OA} + \kappa^2 L_{BC}^2 = L_{BC}^2 + L_{CO}^2 - 2L_{BC}L_{CO}\,cos(\phi_{max}) \qquad (4.8)$$

Equation (4.8) can be re-arranged as a quadratic equation in L_{BC} and the constant coefficients a, b, and c can be defined:

$$\underbrace{(\kappa^2 - 1)}_{a}L_{BC}^2 + \underbrace{(2\kappa L_{OA} + 2L_{CO}\,cos(\phi_{max}))}_{b}L_{BC} + \underbrace{(L_{OA}^2 - L_{CO}^2)}_{c} = 0 \qquad (4.9)$$

L_{BC} can now be solved through the quadratic formula, and L_{AB} can be subsequently calculated using Equation (4.7). The full solution allowing the calculation of L_{BC} and L_{AB} for a desired range of flexion angles $\theta_{K-min} < \theta_K < \theta_{K-max}$ can be summarized as:

$$L_{BC} = \frac{\left(-b \pm \sqrt{b^2 - 4ac}\right)}{2a} \tag{4.10}$$

$$L_{AB} = \kappa L_{BC} \tag{4.7}$$

$$where:$$

$$a \stackrel{\text{def}}{=} (\kappa^2 - 1)$$

$$b \stackrel{\text{def}}{=} 2\kappa L_{OA} + 2L_{CO}\cos(\phi_{max})$$

$$c \stackrel{\text{def}}{=} (L_{OA}^2 - L_{CO}^2)$$

$$\kappa \stackrel{\text{def}}{=} \frac{L_{CO}}{L_{OA}}(\cos(\phi_{min}) - \cos(\phi_{max}))$$

$$\phi_{\min} = 180° - \theta_{\text{flexion-max}}$$

$$\phi_{\max} = 180° - \theta_{\text{flexion-min}}$$

Positive real solutions for L_{BC} and L_{AB} represent configurations of the four-bar linkage that satisfy the Grashof criterion[1] and permit the system to operate as a crank-rocker mechanism.

Using the relationships derived in Equation (4.7) it is possible to design the link lengths of the flexion linkage system to produce flexion angles within a desired range

---

[1] The Grashof criterion states that the sum of the shortest and longest link lengths must be less that the sum of the intermediate link lengths in order for a four-bar linkage system to have at least one fully rotating link.

throughout the cycle. Three sets of flexion angle ranges have been designed for, and the corresponding link lengths are shown in Table 9.

Table 9: Flexion Linkage Link Lengths and Corresponding Flexion Angle Ranges

Minimum Flexion Angle (°)	Maximum Flexion Angle (°)	Range (°)	L_{AB} (in)	L_{BC} (in)	L_{CO} (in)	L_{OA} (in)
67	100	33	0.25	2.75	1	3.00
53	112	59	0.45	2.75	1	3.00
37	120	83	0.60	2.75	1	3.00

The angle ranges were determined such that the required links are easy to fabricate and that three representative ranges could potentially be investigated. Furthermore, only the effective length of L_{AB} needs to be changed. This is accomplished by having multiple mating points for joint B on link AB (as shown in Figure 59B) providing the advantage that the flexion angle range can be altered without replacing any components of the JM2.

4.2.4 Joint Mounting System

A custom mounting system was developed in order to reduce the error associated with insertion of the stifle joint into the system. The flexion angle profile is highly sensitive to variations in the linkage geometry, and hence error in mounting the joint can have consequences on the motion profile. The mounting system consists of two parts: a robust clamping subsystem, Figure 61, and a mounting block, Figure 62. Along with the etched paths in the reservoir wall (shown previously in Figure 59C), the mounting system was

designed to minimize error in aligning the explanted stifle joint with the linkage system and ease the set-up process for the user.
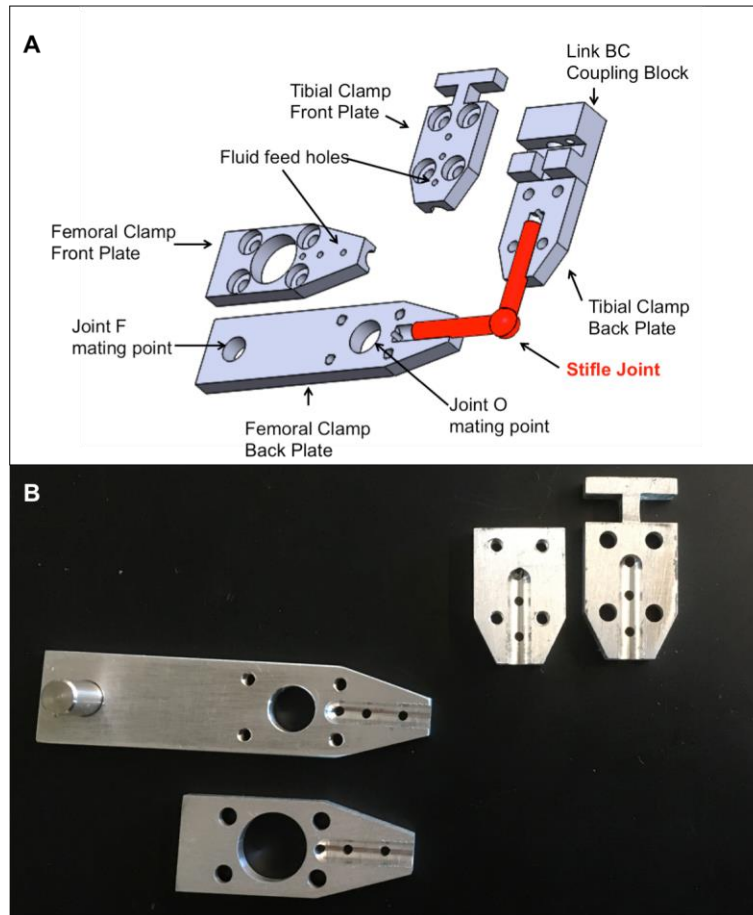
Figure 61: Clamping System – A pair of parallel plates are used to hold the joint by the tibia and femur rigidly; A) Annotated CAD model; B) Fabricated system
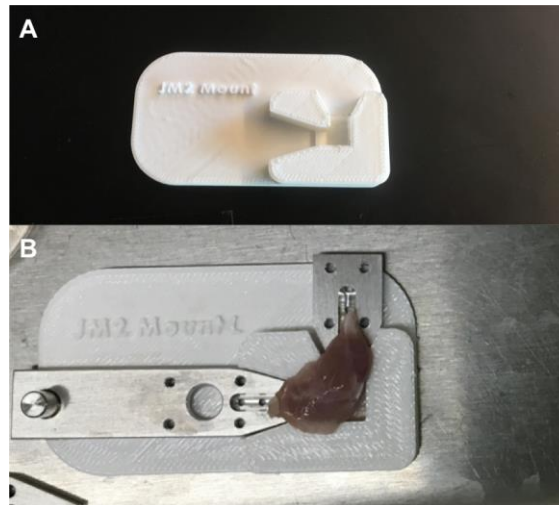
Figure 62: Mounting System – A supplementary mounting block was developed to align the stifle joint with the clamping system in a repeatable manner; A) Mounting block; B) Mounting block used to align stifle with clamp plates

The clamping system is effectively a parallel plate system that allows the stifle joint to be clamped outside the JM2 body, and easily placed into the machine when ready by sliding directly onto joint O and a coupling block on link BC. The mating faces of the clamps are shaped to accommodate the curvature of the tibia and femur. Each clamp pair is closed and tightened with four 2-56 UNC screws. In order to allow some culture medium to penetrate the clamped portions of the bones, three sets of 1.25 mm diameter fluid feed holes are drilled through the clamp plates in the areas contacting the joint tissues. The mounting block is used to align the clamps and stifle joint during mounting. It is fabricated such that when interfaced with the clamps and joint, the distance between the clamp faces and the joint's center of rotation is fixed.

4.3   JM2 Drive Motor Control

In order to utilize the JM2, a robust control system had to be developed. Two independent controllers were made for each of the actuators. This section covers the development of the drive motor controller, the more trivial of the two and effectively a speed control problem.

4.3.1   Control Scheme

The flexion drive motor must be controlled for the rotational speed of the output shaft, ω_{AB}, which drives the rate of change of the knee flexion angle and cycle time. The controller is designed such that ω_{AB} may be controlled as a constant value or a function of cycle position or time. A combination of proportional-integral (PI) control and iterative feed forward learning control was used. The controller is set to follow a reference output rotational velocity, ω_{ref}, which may be a function of the output shaft angle, θ_A. A controller block diagram representation is shown in Figure 63. K_P and K_I are the proportional and integral gains respectively. W_{-1}, W_0, and W_{+1}, are weighting factors acting on the feed forward contributions. u_A is the motor input which takes the form of a percent duty cycle scaled from 0-255. θ_A^* is a scaled discretized integer value representing the angular position of the output shaft. The values of θ_A^* repeat every cycle and are relative to the starting position of the motor. The subscript N represents the output shaft cycle count. The subscript k represents the digital control loop iteration.
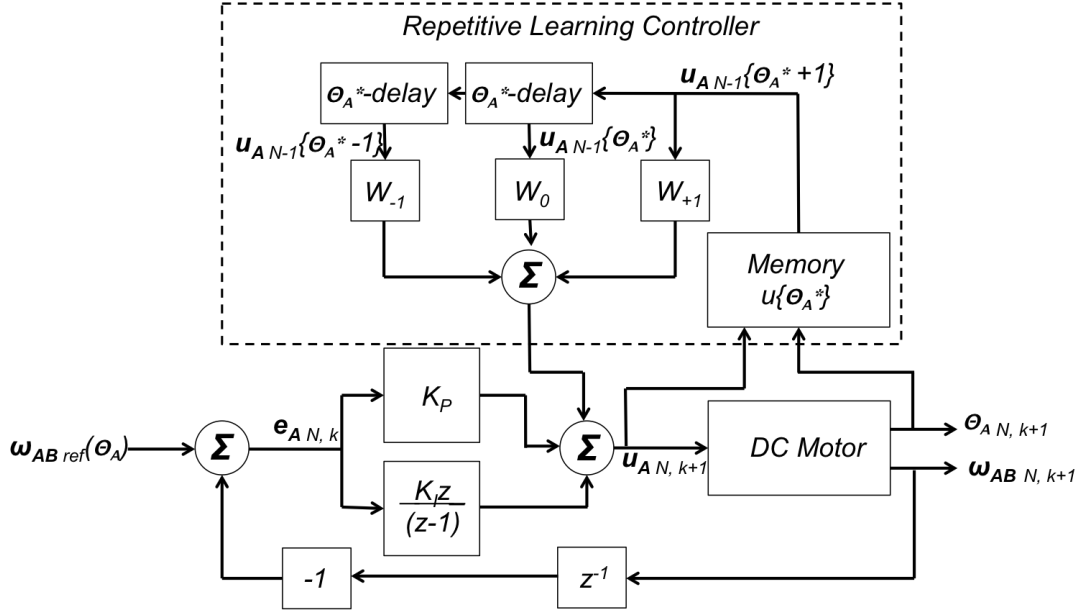
Figure 63: Flexion Drive Motor Controller Block Diagram – The controller used to regulate the speed of the drive motor is based on a standard PI approach supplemented by a repetitive learning controller.

The PI controller acts on an error signal e_A, calculated as the difference between the reference rotational speed ω_{ref} and the actual rotational speed, ω_{AB}, calculated from the Hall-effect encoder signal. The repetitive learning controller calculates a weighted average of the input signal at the current and adjacent values of θ_A^* during the previous cycle iteration. For every value of θ_A^*, the Memory block effectively stores the value of u_A until the following N-cycle iteration. The applied motor input is a sum of the PI controller and learning controller calculated inputs and the resulting expression for motor input u_A for each cycle N and control loop iteration k is given by:

$$u_{A,N,k} = K_P e_{A,N,k} + K_I \sum_{k=0}^{k} e_{A,N,k} + W_{-1} u_{A,N-1}(\theta_A^* - 1) + W_0 u_{A,N-1}(\theta_A^*) + W_{+1} u_{A,N-1}(\theta_A^* + 1) \quad (4.10)$$

The control scheme is executed on an Arduino Uno microcontroller at a 100 Hz sample rate. Appropriate gains were determined experimentally through testing, and no modeling or identification of the drive motor dynamics was found necessary. A flowchart of the system's supporting hardware is shown in Figure 64.
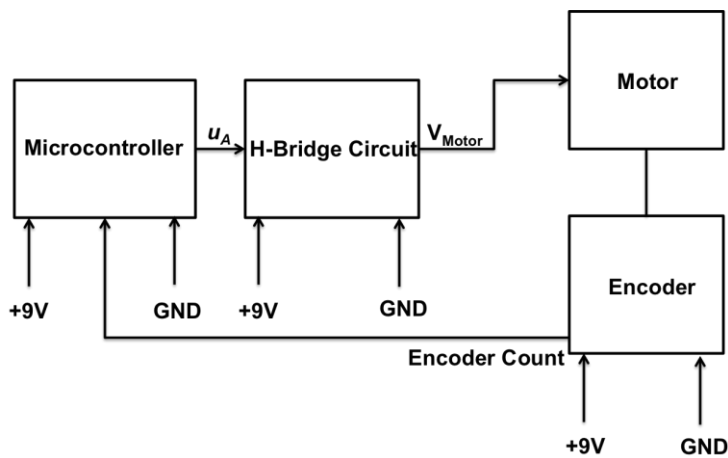
Figure 64: JM2 Drive Motor Hardware Flow Chart – A microcontroller runs the drive motor control scheme and sends a PWM control signal to an H-Bridge circuit. The circuit supplies the motor with the appropriate voltage and current.

The control output is sent to an H-bridge circuit in order to supply adequate current to motor. The supporting hardware is run off of one 9 Volt power supply.

4.3.2 Encoder Count Ambiguity and Compensation

In order to accurately keep track of the number of cycles, a corrective measure must be applied to the encoder count due to the non-integer gear ratio of the motor. This is due

to the fact that the drive motor gear ratio, although expressed in a simplified form as ~47:1, is in fact 5622144:120000. Since the encoder rotates rigidly with the internal shaft, a full rotation of the output shaft does not result in an integer number of encoder counts. Therefore, the exact number of encoder counts per revolution of the output shaft is given by:

$$48 \left(\frac{counts}{internal\ revolution} \right) * \frac{5622144}{120000} \left(\frac{intenal\ revolutions}{output\ revolutions} \right) = 2248.8576 \left(\frac{counts}{output\ revolution} \right)$$

The controller scheme monitors and calculates cycle revolutions assuming a whole number of encoder counts per revolution, due to software programming limitations. Hence, an approximation of *2249 counts/output revolution* is employed (i.e. every 2249 counts, the control system iterates a cycle *N*). Essentially there is an error between *controller counts* and *actual counts.* Consequentially, every cycle, the system effectively assumes it's rotational position as 0.1424 counts ahead of the actual count:

$$2249 \left(\frac{controller\ counts}{cycle} \right) - 2248.8576 \left(\frac{actual\ counts}{cycle} \right) = 0.1424 \left(\frac{extra\ counts}{cycle} \right)$$

If this error is ignored, the system over-estimates its position by 1 encoder value every 7 cycles. Although the error is relatively small, within ~15,742 cycles, the system will have estimated itself to be an entire extra cycle ahead. Considering the system is designed to run over several hours, one could see that at a cycle speed of 0.25 Hz, it would only take 17.5 hours for the system error to accumulate to a full cycle. In order to compensate

for this error, the *controller count* value is decremented by one count every 7 cycles, or every *15,743 controller counts.* This compensation does not completely eliminate the error, but reduces it to a 0.0032 count lag every 7 cycles:

$$\left[2249\left(\frac{controller\ counts}{cycle}\right)*7(cycles)-1(compensation\ count)\right]$$

$$-\left[2248.8576\left(\frac{actual\ counts}{cycle}\right)*7(cycles)\right]=-0.0032\left(\frac{extra\ counts}{7\ cycles}\right)$$

Although the error is relatively small, it still results in the eventual lag of 1 count every 2187.5 cycles. A second compensation is used to completely eliminate the error. Every 2188 cycles and every 4375 cycles, the *controller count* value is incremented by one count. This averages to 1 count added every 2187.5 cycles as needed and the resulting error is completely eliminated after 4375 cycles:

$$4375\ cycles*2248.8576\left(\frac{actual\ counts}{cycle}\right)=9838752\ actual\ counts\ per\ 4375\ cycles$$

$$\left[\left[2249\left(\frac{controller\ counts}{cycle}\right)*7(cycles)-1(compensation\ count)\right]*\frac{2188}{7}(sets\ of\ 7\ cycles)\right.$$

$$\left.+1(compensation\ count)\right]$$

$$+\left[\left[2249\left(\frac{controller\ counts}{cycle}\right)*7(cycles)-1(compensation\ count)\right]\right.$$

$$\left.*\frac{2187}{7}(sets\ of\ 7\ cycles)+1(compensation\ count)\right]$$

$$=9838752\ controller\ counts\ per\ 4375\ cycles$$

Though the original error has a negligible effect on the speed control accuracy, its correction is vital to maintaining an accurate position estimate over long periods of time. The importance of this accuracy is in controlling the loading motor, which is discussed in detail in Chapter 5.

4.4 JM2 Kinematic & Dynamic Analysis

The goal of modeling the JM2 system is to predict the motion and loading profiles in the system. It is particularly aimed at determining the effective loads at the stifle joint articular interface. The model developed in this section accounts for both the drive and loading linkage systems, and is carried out in a manner to give a comprehensive view of the system dynamics.

4.4.1 Derivation of Flexion Angle Profile

In order to define the motion profile of the joint, it is necessary to relate flexion angle to the crank link angle. Again, consider the linkage system in an arbitrary position, where a Cartesian coordinate is defined with its origin at joint A and y-axis inline with L_{OA}. As the motor actuates the system at A, link AB rotates and joint B traces the circular path shown in Figure 65. It is possible to derive an expression for Φ and therefore $\theta_{flexion}$ as a function of θ_A for a given set of link lengths.
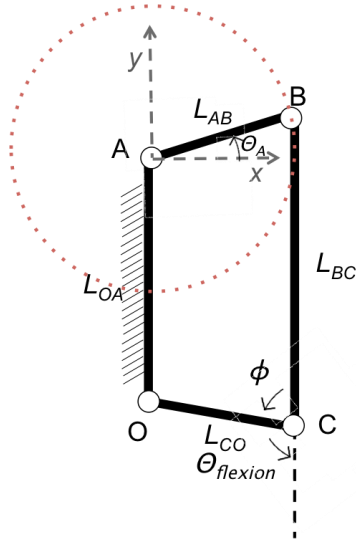
Figure 65: Four Bar Linkage in Arbitrary Position - Cartesian coordinate system is defined with origin at joint A. Joint B traces the dotted circle shown as link AB rotates.

In the coordinate system shown, points A, B and O have the following positions:

$$A(0,0)$$

$$B(L_{AB}\cos(\theta_A), L_{AB}\sin(\theta_A)\}$$

$$O(0,-L_{OA})$$

The distance L_{OB} can be found using the Pythagorean theorem:

$$L_{OB} = \sqrt{(L_{AB}\cos(\theta_A))^2 + (L_{AB}\sin(\theta_A) - L_{OA})^2} \tag{4.11}$$

Equation (4.11) can now be substituted into (4.3):

$$(L_{AB} \cos(\theta_A))^2 + (L_{AB} \sin(\theta_A) - L_{OA})^2 = L_{CO}^2 + L_{BC}^2 - 2L_{CO}L_{BC} \cos(\phi) \qquad (4.12)$$

Solving for ϕ yields:

$$\phi = \cos^{-1}\left(\frac{L_{CO}^2 + L_{BC}^2 - ((L_{AB} \cos(\theta_A))^2 + (L_{AB} \sin(\theta_A) - L_{OA})^2)^2}{2L_{CO}L_{BC}}\right) \qquad (4.13)$$

Using Equation (4.1) the flexion angle $\theta_{flexion}$ can be written as a function of the input angle θ_A:

$$\theta_{flexion} = 180^o - \cos^{-1}\left(\frac{L_{CO}^2 + L_{BC}^2 - ((L_{AB} \cos(\theta_A))^2 + (L_{AB} \sin(\theta_A) - L_{OA})^2)^2}{2L_{CO}L_{BC}}\right) \qquad (4.14)$$

The profiles for the three ranges summarized in Table 9 are plotted graphically in Figure 66. For comparison, images from a fluoroscopic video taken of the JM2 system with a stifle joint shows the actual ranges of motion under the maximum flexion range, Figure 67.
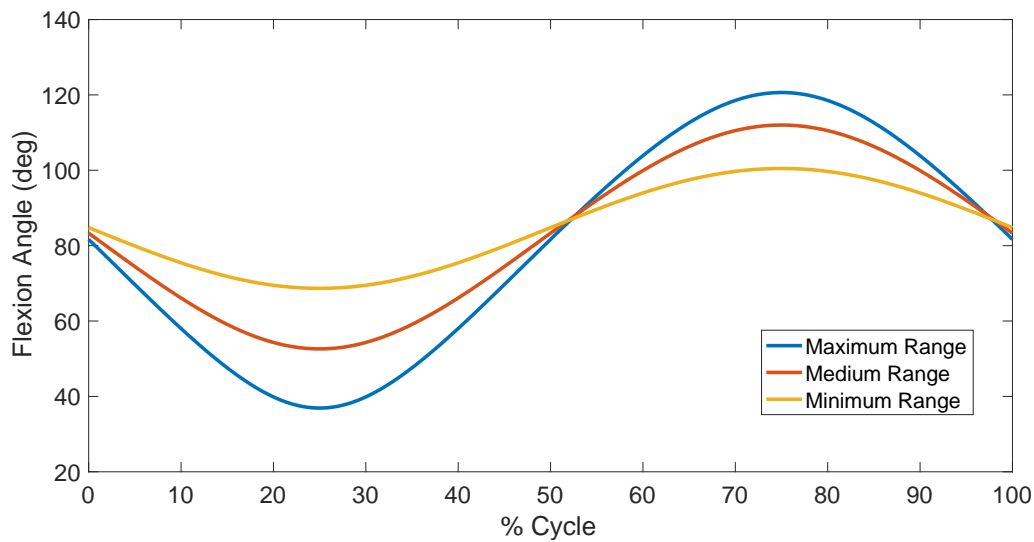
Figure 66: JM2 System Flexion Angle Profiles – Minimum range spans 33 degrees, medium range spans 59 degrees and maximum range spans 83 degrees.
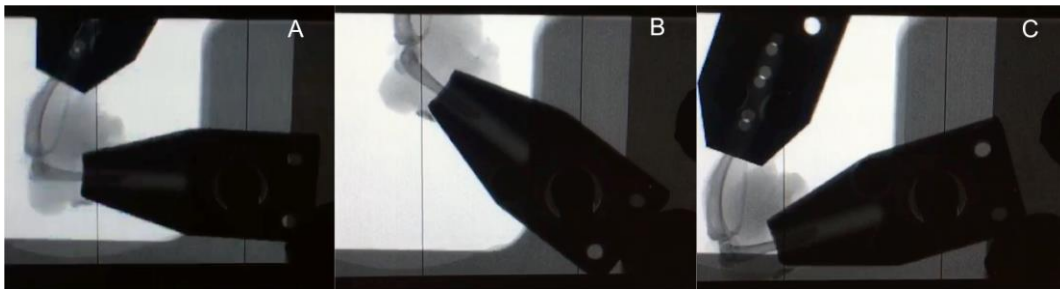
Figure 67: X-Ray Images of Stifle Joint Actuated by JM2 - The full range of an actual joint mounted in a CT-compatible JM2 device under the maximum range of motion; A) 0% of Cycle; B) 25% of Cycle (Minimum Flexion); C) 75% of Cycle (Maximum Flexion)

Qualitative comparison between the predicted and actual motion of the joint, it's clear that the minimum flexion angle is reached. However, Figure 67C indicates that when approaching maximum flexion, elasticity of the bones (particularly the tibia) results in increased curvature and prevents maximum flexion from being reached. The actual

flexion angle is measured utilizing the same system developed in Section 3.3.2, and a comparison of measured and predicted flexion angles are shown in Table 10.

Table 10: JM2: Measured flexion angles and predicted flexion angles

% Cycle	Predicted Flexion Angle	Measured Flexion Angle +/- 1°
0	84°	82°
25	36°	34°
75	120°	95°

A similar trend is seen as with the JM1 device results in Table 4. There is good agreement between the predicted and measured flexion angle at lower flexion states, but the measured angle is lower than expected as the joint is further flexed. Again, this is indicative that towards a higher degree of flexion, there is increased bending in the tibia.

4.4.2 Derivation of JM2 Kinematics and Geometric Paths

The vector paths of all the linkages and joints in the system must be derived and defined in order to fully develop the dynamic model. Effectively, this section defines the kinematics of system. The system only had one degree of freedom, and the entire geometry is defined by the drive motor shaft angle θ_A. A representation of the linkage geometry is shown in below, indicating definitions of joint angles and key coordinates.
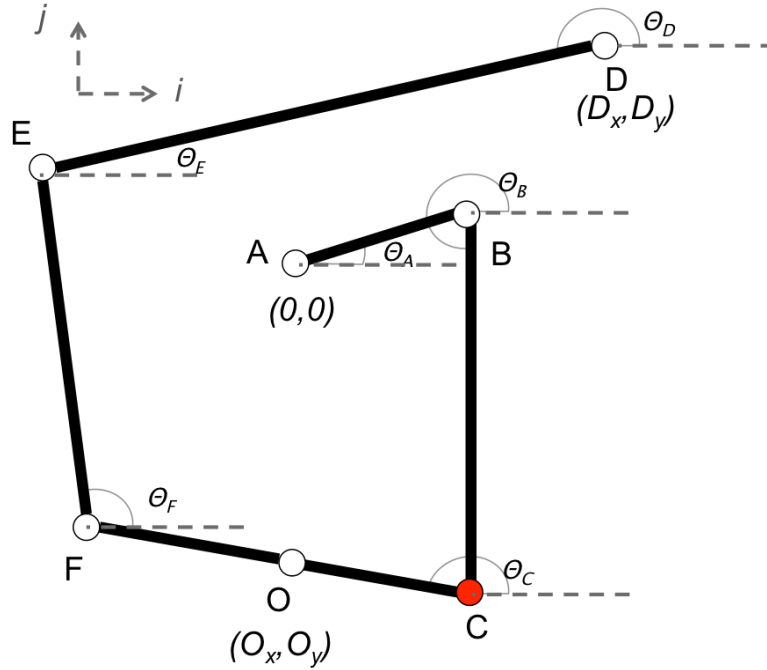
Figure 68: JM2 Kinematic Definitions - Linkage geometry, angle definitions and key coordinates defined with respect to a global coordinate system i-j, with the origin fixed at joint A.

Recall that the explanted stifle joint makes up Joint C. All angles are defined using a right-handed coordinate system and reference the horizontal *i*-direction, and a coordinate system *i-j* is defined as shown. The position of Joint A is defined as the origin. Positions of joints O and D are defined by the design of the system and correspond to the positions of the fulcrum and loading motor respectively. Lengths between consecutive joints are defined clockwise starting from joint A as L_{AB}, L_{BC}, etc.… and are the effective link lengths, defined the design. The length L_{OA} is also defined by the system design, and joint O sits vertically beneath A. The position vectors for each joint can be defined using these design parameters:

$$\vec{A} = \begin{Bmatrix} 0 \\ 0 \end{Bmatrix}$$

$$\vec{B} = \begin{Bmatrix} L_{AB} \cos(\theta_A) \\ L_{AB} \sin(\theta_A) \end{Bmatrix}$$

$$\vec{C} = \left\{ \begin{matrix} L_{CO} \cos(\theta_C - 180) \\ L_{CO} \sin(\theta_C - 180) - L_{OA} \end{matrix} \right\}$$

$$\vec{O} = \left\{ \begin{matrix} 0 \\ -L_{OA} \end{matrix} \right\}$$

$$\vec{F} = \left\{ \begin{matrix} L_{OF} \cos(\theta_C) \\ L_{OF} \sin(\theta_C) - L_{OA} \end{matrix} \right\}$$

$$\vec{E} = \left\{ \begin{matrix} D_X + L_{ED} \cos(\theta_D) \\ D_Y + L_{ED} \sin(\theta_D) \end{matrix} \right\}$$

$$\vec{D} = \left\{ \begin{matrix} D_X \\ D_Y \end{matrix} \right\}$$

Furthermore, the positions of the center of gravity of each link can be estimated. By assuming that the center of gravity of each link is a known length notated as Lnm^G for each link from a joint n to a joint m. For example, the convention for link AB is shown in Figure 69.
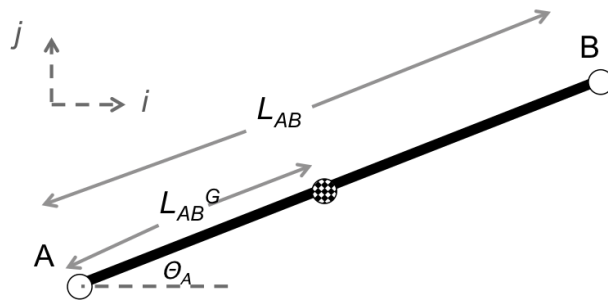
Figure 69: Center of Gravity Notation and Location

The center gravity position vectors are expressed as:

$$\vec{AB}_{CG} = \left\{ \begin{array}{l} L_{AB}^G \cos(\theta_A) \\ L_{AB}^G \sin(\theta_A)\, 0 \end{array} \right\}$$

$$\vec{BC}_{CG} = \left\{ \begin{array}{l} \vec{B} \cdot \hat{\imath} + L_{BC}^G \cos(\theta_B) \\ \vec{B} \cdot \hat{\jmath} + L_{BC}^G \sin(\theta_B) \end{array} \right\}$$

$$\vec{CF}_{CG} = \left\{ \begin{array}{l} \vec{C} \cdot \hat{\imath} + L_{CF}^G \cos(\theta_C) \\ \vec{C} \cdot \hat{\jmath} + L_{CF}^G \sin(\theta_C) \end{array} \right\}$$

$$\vec{FE}_{CG} = \left\{ \begin{array}{l} \vec{F} \cdot \hat{\imath} + L_{FE}^G \cos(\theta_F) \\ \vec{F} \cdot \hat{\jmath} + L_{FE}^G \sin(\theta_F) \end{array} \right\}$$

$$\vec{ED}_{CG} = \left\{ \begin{array}{l} \vec{E} \cdot \hat{\imath} + L_{ED}^G \cos(\theta_E) \\ \vec{E} \cdot \hat{\jmath} + L_{ED}^G \sin(\theta_E) \end{array} \right\}$$

Using formulations for the joint paths, expressions for each joint angle can be found. The method used to derive these expressions involves considering vector loops around the geometry similarly to the method used in Sections 3.3.1 and 3.3.3. For the sake of brevity, the full derivations are not show here and only the resulting expressions are presented and plotted for the medium flexion range geometry for a constant cycle speed in Figure 70.

$$\theta_C = 180^0 + \sin^{-1}\left(\frac{K_3}{\sqrt{K_1^2 + K_2^2}}\right) - \tan^{-1}\frac{K_1}{K_2} \tag{4.15}$$

$$Where:$$

$$K_1 \stackrel{\text{def}}{=} 2L_{CO}L_{AB}\cos(\theta_A)$$

$$K_2 \stackrel{\text{def}}{=} 2L_{CO}L_{AB}\sin(\theta_A) + 2L_{CO}L_{OA}$$

$$K_3 \overset{\text{def}}{=} L_{CO}^2 + L_{AB}^2 + L_{OA}^2 - L_{BC}^2 + 2L_{OA}L_{AB}\sin(\theta_A)$$

$$\theta_B = \cos^{-1}\left(\frac{L_{CO}\cos(\theta_C - 180^O) - L_{AB}\cos(\theta_A)}{L_{BC}}\right) \tag{4.16}$$

$$\theta_D = \sin^{-1}\left(\frac{K_6}{\sqrt{K_4^2 + K_5^2}}\right) - \tan^{-1}\frac{K_4}{K_5} \tag{4.17}$$

Where:

$$K_4 \overset{\text{def}}{=} 2L_{ED}L_{FO}\cos(\theta_C) - 2D_xL_{ED}$$

$$K_5 \overset{\text{def}}{=} 2L_{ED}L_{FO}\sin(\theta_C) + 2L_{ED}L_{OA} - 2D_yL_{ED}$$

$$K_6 \overset{\text{def}}{=} L_{OA}^2 + D_x^2 + D_y^2 + L_{ED}^2 + L_{FO}^2 - L_{FE}^2 - 2D_xL_{FO}\cos(\theta_C) - 2D_yL_{FO}\sin(\theta_C)$$
$$+ 2D_YL_{OA} - 2L_{OA}L_{FO}\sin(\theta_C)$$

$$\theta_F = \cos^{-1}\left(\frac{D_x + L_{ED}\cos(\theta_D) - L_{FO}\cos(\theta_C)}{L_{EF}}\right) \tag{4.18}$$
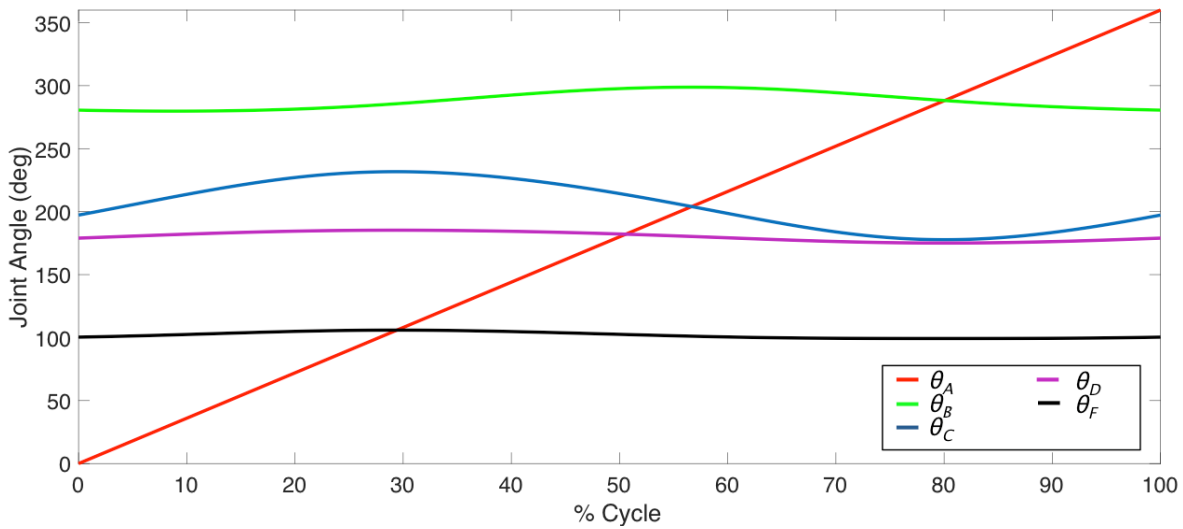
Figure 70: Profiles of All JM2 Linkage Joint Angles – The angles of each joint a derived by the kinematic modeling and can be expressed as function of % cycle.

All angles are functions of the drive shaft angle θ_A, but due to the complexity of the expressions, it is unfeasible to express them explicitly in terms of θ_A. The kinematics of the system is fully defined by Equation (4.15) through (4.18) and can be used to determine the necessary reaction forces, internal forces and drive motor torque under conditions where a defined cycle rate is implemented.

4.4.3 Derivation of Dynamic Model & Joint Forces

With the kinematics fully defined, it is possible to develop a comprehensive model of the system dynamics. The model derived here assumes that the drive motor angle profile is a defined function of time, $\theta_A(t)$, essentially assuming that the drive motor control perfectly actuates the system for a defined profile. The dynamic model is derived using an Euler-Newton formulation, treating the system as 2 dimensional. It was determined that such an approach, although tedious and more involved, is superior to using an energy method (e.g. Lagrange's method or Kane's method) because it can be used to determine

all the internal forces. The knowledge of internal forces is critical to predicting the forces at the stifle joint. A full system model is derived by force and moment balance of each link assuming known kinematics. For example, a free body diagram of link AB is shown in Figure 71.
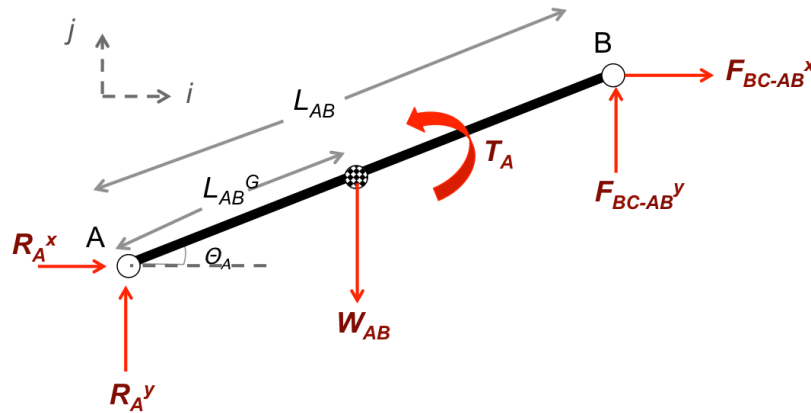
Figure 71: Link AB Free Body Diagram – A free body diagram of link AB showing reaction forces at A, weight acting and the center of gravity, applied motor torque and joint forces at B.

All force and moment balance equations are written in the global *i-j* coordinate system. R_A^x and R_A^y are the reaction forces in the *i* and *j* directions respectively. W_{AB} is the weight of the link, acting at the center of gravity. T_A is the applied drive motor torque at joint A. F_{BC-AB}^x and F_{BC-AB}^y are the joint forces applied by link BC on link AB at their mating joint B in the *i* and *j* directions respectively. For link AB the resulting equations of motion are:

$$\sum_{AB} F_i = R_A^x + F_{BC-AB}^x = \frac{d^2}{dt^2}(\overrightarrow{AB}_{CG} \cdot \hat{\imath})m_{AB} \qquad (4.19)$$

$$\sum_{AB} F_j = R_A^y - W_{AB} + F_{BC-AB}^y = \frac{d^2}{dt^2}(\overrightarrow{AB}_{CG} \cdot \hat{\jmath})m_{AB} \qquad (4.20)$$

$$\sum_{AB} M_A = -W_{AB}L_{AB}^G \cos(\theta_A) + F_{BC-AB}^y L_{AB} \cos(\theta_A) - F_{BC-AB}^x L_{AB} \sin(\theta_A)$$

$$= \frac{d^2}{dt^2}(\theta_A)I_{AB}^A \qquad (4.21)$$

Where m_{AB} is the mass of link AB and I_{AB}^A is the moment of inertia of link AB about A. Using similar notation for mass terms, moment of inertia terms, reaction forces and joint forces, the equations of motion for the other links can be derived as follows:

For link BC:

$$\sum_{BC} F_i = F_{AB-BC}^x + F_{CF-BC}^x = \frac{d^2}{dt^2}(\overrightarrow{BC}_{CG} \cdot \hat{\imath})m_{BC} \qquad (4.22)$$

$$\sum_{BC} F_j = F_{AB-BC}^y + F_{CF-BC}^y - W_{BC} = \frac{d^2}{dt^2}(\overrightarrow{BC}_{CG} \cdot \hat{\jmath})m_{BC} \qquad (4.23)$$

$$\sum_{BC} M_B = -W_{BC}L_{BC}^G \cos(\theta_B) + F_{CF-BC}^y L_{BC} \cos(\theta_B) - F_{CF-BC}^x L_{BC} \sin(\theta_B) + T_A$$

$$= \frac{d^2}{dt^2}(\theta_B)I_{BC}^B \qquad (4.24)$$

For link CF:

$$\sum_{CF} F_i = F_{BC-CF}^x + F_{EF-CF}^x + R_O^x = \frac{d^2}{dt^2}(\overrightarrow{CF}_{CG} \cdot \hat{\imath})m_{CF} \qquad (4.25)$$

$$\sum_{CF} F_j = F^y_{BC-CF} + F^y_{EF-CF} - W_{CF} + R^y_O = \frac{d^2}{dt^2}(\overrightarrow{BC}_{CG} \cdot \hat{j})m_{CF} \tag{4.26}$$

$$\sum_{CF} M_C = -W_{CF}L^G_{CF}\cos(\theta_C) + R^y_O\cos(\theta_C) - R^x_O L_{CO}\sin(\theta_C) + F^y_{EF-BCF}L_{CF}\cos(\theta_C)$$

$$- F^x_{EF-CF}L_{CF}\sin(\theta_C) = \frac{d^2}{dt^2}(\theta_C)I^C_{CF} \tag{4.27}$$

For link FE:

$$\sum_{FE} F_i = F^x_{ED-FE} + F^x_{CF-FE} = \frac{d^2}{dt^2}(\overrightarrow{FE}_{CG} \cdot \hat{i})m_{FE} \tag{4.28}$$

$$\sum_{FE} F_j = F^y_{ED-FE} + F^y_{CF-FE} - W_{FE} = \frac{d^2}{dt^2}(\overrightarrow{FE}_{CG} \cdot \hat{j})m_{FE} \tag{4.29}$$

$$\sum_{FE} M_F = -W_{FE}L^G_{FE}\cos(\theta_F) + F^y_{ED-FE}L_{FE}\cos(\theta_F) - F^x_{EF-FE}L_{FE}\sin(\theta_F)$$

$$= \frac{d^2}{dt^2}(\theta_F)I^F_{FE} \tag{4.30}$$

Finally, for link ED:

$$\sum_{ED} F_i = R^x_D + F^x_{FE-ED} = \frac{d^2}{dt^2}(\overrightarrow{ED}_{CG} \cdot \hat{i})m_{ED} \tag{4.31}$$

$$\sum_{ED} F_j = R^y_D - W_{ED} + F^y_{FE-ED} = \frac{d^2}{dt^2}(\overrightarrow{ED}_{CG} \cdot \hat{j})m_{ED} \tag{4.32}$$

$$\sum_{ED} M_E = -W_{ED} L_{ED}^G \cos(\theta_E) + R_D^y L_{ED} \cos(\theta_E) - R_D^x L_{ED} \sin(\theta_E) + T_D$$

$$= \frac{d^2}{dt^2}(\theta_E) I_{ED}^E \tag{4.33}$$

Equations (4.19) to (4.33) can be written as system of 15 equations and 15 unknowns, once it is recognized that joint forces must be equal and opposite. For example:

$$F_{BC-AB}^x = -F_{AB-BC}^x$$

Therefore, the system of equations can simply be expressed as:

$$\boldsymbol{B = AX} \tag{4.34}$$

Where **X** is a vector of unknown parameters, including the drive motor torque and all joint forces, **B** is a vector of known parameters, including the kinematics, link masses and loading motor torque, and **A** is a matrix describing the system dynamics:

$$X = \begin{bmatrix} T_A \\ R_A^x \\ R_A^y \\ F_{BC-AB}^x \\ F_{BC-AB}^y \\ F_{CF-BC}^x \\ F_{CF-BC}^y \\ R_O^x \\ R_O^y \\ F_{FE-CF}^x \\ F_{FE-CF}^y \\ F_{ED-FE}^x \\ F_{ED-FE}^y \\ R_D^x \\ R_D^y \end{bmatrix}$$

$$B = \begin{bmatrix} \dfrac{d^2}{dt^2}(A\vec{B}_{CG} \cdot \hat{i})m_{AB} \\[2ex] \dfrac{d^2}{dt^2}(A\vec{B}_{CG} \cdot \hat{j})m_{AB} + W_{AB} \\[2ex] \dfrac{d^2}{dt^2}\theta_A + W_{AB}L_{AB}^G \cos(\theta_A) \\[2ex] \dfrac{d^2}{dt^2}(B\vec{C}_{CG} \cdot \hat{i})m_{BC} \\[2ex] \dfrac{d^2}{dt^2}(B\vec{C}_{CG} \cdot \hat{j})m_{BC} + W_{BC} \\[2ex] \dfrac{d^2}{dt^2}\theta_{BC} + W_{BC}L_{BC}^G \cos(\theta_B) \\[2ex] \dfrac{d^2}{dt^2}(C\vec{F}_{CG} \cdot \hat{i})m_{CF} \\[2ex] \dfrac{d^2}{dt^2}(C\vec{F}_{CG} \cdot \hat{j})m_{CF} + W_{CF} \\[2ex] \dfrac{d^2}{dt^2}\theta_{CF} + W_{CF}L_{CF}^G \cos(\theta_C) \\[2ex] \dfrac{d^2}{dt^2}(F\vec{E}_{CG} \cdot \hat{i})m_{FE} \\[2ex] \dfrac{d^2}{dt^2}(F\vec{E}_{CG} \cdot \hat{j})m_{FE} + W_{FE} \\[2ex] \dfrac{d^2}{dt^2}\theta_{FE} + W_{FE}L_{FE}^G \cos(\theta_F) \\[2ex] \dfrac{d^2}{dt^2}(E\vec{D}_{CG} \cdot \hat{i})m_{ED} \\[2ex] \dfrac{d^2}{dt^2}(E\vec{D}_{CG} \cdot \hat{j})m_{ED} + W_{ED} \\[2ex] \dfrac{d^2}{dt^2}\theta_{ED} + W_{ED}L_{ED}^G \cos(\theta_E) - T_D \end{bmatrix}$$

$$
A = \begin{bmatrix}
0 & 1 & 0 & 1 & 0 & 0 & 0 & 0 & 0 & 0 & 0 & 0 & 0 & 0 & 0 \\
0 & 0 & 1 & 0 & 1 & 0 & 0 & 0 & 0 & 0 & 0 & 0 & 0 & 0 & 0 \\
1 & 0 & 0 & -L_{AB}\sin(q_A) & L_{AB}\cos(q_A) & 0 & 0 & 0 & 0 & 0 & 0 & 0 & 0 & 0 & 0 \\
0 & 0 & 0 & -1 & 0 & 1 & 0 & 0 & 0 & 0 & 0 & 0 & 0 & 0 & 0 \\
0 & 0 & 0 & 0 & -1 & 0 & 1 & 0 & 0 & 0 & 0 & 0 & 0 & 0 & 0 \\
0 & 0 & 0 & 0 & 0 & -L_{BC}\sin(q_B) & L_{BC}\cos(q_B) & 0 & 0 & 0 & 0 & 0 & 0 & 0 & 0 \\
0 & 0 & 0 & 0 & 0 & -1 & 0 & 1 & 0 & 1 & 0 & 0 & 0 & 0 & 0 \\
0 & 0 & 0 & 0 & 0 & 0 & -1 & 0 & 1 & 0 & 1 & 0 & 0 & 0 & 0 \\
0 & 0 & 0 & 0 & 0 & 0 & 0 & -L_{CO}\sin(q_C) & L_{CO}\cos(q_C) & -L_{CF}\sin(q_C) & L_{CF}\cos(q_C) & 0 & 0 & 0 & 0 \\
0 & 0 & 0 & 0 & 0 & 0 & 0 & 0 & 0 & -1 & 0 & 1 & 0 & 0 & 0 \\
0 & 0 & 0 & 0 & 0 & 0 & 0 & 0 & 0 & 0 & -1 & 0 & 1 & 0 & 0 \\
0 & 0 & 0 & 0 & 0 & 0 & 0 & 0 & 0 & 0 & 0 & L_{FE}\sin(q_F) & L_{FE}\cos(q_F) & 0 & 0 \\
0 & 0 & 0 & 0 & 0 & 0 & 0 & 0 & 0 & 0 & 0 & -1 & 0 & 1 & 0 \\
0 & 0 & 0 & 0 & 0 & 0 & 0 & 0 & 0 & 0 & 0 & 0 & -1 & 0 & 1 \\
0 & 0 & 0 & 0 & 0 & 0 & 0 & 0 & 0 & 0 & 0 & 0 & 0 & -L_{ED}\sin(q_E) & -L_{ED}\cos(q_E)
\end{bmatrix}
$$

The system of equations must be solved numerically due to the complexity of the kinematic angle relationships, specifically due to difficulty in taking necessary time derivatives of the joint angle functions (4.15) through (4.18). A numeric solver was written using MATLAB (Mathworks, Natick, MA, USA) and can be run to determine all the components in vector **X**. Each term is a function of geometry, which in turn is a function of time.

The primary interest in developing a full dynamic model is to predict the forces experienced by the stifle joint as a function of time. The stifle joint are simply the internal forces at joint C, given by F_{C0F-BC}^{x} and F_{CF-BC}^{y} in the global coordinate system. They can be converted to the femoral coordinate frame, dubbed $\widehat{a_1}$-$\widehat{a_2}$, (shown in Figure 72) as follows:
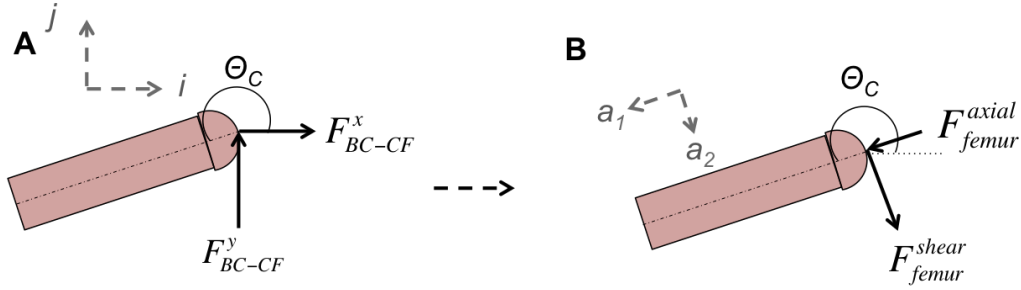
Figure 72: Coordinate Transform of Stifle Joint Forces – Convention for transforming joint forces derived in A) the global frame to B) the femoral frame

$$F_{femur}^{axial} = F_{BC-CF}^{x} \cos(\theta_C) + F_{BC-CF}^{y} \sin(\theta_C) \qquad (3.35)$$

$$F_{femur}^{shear} = -F_{BC-CF}^{x} \sin(\theta_C) + F_{BC-CF}^{y} \cos(\theta_C) \qquad (3.36)$$

The sign convention is such that a positive axial force indicates compression of the femur, and a positive shear force indicates shear action in the ventral direction on the femoral surface. The axial and shear loads at the femur can now be predicted by assigning values to the system properties. Three major assumptions are made: 1) all links are assumed as simple shapes for moment of inertia calculations; 2) the centers of mass of all links are at the middle of the link length, with the exception of link AB which has a square shape, and hence its0 center of mass is assumed at joint A; 3) the mechanical links are the dominant sources of inertia in the system and contributions of the stifle joint to mass and moment of inertia terms are negligible. Properties are summarized in Table 11. Shape assumptions are compared the actual assembled link shapes in Appendix C.

Table 11: JM2 length and inertia properties

Link	Mass (kg)	Length (m)	Shape Assumption
AB	0.015	0.0114	Square Plate Side length = 31.7 mm
BC	0.010	0.0698	Thin Rectangular Plate Length = 70.7 mm Width = 12.9mm
CF	0.005	0.0540	Thin Rectangular Plate Length = 54.1 mm Width = 12.1 mm
FE	0.015	0.0953	Thin Rectangular Plate Length = 102.0 mm Width = 10.7 mm
ED	0.055	0.1460	Thin Rectangular Plate Length = 151.2 mm Width = 12.4 mm

The predicted femoral loads shown in Figure 73, Figure 74, Figure 75 and Figure 76 for shear and axial loads for the case where the system is fully assembled, and the case where only the drive linkage system is assembled. These results indicate the expected loads when the system is operated under constant angular rotation of the drive motor shaft at 0.25 Hz in the clockwise direction. No active loading applied at the loading motor.
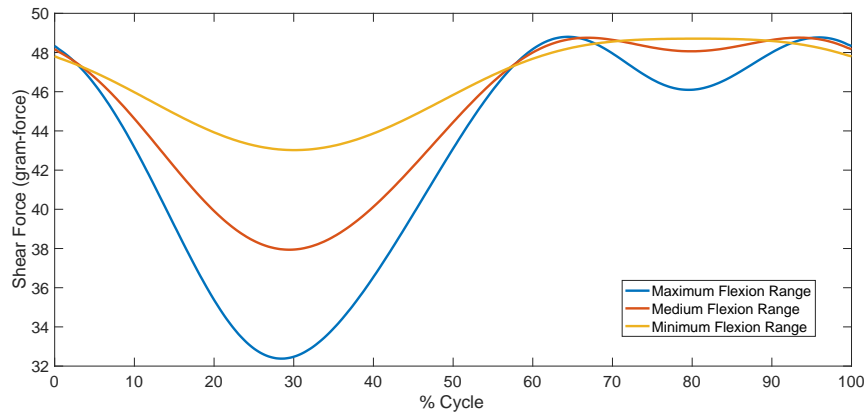
Figure 73: Shear Force Profile in Femoral Frame with Full Linkage Assembly Attached
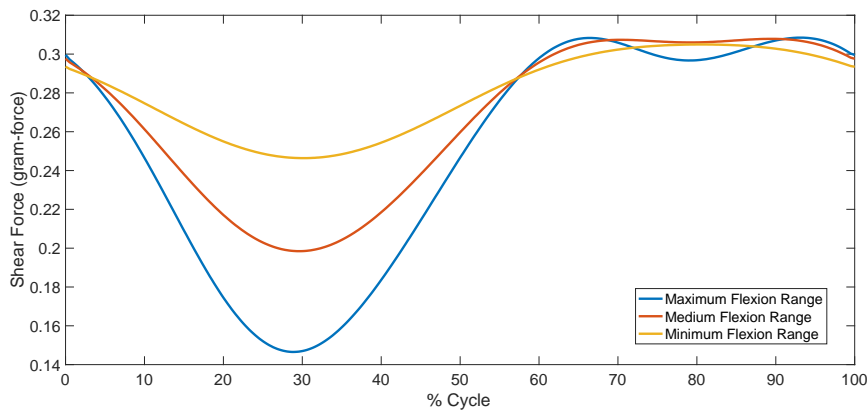
Figure 74: Shear Force Profile in Femoral Frame with Only Drive Linkage Assembly Attached
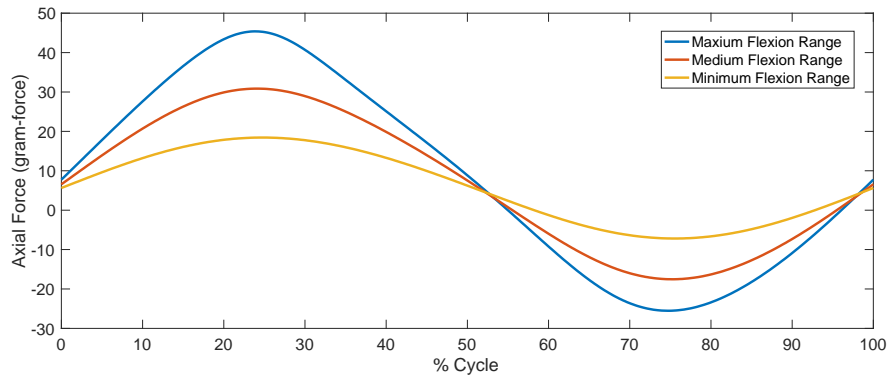
Figure 75: Axial Force Profile in Femoral Frame with Full Linkage Assembly Attached
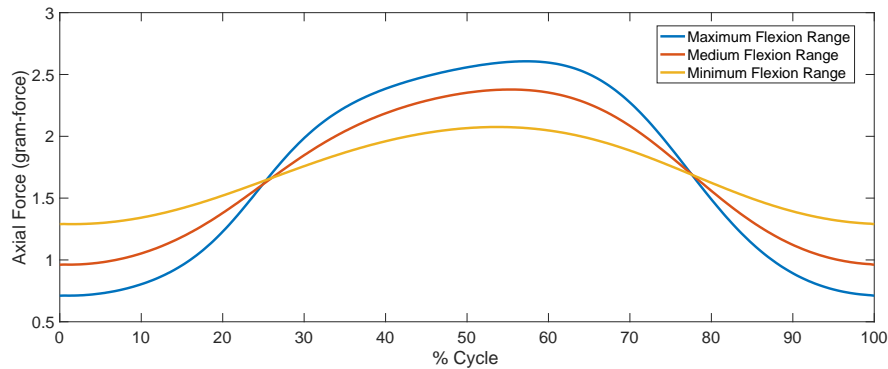
Figure 76: Axial Force Profile in Femoral Frame with Only Drive Linkage Assembly Attached

The predictions indicate that when the system is fully assembled, both shear and axial loads are significantly increased. This is an intuitive result considering that the loading linkage system adds considerable mass to the system that needs to be actuated. The profiles shown here represent the "passive loading" function of the JM2 system (i.e. the loading motor is not driven). The model also does not take into account friction within the joints, which may contribute to increasing loads and have transient properties as the system is run and maintained in the incubator.

4.5 Experimental Use of the JM2 – Investigation of Flexion Rate & Profile

The JM2 system was utilized to investigate the effects on flexion rate and profile on explanted joints. For all experiments the system was used as shown in Figure 58C, with only the drive linkage system attached and no active loading implemented. Six JM2 systems were used in parallel for experiments, Figure 77. The overall purpose of these experiments was to demonstrate that a range of damage to the articular surface can be created using the JM2 system in a passive loading configuration.
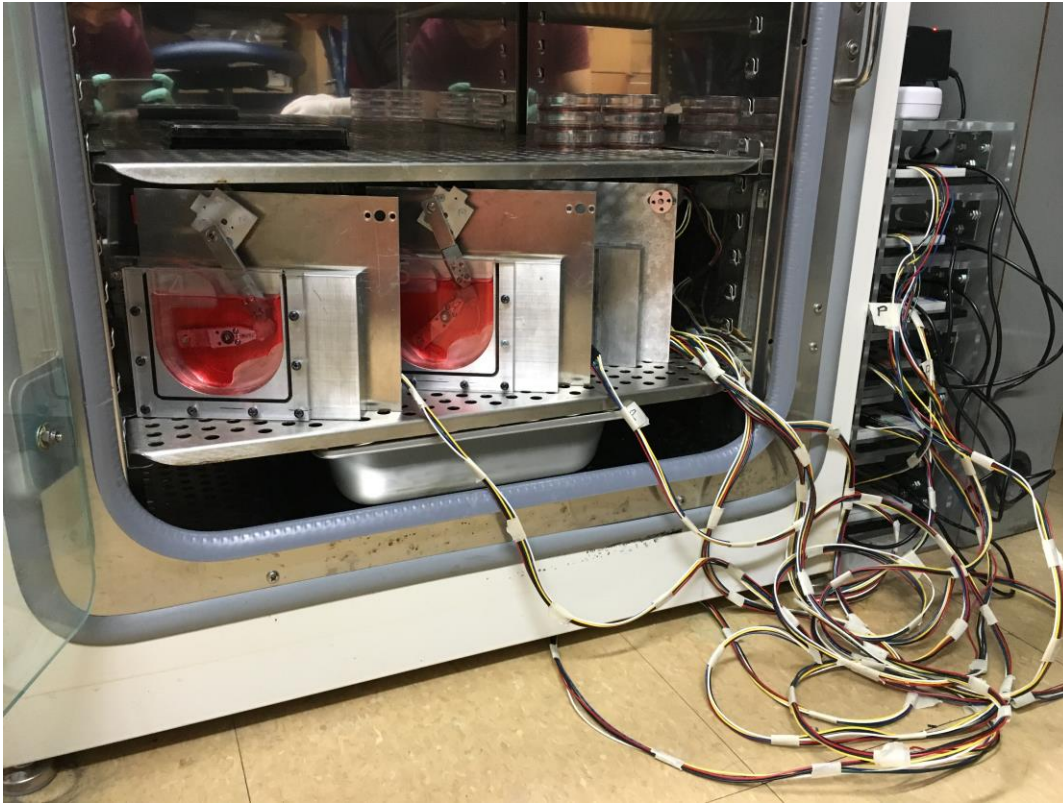
Figure 77: JM2 Device in Incubator - Photograph showing several JM2 systems running in parallel

Two sets of experiments were run: the first was pilot testing aimed at looking at the effects of flexion cycle rate and culture duration on different strains of mice, with the goal of determining appropriate culture duration and actuation frequency; and the second was aimed at looking the effects of flexion cycle profile in terms active actuation time and resting time. All experiments were run using the medium flexion angle range configuration.

4.5.1 Joint Preparation

The pilot investigation into cycle rate was performed using 12-13 week old $NF_{\kappa}B$/Balb C and CD-1 mice. Investigation into cycle profile was performed on 13-week old CD-1 mice. Mice were sacrificed and rear stifle joints were surgically isolated using the procedures detailed in 3.4.1. A mix of female and male mice were used for pilot testing, while only female

mice were used for the investigation into cycle profile due to availability. Stifle joint's were mounted such that the tibia aligns with the link BC, resulting in a motion similar to a bicycle.

4.5.2 Sterility Measures

The same sterility measures outlined in 3.4.2 were employed for all experiments.

4.5.3 Histological Assessment Methods

Following culture, samples were processed and prepared for histology using the methods outlined in Section 3.4.4. Samples were stained with the Safranin-O/Fast Green protocol outline in Appendix B. Qualitative analysis was not utilized due to an inability to identify suitable representative images. Rather, quantitative analysis in accordance with OARSI scoring method described in Figure 47 was used. Only tibial scores are presented due to the limitations of femoral scores established in Section 3.4.6. Significant differences are determined by performing select comparisons using the Mann-Whitney U test for direct comparisons of pairs of groups, and the Kruskal-Wallis test followed by Dunn's Multiple Comparison test where appropriate. P-values below 0.05 are considered statistically significant.

4.5.4 Pilot Testing - Culture Conditions

As stated previously, two sets of experiments were run investigating different aspects of culture and actuation conditions. The first round effectively served as pilot tests to gauge the effects of the system on two different mouse strains, altering the culture time and cycle frequency. The conditions are outlined in Table 12, and compare samples taken from both

NF$_κ$B/Balb C and CD-1 mice cultured in the JM2 system under 0.25 Hz and 0.50 Hz cycles for either 7 or 14 days. All joints were maintained in DMEM solution at the low glucose level (1.0 mg/ml concentration) discussed in 3.4.

Table 12: Pilot Testing Culture Conditions

Strain	Condition	Number of Samples	Culture Time (days)
CD-1	0.25 Hz	3	7
CD-1	0.5 Hz	3	7
CD-1	Static	2	7
CD-1	0.25 Hz	2	14
CD-1	0.5 Hz	3	14
CD-1	Static	2	14
NF$_κ$B/Balb C	0.25 Hz	2	7
NF$_κ$B/Balb C	0.5 Hz	3	7

Only two to three samples were tested per condition, as the goal of the experiments was not to determine significant differences, but to provide guidance for suitable strains, cycle frequencies and culture times for flexion cycle profile experiments. All actuated samples were subject 8 hours of motion, followed by a 16-hour resting phase.

4.5.5 Pilot Testing – Results

The mean tibia OARSI scores for all samples taken from CD-1 mice are shown in Figure 78. The comparisons show samples cultured statically, and dynamically under 0.25 Hz and 0.50 Hz cycle frequencies for both 7 and 14 days. No statistical testing was performed due to the low number of samples in each category (*n=2-3*).
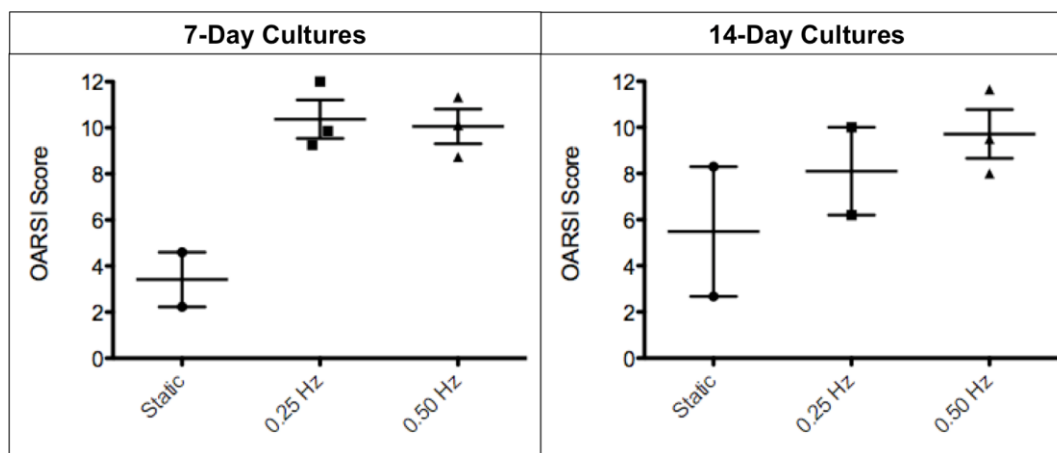
Figure 78: Pilot Testing Results of Joints Taken from CD-1 Mice– Dot plots of tibial scores showing observations, mean score per condition and standard error of the mean as error bars; no statistical testing was performed due to the low samples numbers. Observation indicates that both at 7 and 14 days, dynamic actuation leads to an increase in OARSI score.

Despite the small number of samples, the results suggest that the dynamic actuation does induce a higher degree of staining loss. However, there is no clear difference between samples actuated at 0.25 Hz and 0.50 Hz for 8 hours a day, indicating that even at the lower rate of 0.25 Hz the motion results in an effectively saturated OARSI score. This is supported also by the lack of increase in score that would be expected due to an increase in culture time.

Comparisons of mean tibial OARSI scores obtained from CD-1 and $NF_\kappa B$/Balb C mice cultured for 7 days under dynamic actuation at 0.25 Hz and 0.5 Hz are shown in Figure 79. Again, no statistical analysis was performed due to the low number of samples.
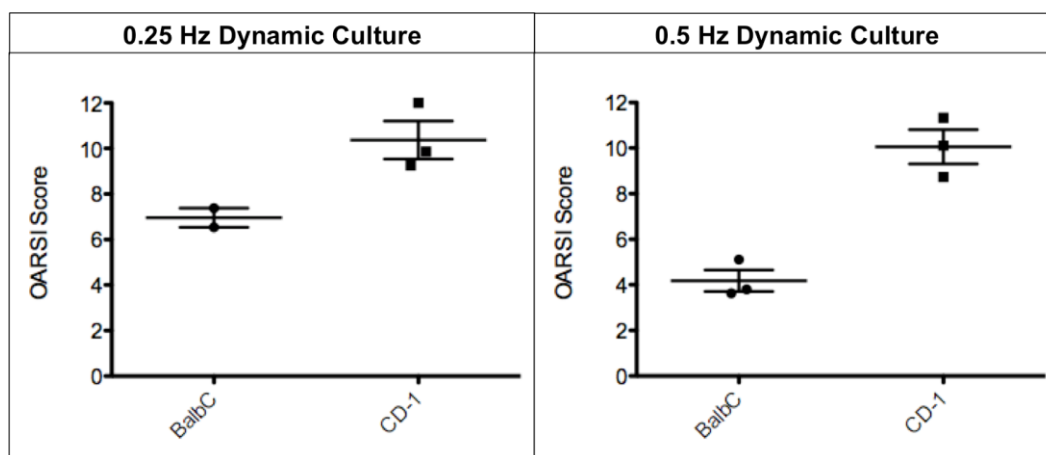
Figure 79: Pilot Testing Results Comparing Joints Taken from CD-1 and BalbC Mice– Dot plots of tibial scores showing observations, mean score per condition and standard error of the mean as error bars; no statistical testing was performed due to the low samples numbers. Observation indicates that both at 0.25 Hz and 0.50 Hz dynamic actuation, samples taken from CD-1 mice tend to score higher than those taken from BalbC mice.

There is an evident difference in scores between CD-1 and NF$_\kappa$B/Balb C samples, with CD-1 scores being markedly lower. Also evident, is the lack of difference in score between the two cycle frequencies. This again indicates that both cycle rates result in a rigorous amount of activity and result in an extreme amount of damage to the articular matrix.

4.5.6 Activity Cycle Profile Investigation – Culture Conditions

Based on the results of the pilot testing, it was determined that both 0.25 Hz and 0.50 Hz cycle rates at 8 hours/day are too aggressive for a representative culture. This led to an interest in investigating another aspect of the dynamic activity cycle profile: relative activity and rest durations. Two cycle profiles were chosen for comparison, represented graphically in Figure 80.

a) Continuous Activity Cycle

| 2 Hours Active | 22 Hours Rest |

b) Intermittent Activity Cycle

| 1 Hour Active | 11 Hours Rest | 1 Hour Active | 11 Hours Rest |

c) Pilot Test Activity Cycle

| 8 Hours Active | 16 Hours Rest |
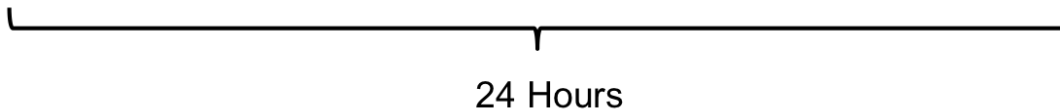
24 Hours

Figure 80: JM2 Activity Cycle Profiles – The division of 24 hour periods into active and resting times; a) Continuous activity is defined as 2 hours of actuation followed by 22 hours of rest; b) Intermittent activity is defined as two consecutive series of 1 hour of activity followed by 11 hours of rest; c) Cycle used in pilot testing that involved 8 hours of activity followed by 16 hours of rest.

The dynamic activity cycles are designed dividing a 24-hour period into sub-periods of activity (i.e. actuation at a 0.25 Hz flexion rate) and rest. The continuous cycle is designed as 2 hours of activity followed by 22 hours of resting. The intermittent cycle is designed as two repetitions of a single hour of activity followed by 11 hours of rest. For comparison, the cycle used in the pilot tests, 8 hours of activity followed by 16 hours of rest, is shown in Figure 80C. Both the continuous and intermittent cycles have the same amount of active time divided into different sub-periods.

Six joints were cultured under the continuous activity condition and six others were culture under the intermittent condition. As control groups, eight joints were evenly divided into two groups dubbed "continuous rotation" and "intermittent rotation", where samples were

maintained in petri dishes on top of a rotating table. The rotating table was only turned on during "active" cycles in the respective continuous and intermittent conditions. A summary of joints per condition is presented in Table 13.

Table 13: Summary of samples per condition in activity cycle investigation.

Condition	Number of Samples
Dynamic Continuous	6
Dynamic Intermittent	6
Rotation Continuous	4
Rotation Intermittent	4

In total 20 joints were used. All joints were taken from 13-week-old female CD-1 mice. CD-1 mice were chosen over $NF_\kappa B$/Balb C based on the results of the pilot tests, suggesting a higher sensitivity to the effects of dynamic actuation. Female mice were used due to availability. All samples were cultured for 7 days in low glucose (1.0 mg/ml) DMEM solution. Medium was replaced once during the course of experiments, on the third or fourth day following culture initiation.

4.5.7 Activity Cycle Profile Investigation – Results

The resulting mean tibial OARSI scores for each of the four conditions are shown in Figure 81.
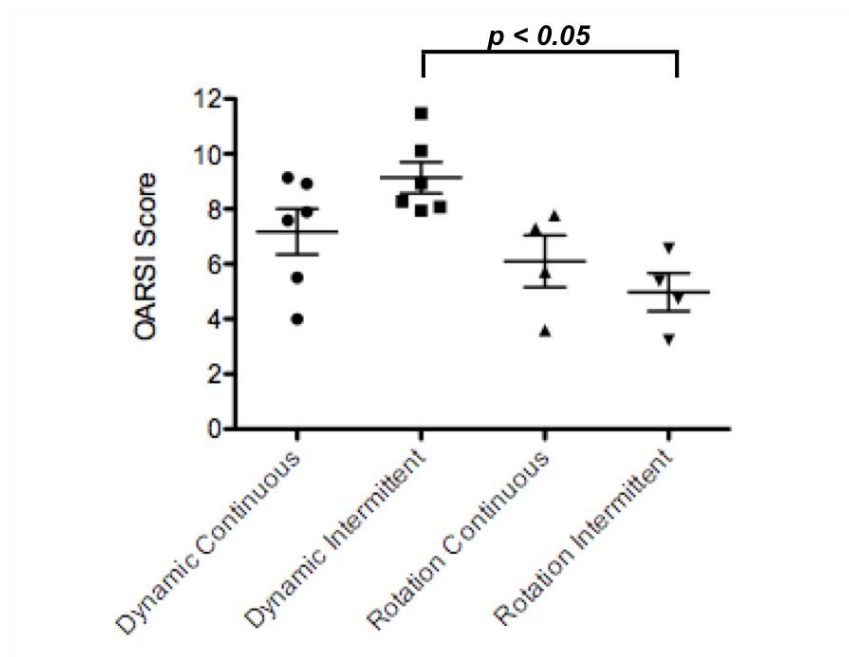
Figure 81: Activity Cycle Investigation Results – Dot plots of tibial scores showing observations, mean score per condition and standard error of the mean as error bars; a Kruskal-Wallis test indicates that there is a significant difference of means between all four groups ($p = 0.0108$) and a Dunn's test reveals that there is a significant difference between the Dynamic and Rotation Intermittent groups ($p<0.05$).

A Kruskal-Wallis test for non-parametric data shows a significant difference in means with $p = 0.0108$ and a Dunn's nonparametric comparison post-hoc test reveals that the dynamic intermittent condition results in a significantly higher score that the rotational intermittent condition. Both the intermittent and continuous rotational conditions have no measurable differences in resulting OARSI score. An increase in OARSI score from the continuous to intermittent dynamic activity conditions is notable, but does not quite qualify for statistical significance.

4.5.8 Discussion

Similarly to the data gathered using the JM1 systems, it's been found that the tibial scores are likely offer greater validity for drawing meaningful conclusions from these results. See Figure 82 and Figure 83 for the relative distributions of femur and tibia section scores for samples from both the pilot and activity cycle studies respectively, reflecting what was seen in Figure 54 and Figure 55.
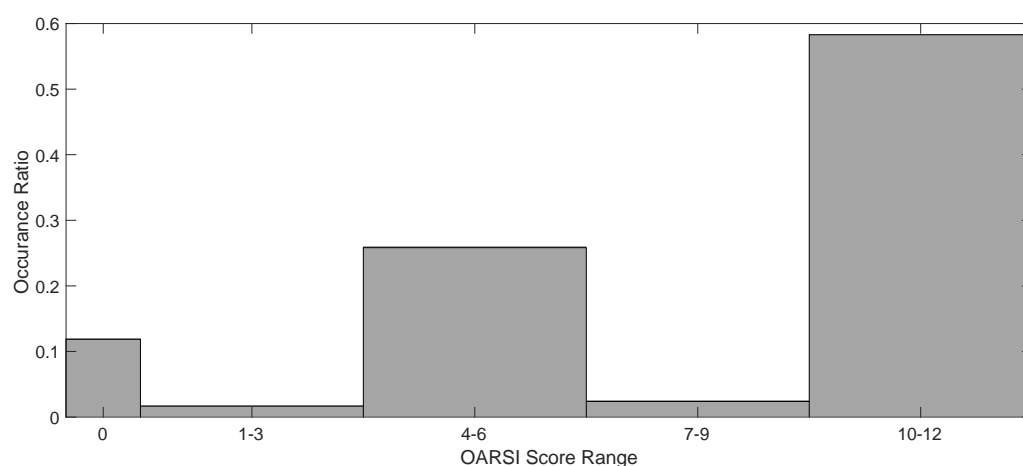
Figure 82: Distribution of Femur Scores from all JM2 Experiments– Femur scores tend to aggregate in categories associated with full depth staining loss (4-6, 10-12) making them unsuitable for drawing conclusive results.
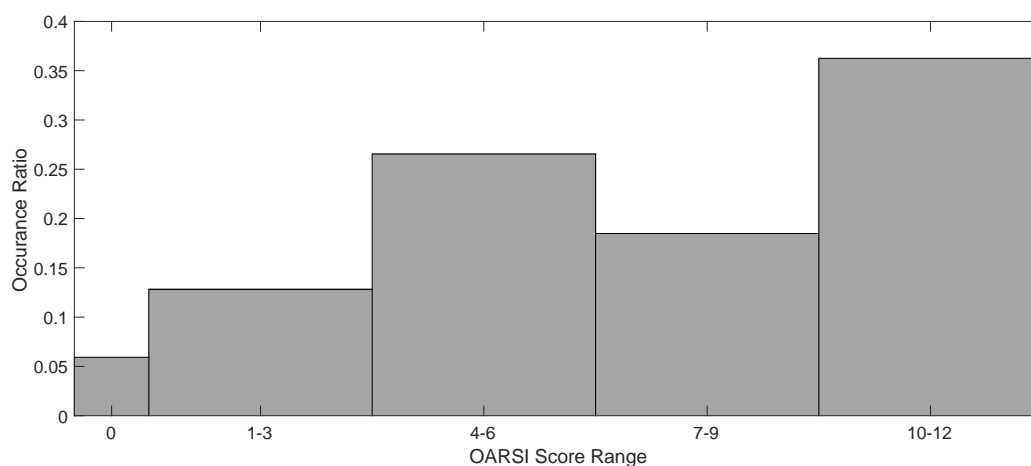
Figure 83: Distribution of Tibia Scores from all JM2 Experiments – Compared to femoral scores, the tibia scores display a more even distribution.

It is clear that the femur scores again tend to fall in categories associated with deeper loss (4-6 & 10-12). As stated in Section 3.4.6 this is due to the relatively thin articular surface of the femur. Therefore, all conclusions have been drawn from the mean tibial scores, and femoral scores were not presented as part of the results.

The results of the pilot study suggest samples taken from CD-1 mice have a greater sensitivity to the effects of active actuation. Figure 79 indicates that at both cycle rates, CD-1 mice exhibit a remarkably higher level of damage compared to $NF_{\kappa}B$/Balb C, reflected in the higher OARSI score. The increased sensitivity of excised joint from CD-1 mice indicates that the strain is a good model to use for investigating differences in actuation conditions, whereas $NF_{\kappa}B$/Balb C samples may not respond as measurably to the effects of the JM2.

The results of the pilot study also suggest that the dynamic actuation of the system does result in damage to articular surface as measured by the OARSI system. However, the levels of activity used in the pilot test (i.e. 0.25 Hz and 0.50 Hz at 8 hours/day) seem to have a saturating effect on the score. This is indicative that the even the lower activity level is too rigorous and any increase in cycle rate or culture time has no further measurable effects on joint health. However, compared to the samples cultured statically, there is a noticeable increase in scores of JM2 actuated samples, suggesting that a gradient of effects exists and that the static culture and dynamic culture 0.25 Hz for 8 hours/day represent two extreme ends.

In investigating activity cycles, the effects of dynamic actuation versus lack of actuation are clearly marked by the significant increase in tibial OARSI scores from the rotational to the dynamic condition for intermittent cycles. Again, this is an indicator that the action of the system has a destructive effect on the articular cartilage. Although not significant, there is a notable difference in score between the intermittent and continuous activity cycles as well. Despite both cycles resulting in the same amount of total activity, the continuous cycle scores lower than the intermittent cycle, and a higher sample number may result in statistical

significance. Further experimentation and repetition of these results would be necessary to confirm the effect, but one can speculate that the effect may be due to the relative differences in "resting" times. The continuous cycle features 22 hours straight of inactivity, while the intermittent cycle features 11 hours at a time. It is possible that the longer period of inactivity produces a beneficial effect on joint health, akin to a healing effect.

An important feature of a successful *in-vitro* culture system for OA study is the ability to produce a wide range of conditions, in this case as quantified by the chosen scoring method. Effectively, the system should be able to have a gradient of effects depending on the flexion cycle frequency and activity profiles. Combining the results from both experiments for mean tibial scores from 7-day dynamically cultured CD-1 joint samples shows that such a range of damage can be inflicted, Figure 84.
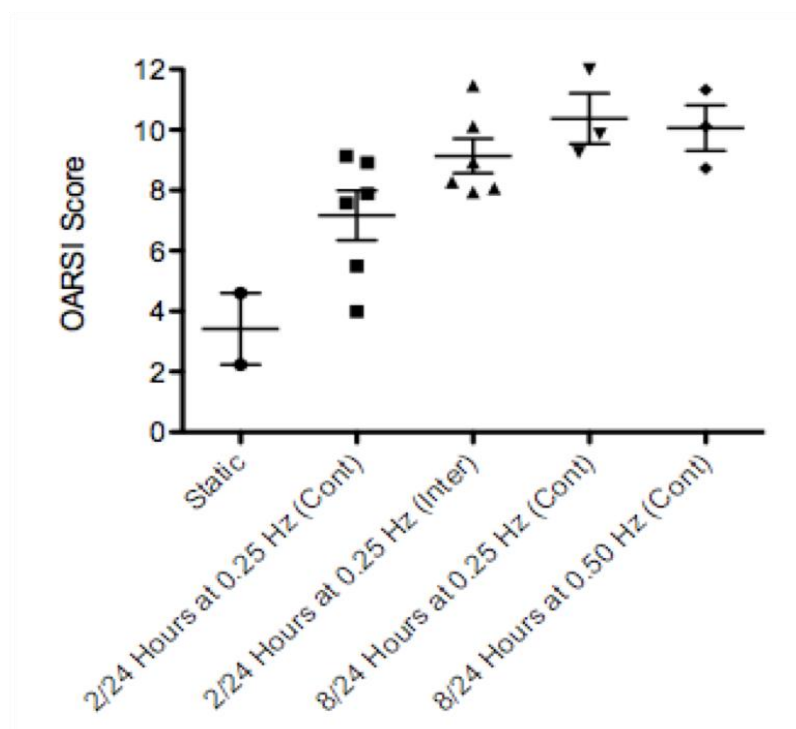
Figure 84: The Spectrum of Attainable OARSI Scores – A combination of all mean tibial scores for 7-day dynamic culture of CD-1 mice, showing that the JM2 system is capable to developing a range of damage by only changing parameters of the flexion-extension cycle. Static condition result shown for reference.

All dynamic cultures presented in Figure 84 score higher than the static culture due to a higher degree of staining loss of the tibial articular surface. Within the dynamic cultures, the cultures only actuated for 2 hours score lower than those actuated at 8 hours. This is an intuitive result considering that the joint goes through fewer flexion extension cycles. Within the 8-hour dynamic cultures, the effects of cycle rate are not measurable.

There is still a challenge in determining significance of several results. The nature of the experiments results in a low sample number per culture condition, leading to generally wide standard deviations of mean scores. Low sample numbers are due to a combination of factors including availability of mice, ethical concerns, space limitations for cultures in the incubator, and long data processing times. As the standard deviations between static, rotational and JM2 cultured conditions are generally comparable, there is no evidence that significant error is due to repeatability issues in the system design. Two ways to overcome this limitation are possible. First, increasing the number of samples per condition at the expense of researchers' time and cost would potentially bring to light some statistical significance. Second, developing a new evaluation system less prone to deviation. This however would require a notable amount of vetting and validation before being accepted by the greater research community.

In summary, the following conclusions are drawn from the results:

1. Confirmation of the conclusion drawn in 3.4.6 that the scores of femoral surfaces tend to fall into categories associated with >1/2 depth loss due to the thin articular surface.

2. Joints taken from CD-1 mice score significantly higher than those taken from $NF_{\kappa}B$/Balb C mice when dynamically cultured.

3. Dynamic actuation at any of the tested levels results in a higher score compared to static and rotational cultures, but significantly in limited comparisons.

4. Eight hours of dynamic culture results in a high enough amount of degradation of the articular cartilage matrix that cycle rate above 0.25 Hz has no measurable effect on Safranin-O staining loss.

5. There is potential that the duration of resting periods following dynamic actuation has an effect of joint health even in the total activity time is kept consistent. However, further investigation is needed.

4.6 Conclusions

The motivation of developing a reliable *in-vitro* OA investigation system fueled the design process of the JM2 system. The system was built on the successful design principles of the JM1 and improved to demonstrate a higher level of reliability, repeatability and usability. Particular focuses of the design included careful modeling of the linkage geometry to control the flexion angle with high precision and fabrication of a custom mounting system designed to minimize user error and burden during system set-up. A PI control system with repetitive feed forward contribution was developed and implemented to control the flexion cycle profile. Extensive modeling and analysis was also performed to characterize the system and determine the loading at the stifle joint interface.

The experiments reported here are intended to demonstrate that the system can develop a wide range of damage depending cycle conditions. The conditions tested clearly represent the more rigorous side of the JM2's actuation abilities, but still show that gradient of effects. The low sample numbers make determination of significance challenging and point to the need for developing alternative evaluation and statistical approaches. Furthermore, the cycle profiles tested only represent a minority of those possible even under passing loading. Future work may be directed at utilizing the different flexion range configurations, cycle rates, and activity

profiles. The vast potential for combinations of these three shows the equally vast range of conditions that the system can simulate.

The usage of the system reported in this Chapter did not use the active loading abilities of the system for the sake of simplicity. The extensive development and testing of active loading capability is the subject of Chapter 5.

5

Demonstration of Active Loading Control

5.1 Introduction

The results and discussions presented in Chapter 4 outlined the JM2 system as a system capable of culturing and actuating amputated mouse stifle joints in a controlled manner. The focus was on developing a system that paid high regard to maintaining a well-defined flexion angle profile. Although the joint experiences some loading in this configuration, it is passive in nature and results due to inertial forces and weights in the system. In an interest to further extend the capabilities of the JM2, a second actuator and linkage system was designed and fabricated with the potential to apply controlled loads on the joint during the motion cycle. This application of loads is termed "active loading control". This chapter covers the approach and solution to the non-trivial problem of active loading control using the JM2. The use of active loading control was not applied in biological experiments, and the goal of this work is to simply characterize and demonstrate the abilities of the JM2 as a system to apply controlled loads. Testing of the system's capabilities was performed using an "analogue stifle joint".

This chapter covers topics pertaining to:

1. Revision of the loading linkage system and the concept of active loading.

2. Outlining the controller design to achieve active loading control, and the sensing approaches.

3. Presentation of evidence that rejects the use of current sensing as a reliable method of controlling loads.

4. Development of a feedback control system using direct load sensing.

5. Presentation of the abilities and limitations of the developed active loading system.

5.2 Revision of Loading Linkage System

Although covered briefly in Section 4.2, we will begin by reviewing the JM2 design, with special attention paid to the loading linkage system. A conceptual figure of the JM2 is repeated in Figure 85 here for convenience.
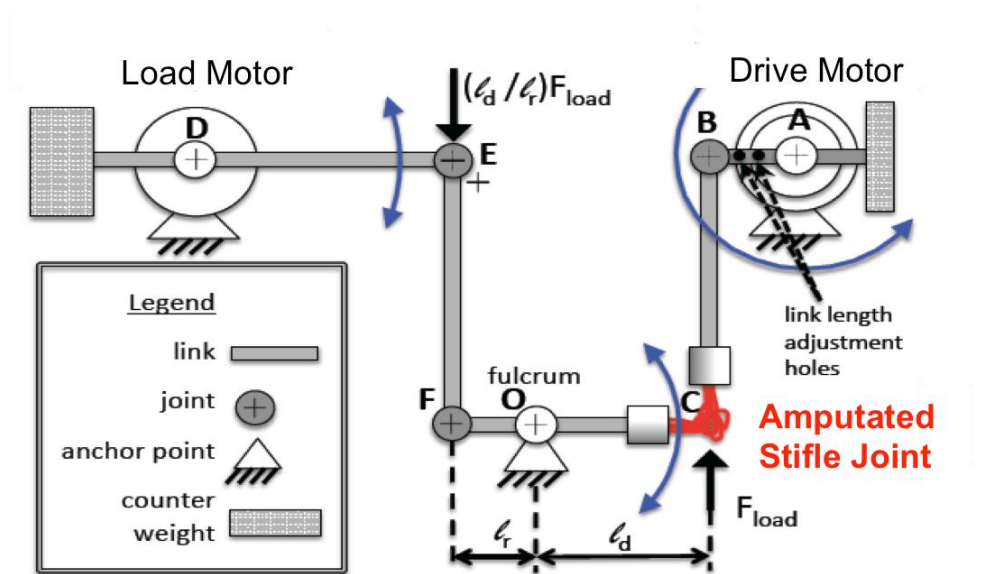
Figure 85: Conceptual Schematic of JM2 Design – Repeated for convenience.

Recall that the linkage system ABCO, actuated by the flexion/extension drive motor, controls flexion profile of the stifle joint and must satisfy geometric constraints. The loading linkage system, DEFO, is used to apply a controlled load at the stifle joint. In the configuration shown conceptually in Figure 85, a desired force at the joint is marked F_{Load}. Assuming the system is static and neglecting any linkage weight effects, one can see that F_{Load}, would be the result of the application of a torque at D resulting in a load $(l_d/l_r)F_{load}$. Although this is a dramatically simplified model, it demonstrates the basic principle behind using the loading motor for active loading control.

In the fabricated configuration, the two linkage systems are offset in the direction perpendicular to the plane of motion. This reduces the overall system footprint and both linkage systems can go through their full range of motion without interference. An early prototype is shown in Figure 86.
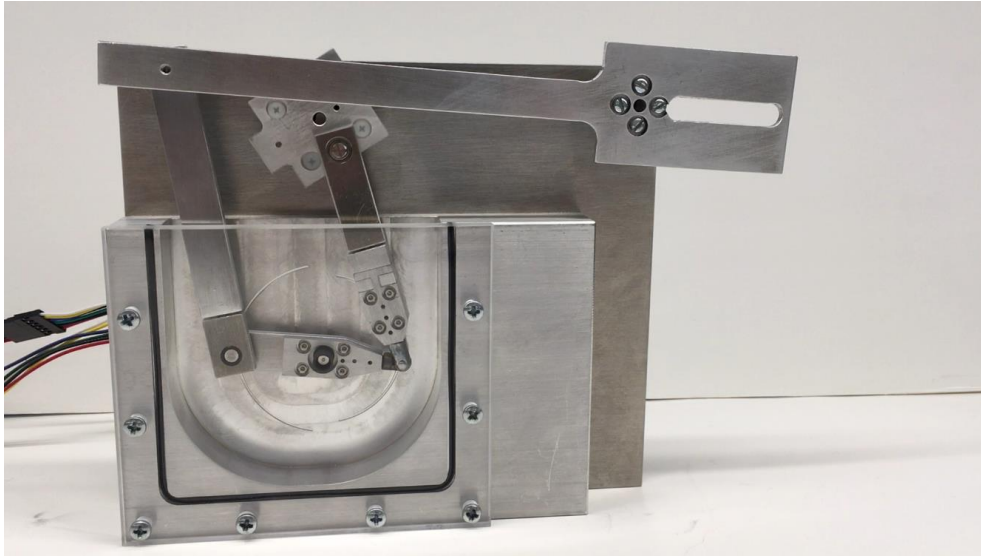
Figure 86: Early Prototype of JM2 - Shows complete device with prototype loading linkage system

Like most of the system components, the links in the loading linkage system are custom fabricated out of 6061 aluminum sheets. Recall that a DC gear motor with a ~34:1 gear ratio is used as the loading motor. Further revisions were made to the system, particularly pertaining to link DE, attached to the loading motor, in order to accommodate a load cell for feedback control purposes. These will be discussed further in Section 5.5.

5.3 Controller Layout

Successful implementation of active loading is dependent on the development of an effective closed loop control system. The goal of the control system is to determine the duty cycle of a pulse width modulated (PWM) voltage signal input into the loading motor for some desired load profile at the stifle joint. The profile is assumed to be a function of cycle position as opposed time. Nominally, the flexion cycle profile is a function of time, and with perfect flexion cycle control the loading profile may also be designed as a temporal function. However, any error in the flexion cycle profile tracking would then result in an offset between

the flexion profile and loading profile. A general loading control scheme is shown in Figure 87.
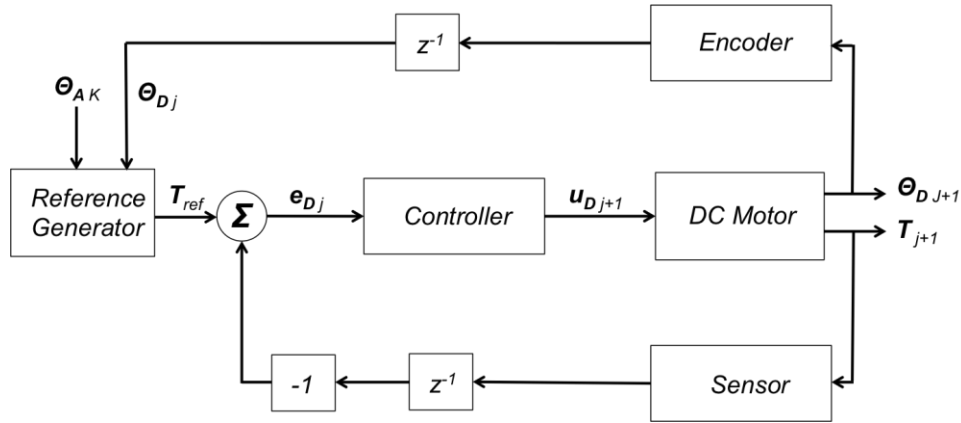
Figure 87: Active Loading Controller Block Diagram – The nature of the controller is dependent on the type of sensing method used to estimate applied motor torque.

T_{ref} is the control reference, determined from the desired load at the current cycle position. Since the load is a function of position the reference value is generated for each loop iteration, j. The absolute cycle position is calculated by the "Reference Generator", which must consider the relative positions of both motors in order to calculate an absolute cycle position. As such encoder feedback from the loading motor and a position value from the drive motor controller is fed into the Reference Generator every iteration. T_{ref} is then calculated as a function of the absolute cycle position. A second sensor is used to sense a measure of the applied load. The sensor type employed determines the nature of reference value. An error value, e_{Dj}, is calculated by the difference between the reference value and sensor feedback value. A controller, whose nature is also determined by the sensor type, generates an input signal to the DC motor, $u_{D,j+1}$, which takes the form of PWM voltage signal. This control scheme is executed using an Arduino Mega microcontroller at a 100 Hz sample rate.

5.3.1 Calculating Absolute Cycle Position

The loading profile must be designed as a function of the joint flexion angle. This guarantees that the loading cycle and motion cycle remain synchronized. As a consequence the reference signal must also be a function of the joint flexion angle, or some absolute cycle position. However, the encoders employed only provide enough information individually to determine a position in the cycle relative to the starting position. Therefore, there is no information about the actual geometric state of the linkage system, or absolute flexion angle available unless the initial conditions of the system are known.

An algorithm was developed to address this issue, utilizing the fact that the encoder value of the loading motor oscillates between two values as the cycle progresses. Unlike drive motor, whose encoder count continues to rise due to constant rotation, the loading motor only moves between two fixed angles. Therefore, the system can auto-calibrate itself by looking for features in the loading motor profile and effectively calculate the initial offset of the system relative to some known absolute position.

Recall from Section 4.3 that the drive motor control algorithm keeps track of the total number of drive motor encoder counts and generates a discrete angular position value of the drive motor shaft, θ_A^*. This value is scaled from 0-254 due to memory limitations and is relative to the initial position of the drive motor shaft when the system is initialized. Therefore, there exists an offset value $\theta_{A,Offset}^*$ such that:

$$\theta_A^* - \theta_{A,offset}^* = \theta_{A,abs}^*$$

Where $\theta_{A,abs}^*$ is an absolute discrete cycle position with a value of 0 corresponding to link AB being horizontal, or $\theta_A = 0^o$ according to the definition specified in Section 4.4.2. The angle definitions are repeated in Figure 88 for convenience.
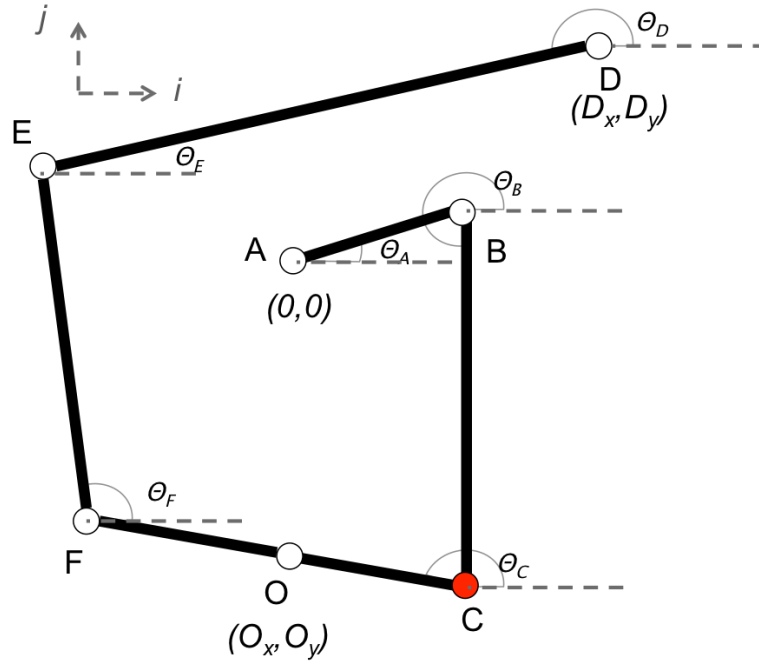
Figure 88: JM2 Kinematic Definitions – Repeated for convenience

Using the solution for θ_D in Equation (4.17) derived in Section 4.4.2, it's possible to express θ_D as a function of θ_A, Figure 89. The mean value of θ_D is also shown.
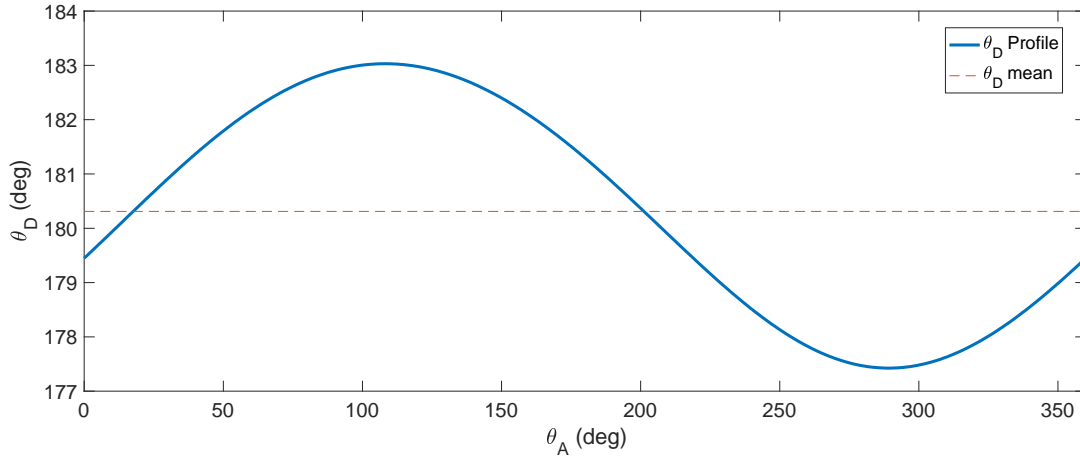
Figure 89: Profile and Mean Value of Angle θ_D as a Function of Drive Motor Angle – Note that the value of θ_D crosses it's profile mean value at two distinct values of the drive motor angle.

One can see that the value of θ_D crosses its mean value, $\bar{\theta}_D$, at two points in the profile with different slope directions. Hence it is possible to correct for any offsets in angular profile measurements for both θ_A and θ_D by measuring the profile of θ_D as a function of some $(\theta_A + \theta_{A,offset})$ and looking for one of the mean crossing points in the θ_D profile.

This is best illustrated by an example. The following is a demonstration of calculating a discrete offset, $\theta_{A,offset}^*$. The system controller receives encoder feedback from both the drive motor and loading motor and converts them to values scaled from 0 to 254 that repeat every cycle by considering the number of encoder counts per output shaft cycle. The recording of both profiles occurs in synchronization and the cyclic nature of the system means that they repeat in unison. Note that these original estimations are offset from the true zero position of the system.

$$\theta_A^* + \theta_{A,offset}^* = \left[\frac{drive\ motor\ encoder\ count}{counts\ per\ revolution} - floor\left(\frac{drive\ motor\ encoder\ count}{counts\ per\ revolution} \right) \right] * 254 \quad (5.1)$$

$$\theta_D^* + \theta_{D,offset}^* = \left[\frac{load\ motor\ encoder\ count}{counts\ per\ revolution}\right] * 254 \tag{5.2}$$

The *floor* function in Equation (5.1) simply maps the argument down to the previous integer value, in this case necessary to account for cycle ambiguity in the drive motor position. Considering that the system starts from an offset position, the profile of $(\theta_D^* + \theta_{D,offset}^*)$ versus $(\theta_A^* + \theta_{A,offset}^*)$ is shown in Figure 90, with the mean value of $(\theta_D^* + \theta_{D,offset}^*)$ shown as well.
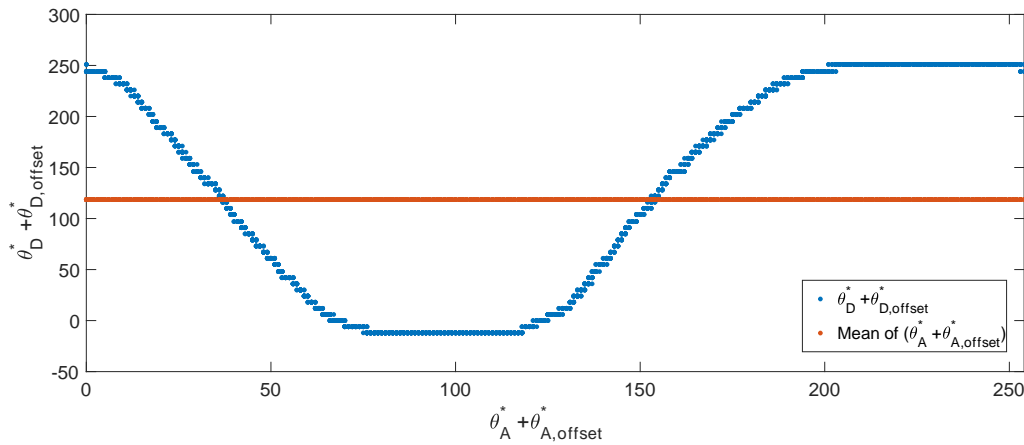
Figure 90: Profile of Load Motor Angle as Measured – Due to the fact that the motor encoders are relative, the system measures both the load motor and drive motor shaft angles with some offset relative to an absolute zero value.

Graphically, the offset is clear. One can compare the profiles in Figure 89 and Figure 90 and see that the offset can be corrected by comparing a similar feature such as the mean crossing. In the developed algorithm, the point at which the drive motor profile intercepts the mean value with a positive slope is used. From Figure 89, this intercept occurs at $\theta_A=18°$,

which corresponds to a scaled discretized value of $\theta_A^* = 13$. In Figure 90 this intercept occurs at a value $(\theta_A^* + \theta_{A,offset}^*) = 154$. Now $\theta_{A,offset}^*$ can be calculated for this case as:

$$\theta_{A,offset}^* = 154 - 13 = 141$$

And the absolute drive motor position can be calculated as:

$$\theta_A^* = ((\theta_A^* + \theta_{A,offset}^*) - 141) \bmod 254$$

The corrected profile of $(\theta_D^* + \theta_{D,offset}^*)$ versus θ_A^* can be plotted as shown in Figure 91.
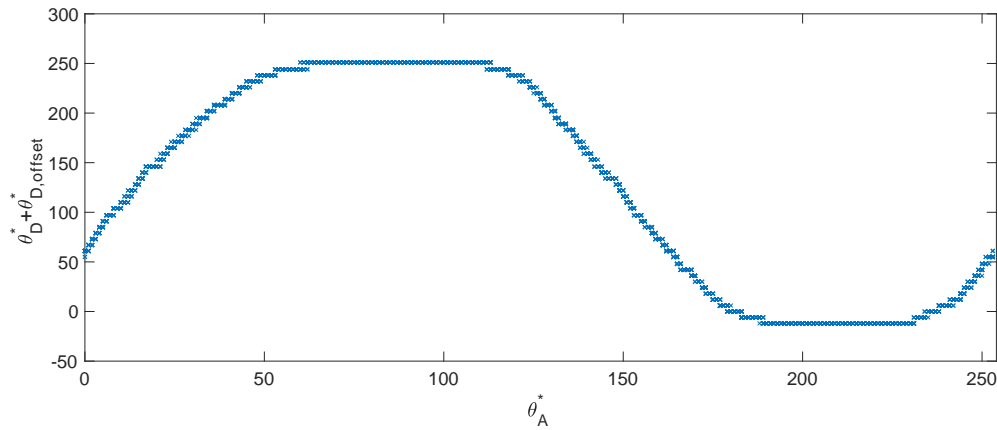
Figure 91: Corrected Load Motor Angle Profile – By running the offset calculation algorithm, the offset in the drive motor angle can be eliminated and the drive motor angle can be expressed relative to a known zero value.

Although there is still an offset associated with the load motor angle, it is not necessary to eliminate for proper functionality of the system. This algorithm is summarized in Figure 92.
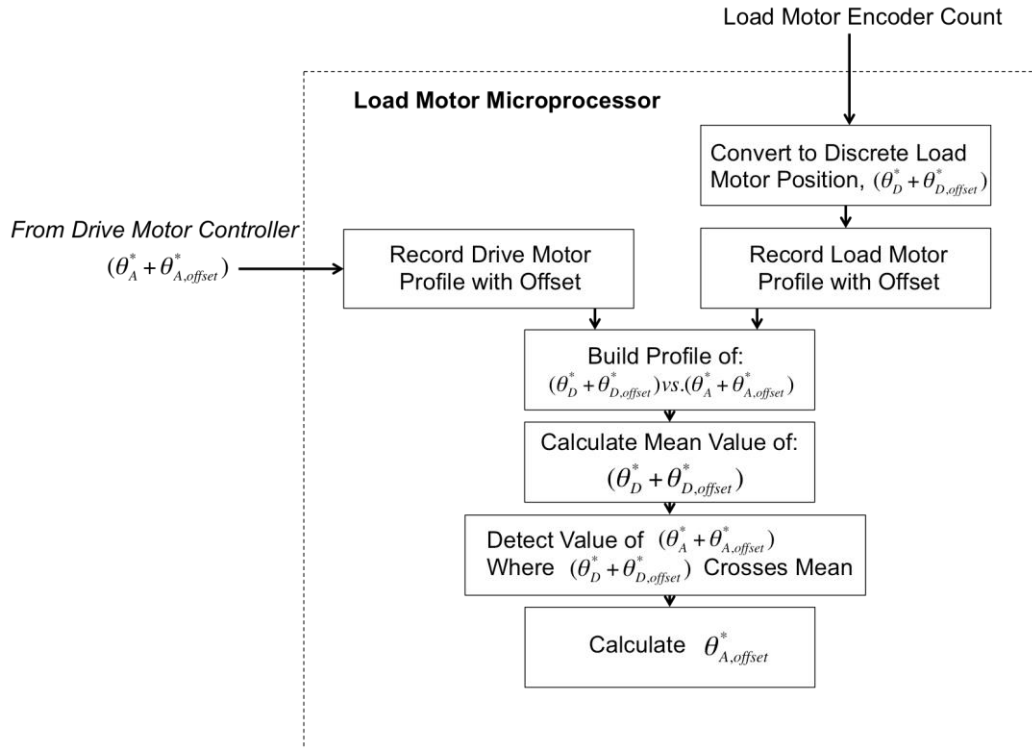
Figure 92: Drive Motor Offset Calculation Algorithm

The algorithm only needs to be run over a single cycle to accurately calculate the offset. Therefore, it is run once when the system is initiated. The absolute position value, θ_A^*, can now be used by the Reference Generator to calculate a reference value that is a function of the absolute cycle position. In order to maintain accuracy as the system operates, this algorithm is repeated every 100 cycles and a new value for the drive motor offset, $\theta_{A,offset}^*$, is calculated in case any loss of synchronization occurs.

5.3.2 Sensing Options

A major challenge in implementing active loading control is developing an efficient sensing method. With the goal of trying to directly control some dimension of the load at the stifle joint, it would be ideal to directly sense the load being controlled. However, no feasible sensing method was conceived of to achieve this, due to the limitation that the joint is constantly submerged in fluid. Therefore, indirect sensing methods, where mathematical models between the sensed parameter and the joint load could be developed, were researched. Efforts were directed at two approaches: current sensing of the loading motor current draw, which ultimately proved unsuccessful, and bending load sensing of link DE, which demonstrated promising results.

5.4 Attempts at Current Sensing

The approach to current sensing was based on the theoretical premise that a DC motor's current draw is directly proportional to the output torque. In other words, measuring the current draw of the loading motor would allow for an estimate of the applied torque at joint D, which could then be related to an applied load at the stifle joint. The advantage of current sensing over direct load sensing on the linkage system is that it does not require additional sensors to be mounted onto the device itself. Therefore, there are no reservations associated with failure of sensors in the incubator during use. Although current sensing is theoretically possible, the discussion presented here highlights the challenges in implementation that ultimately lead to the infeasibility its use for this particular application.

5.4.1 Current-Torque Relationship in DC Motors

It is necessary to delve a little deeper into the relationship between current draw and output torque in DC motors. In a theoretically ideal case, the relationship between the two is one of direct proportionality, such that:

$$T_{motor} = K_T i \tag{5.3}$$

Where T_{motor} is the torque applied by the motor shaft, K_T is the so-called motor size constant and i is the current drawn by the motor. K_T is equivalent in value to K_V, called the back-electromotive force (EMF) constant or motor velocity constant, in a system of consistent units. K_V, and consequently, K_T, can be easily found by back driving a motor shaft and measuring the resulting back-EMF:

$$K_T = K_V = \frac{\omega}{V_{emf}} \tag{5.4}$$

Where ω is the velocity at which the motor is back-driven, and V_{emf} is the measured back-EMF voltage. It is clear that the theoretical relationship is straightforward to model once the value of K_T is determined, which can be accomplished with a relatively easy experimental set-up.

For successful implementation, the losses due to friction must be considered. Particularly in geared motors, these losses are significant. Equation (5.3) can be appended to account for frictional losses:

$$T_{motor} = K_T i - T_f(\omega) \tag{5.5}$$

Where $T_f(\omega)$ is the rotational friction loss between the internal shaft and output shaft, generally expressred as a function of the output angular velocity.

5.4.2 Motor Properties and Friction Characterization

The characterization of the frictional properties of the chosen motors is necessary to accurately estimate the output torque. In order to develop a model for $T_f(\omega)$ an experimental procedure was developed where the current draw of a motor was measured while it was run at a constant angular velocity with no load. With neither loading nor angular acceleration, the output torque has effectively been set to zero:

$$T_{motor} = 0$$

In this special case, Equation (5.5) can be re-written as:

$$i = \frac{T_f(\omega)}{K_T} \tag{5.6}$$

Therefore, since K_T, is a constant, one can derive a scaled relationship between the motor friction and angular velocity by measuring current draw as a function of angular velocity.

Data was collected for three DC motors of the same model, identical to those intended to act as the loading motor. The motors were run at a constant velocity using the same speed controller described in Section 4.3. The current draw was measured using an ACS712 Low Current Sensor (Sparkfun, Niwot, CO, USA) and sampled using the same Arduino UNO microcontroller running the control scheme at 100 Hz. The resulting current versus speed profiles are plotted in Figure 93 for all three motors.
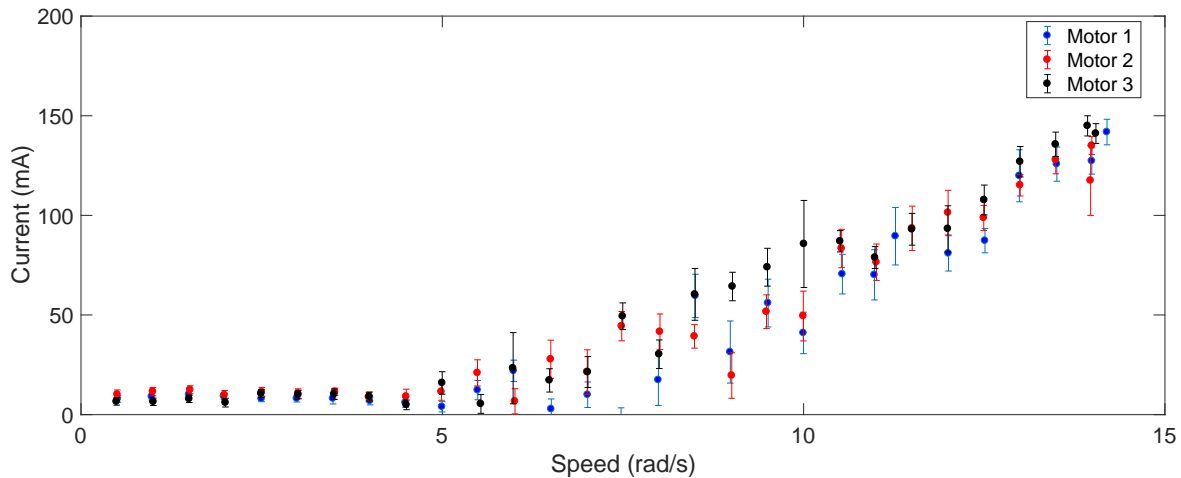
Figure 93: Current Draw Versus Speed Measurements for Three 34:1 DC Motors - Error bars represent +/- 1 standard deviation in current measurements. The current draw is a measure of the motor friction and the discrepancies between the measurements for three motors suggests that they have different frictional properties.

Figure 93 represents the major barricade to successful implementation of load sensing. The three tested motors do not share identical current draw profiles as functions of speed. This is indicative that the torque characteristics of the three tested motors differ and that each has a unique torque to speed relationship, $T_f(\omega)$. This is statistically proved by a series of T-test

comparing pairs of current measurements at each speed, shown in Figure 94. All the comparisons result in a high confidence ($p << 0.01$) that the measured current values differ.
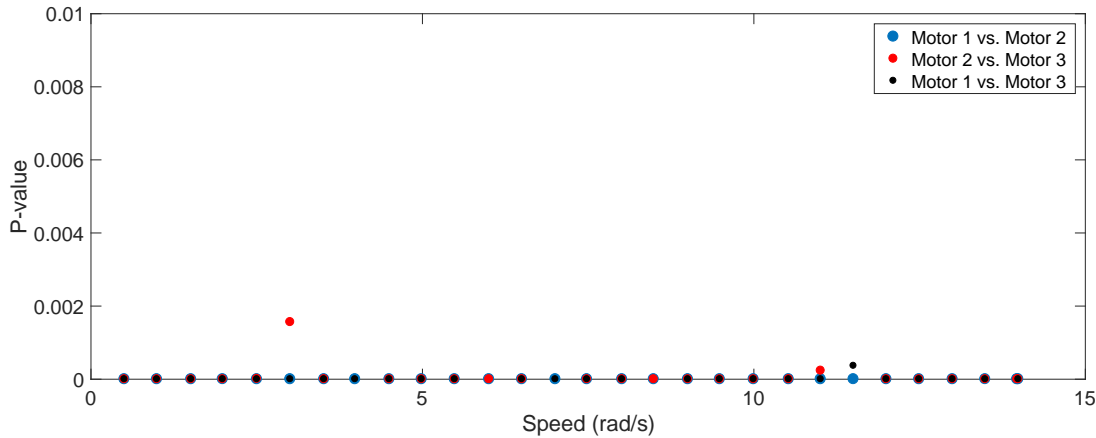
Figure 94: Statistical Comparison of Current Measurements per Speed for 34:1 DC Motors – Statistically, the three motors are not identical in frictional properties.

Although it is possible to characterize each motor individually, it presents an additional burden in that each individual device's control system needs to calibrated and tuned separately. Furthermore, one can expect that over the lifetime of a single motor, the frictional properties would evolve as components degrade and fatigue. As a result, efforts to utilize current sensing for load estimation were abandoned in favor of a direct load sensing approach.

5.5 Direct Load Sensing

The approach of direct load sensing involves the placement of a bending micro load cell on link DE. A load cell on the link effectively measures the bending strain at the sensor location, which in turn provides a measure of the applied loading motor torque. The applied

torque can then be directly related to a component of the stifle joint load through system modeling. Figure 95 shows a prototype JM2 device fitted with a load cell on link DE.
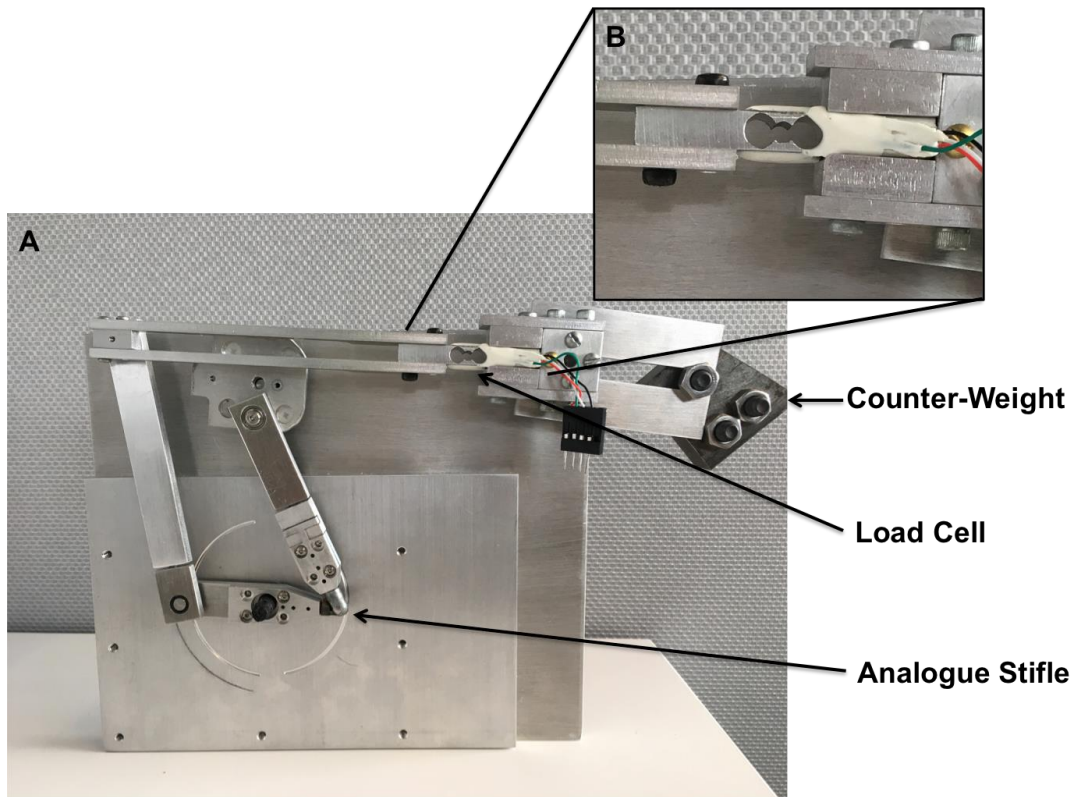
Figure 95: Prototype JM2 System Fitted with Active Loading Capabilities - A) Full device; B) Load cell detail.

Link DE was fully redesigned to properly interface the load cell with the system. Figure 95B shows the sensor used, a micro load cell (CZL616C, Phidgets, Alberta, Canada) designed to measure shear load in the vertical plane, perpendicular to the face seen in Figure 95B. The sensor is prefabricated with appropriately mounted strain gauges and a reported bidirectional load capacity of 0.780 kg. The sensor signal is amplified using an Arduino compatible amplifier and signal conditioning board, or shield (RB-Onl-38. RobotShop, Vermont, USA).

The amplified signal is sampled by Arduino Mega microcontroller with a 10-bit analog-to-digital (A/D) resolution at a 100 Hz sample rate. A counterweight is hung in a manner to preload the motor, with the purpose of ensuring constant contact between gear teeth and preventing backlash during operation. The analogue stifle joint is also shown, fabricated out of a modified hinged threaded standoff (98010A260, McMaster-Carr, NJ, USA).

5.5.1 Load Cell Calibration

The load cell was experimentally calibrated to relate the microcontroller sampled A/D value to a torque at joint D. The calibration procedure involved maintaining the link fixed horizontally about joint D and hanging weights on known mass on joint E. The free body diagram in Figure 96 summarizes the procedure. No counterweight was used.

Figure 96: Free Body Diagram of Load Cell Calibration Procedure – By fixing the link at D and applying a weight at E, the load cell is calibrated for a known reaction moment M_R

Here W_A is an applied weight at joint E and M_R is the resulting reaction moment when the link is prevented from rotating. From static analysis the relationship between M_R and W_A can be expressed as:

$$M_R = -WL_{ED} \qquad\qquad (5.7)$$

The calibration indirectly takes into account the effects of link weigh with an offset. Furthermore, recall from Figure 89 that link ED only rotates within +/- 3° from the horizontal throughout the cycle. Therefore, rotational effects resulting in the change in direction of the weight are neglected. Table 14 summarizes the masses placed at E, resulting reaction moments at D and recorded A/D values obtained during calibration. The relationship between torque at D and the A/D value is shown in Figure 97.

Table 14: Summary of load cell calibration data

Mass (kg)	Load Cell Output (+/-3)	Resulting Moment (Nm)
0	503	0
0.01	512	-0.014
0.02	525	-0.029
0.03	535	-0.043
0.05	558	-0.072
0.1	606	-0.143
0.3	809	-0.430
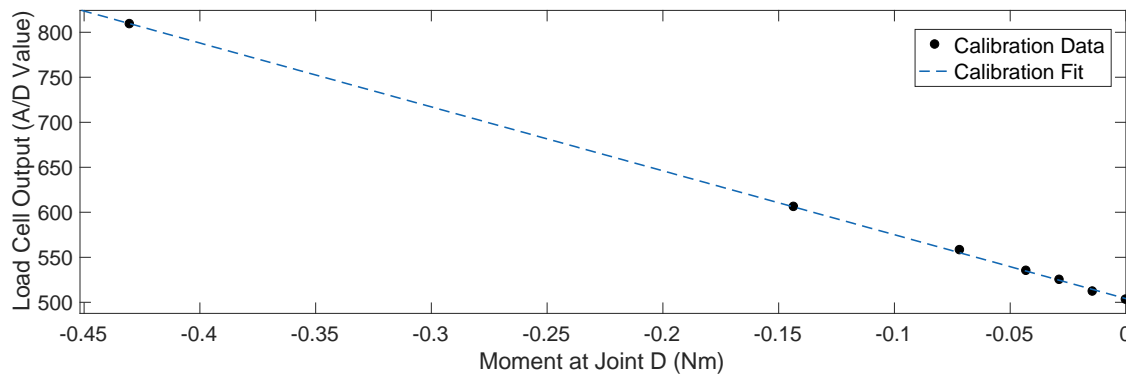
Figure 97: Load Cell Calibration Data and Fit

The derived calibration curve is linear, with a regression coefficient $R^2 = 0.9998$:

$$O_{LC} = -709.8M_R + 504.9$$

Or in terms of an applied torque at D, T_D:

$$O_{LC} = -709.8T_D + 504.9 \tag{5.8}$$

Where O_{LC} is the raw recorded A/D value from the load cell. This calibration allows one to relate the sensor measurement to a moment at joint D, which is the result of an applied motor torque. Effectively, Equation (5.8) allows for the estimation of the applied torque at D. However, in order to accurately control the load on the joint, it is necessary to develop an additional relationship between the applied torque at D and some component of the load.

5.5.2 Load Modeling and Friction Effects

Although the full dynamic model derived in Section 4.4, culminating in the system of equations summarized by Equation (4.34) can be used to derive a relationship between the applied motor torque and the resulting internal loads at the joint, the entire system of equations must be solved in order to do so. In application, this presents a computationally demanding process of the control system. Therefore, it is preferable to develop a closed-form relationship between the applied torque and some component of the stifle load. Consider the loading linkage system as shown in Figure 98.
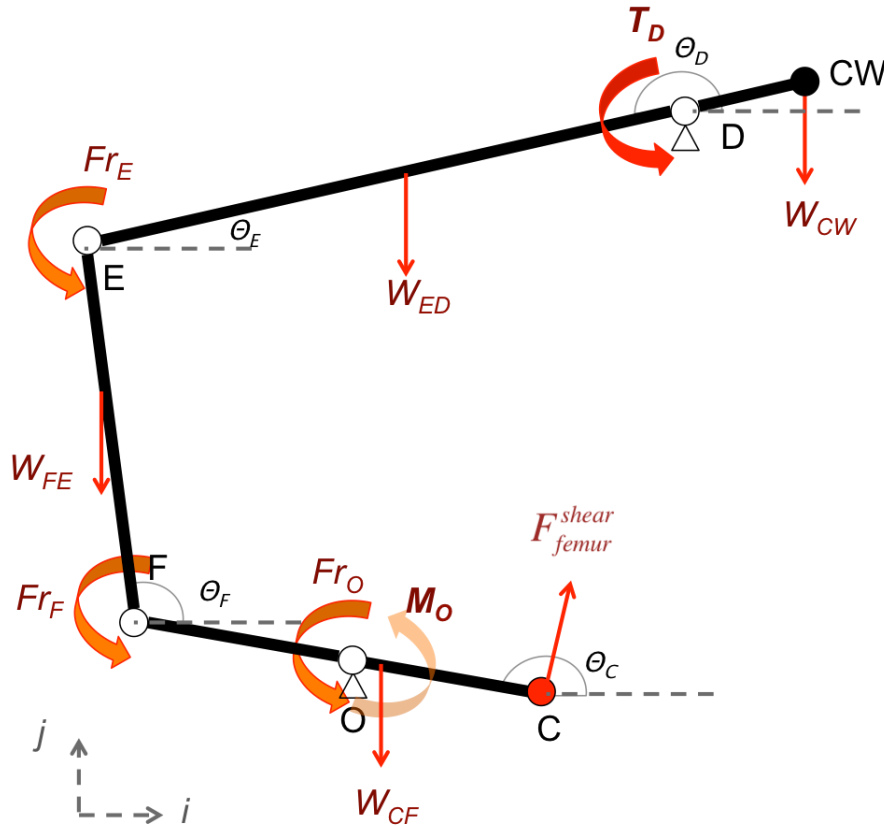
Figure 98: Free Body Diagram of Loading Linkage System – By accounting for applied motor torque, linkage weights and joint friction, it is possible to develop a relationship between the applied motor torque and an equivalent femoral shear force.

This derivation process takes into account all link weights, W_{ED}, W_{FE}, and W_{CF} as well as the counterweight, W_{CW}, at point CW. Link weights act at their respective centers of mass, assumed to be halfway along the total link length. Rotational friction at joints E, F and O are modeled as constant values and shown as Fr_E, Fr_F and Fr_o respectively. The applied motor torque, T_D, is shown at joint D and follows a right-handed sign convention.

The system is assumed to be quasi-static. First, we can relate the applied torque to a reaction moment at joint O, M_O, by considering an energy balance formulation. The kinetic energy of the system is considered negligible due to the relatively low cycle rates and link velocities:

$$Energy\ in = Energy\ out$$

$$T_D \Delta\theta_D = -M_O \Delta\theta_C + (\Delta\overrightarrow{CG}_{ED} \cdot \hat{j})W_{ED} + (\Delta\overrightarrow{CG}_{FE} \cdot \hat{j})W_{FE} + (\Delta\overrightarrow{CG}_{CF} \cdot \hat{j})W_{DF} + \Delta(L_{DCW}\sin(\theta_E))W_{CW}$$
$$+ Fr_E|\Delta\theta_E - \Delta\theta_F| + Fr_F|\Delta\theta_F - \Delta\theta_C| + Fr_O|\Delta\theta_O|$$

This can be written more succinctly by grouping the terms associated with potential energy and energy loss due to friction:

$$T_D = -M_O \frac{\Delta\theta_C}{\Delta\theta_D} + PE_{comp} + FR_{comp} \tag{5.9}$$

$$where:$$

$$PE_{comp} \stackrel{\text{def}}{=} \frac{(\Delta\overrightarrow{CG}_{ED} \cdot \hat{j})W_{ED} + (\Delta\overrightarrow{CG}_{FE} \cdot \hat{j})W_{FE} + (\Delta\overrightarrow{CG}_{CF} \cdot \hat{j})W_{DF} + \Delta(L_{DCW}\sin(\theta_E))W_{CW}}{\Delta\theta_D}$$

$$FR_{comp} \stackrel{\text{def}}{=} \frac{Fr_E|\Delta\theta_E - \Delta\theta_F| + Fr_F|\Delta\theta_F - \Delta\theta_C| + Fr_O|\Delta\theta_O|}{\Delta\theta_D}$$

With Equation (9) relating the applied torque to a reaction moment at joint O, it is necessary to relate this moment to a component of the stifle joint load. M_O can be expressed as an equivalent force acting perpendicular to link FC. In fact, since the femur is mounted as part of FC, the equivalent force is the shear force acting along the femoral surface, F_{femur}^{shear}, and can be expressed as:

$$F_{femur}^{shear} = \frac{M_o}{L_{CO}} \tag{5.10}$$

Combining Equations (5.9) and (5.10), and re-organizing leads to the following:

$$T_D = -F_{femur}^{shear} G(\theta_A) + PE_{comp}(\theta_A) + FR_{comp}(\theta_A) \tag{5.11}$$

$$where:$$

$$G(\theta_A) \overset{\text{def}}{=} L_{CO} \frac{\Delta\theta_C}{\Delta\theta_D}$$

The defined functions G, FR_{comp} and PE_{comp} are dependent on the linkage system geometry, and hence can be expressed as functions of the input angle θ_A. These functions also have physical meanings. G is analogous to a mechanical advantage, relating the resulting shear force at the femur due to an applied loading motor torque. FR_{comp} describes the loading ability lost due to overcoming friction in the mechanical joints. PE_{comp} describes loading ability lost due to changing the potential energy of the system.

It is helpful to define a convention related to the load direction. In Equation (5.11), the sign of F_{femur}^{shear} agrees with the convention defined earlier in Section 4.4.3, repeated here in

Figure 99B. *For the remainder of this dissertation, a positive value of F_{femur}^{shear} will be referred to as a compressive state of loading, while a negative value will be a tensile state.* Although it is unconventional to assign such terminology to a shear force, one can easily deduce from the system geometry that the defined compressive state is similar to physiological compression and the tensile state is similar to physiological tension, or stretching of the joint.
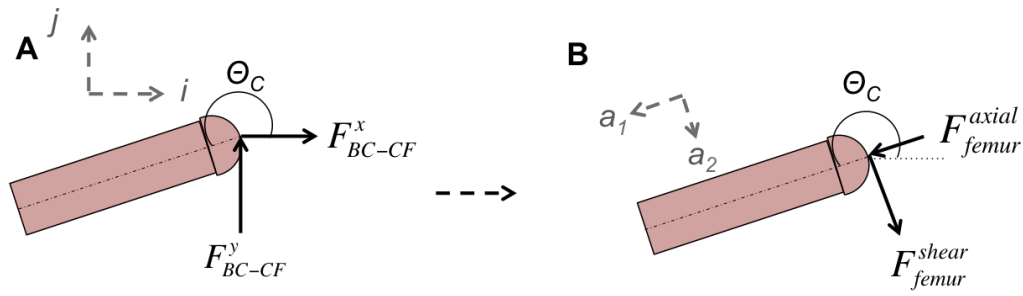
Figure 99: Femoral Load Sign Convention – A) Loads as expressed in the global coordinate system; B) Loads as expressed in the femoral coordinate system, showing arrows in the positive convention.

The derivation of Equation (5.11) relied on several assumptions that may be called into question (e.g. quasi-static system). It is useful to compare this model with the full dynamic model derived earlier in Section 4.4. Figure 100 shows the resulting femoral shear force as calculated by both models for comparison. The comparison is made for an constant applied torque of 0.3 Nm in a counterclockwise direction, for the system operating at a 0.25 Hz cycle rate, considered representative operating conditions. Since the dynamic model does not consider friction, this comparison is for a friction-free case. The two models show very strong agreement, justifying the assumptions made and validating the accuracy of Equation (5.12).
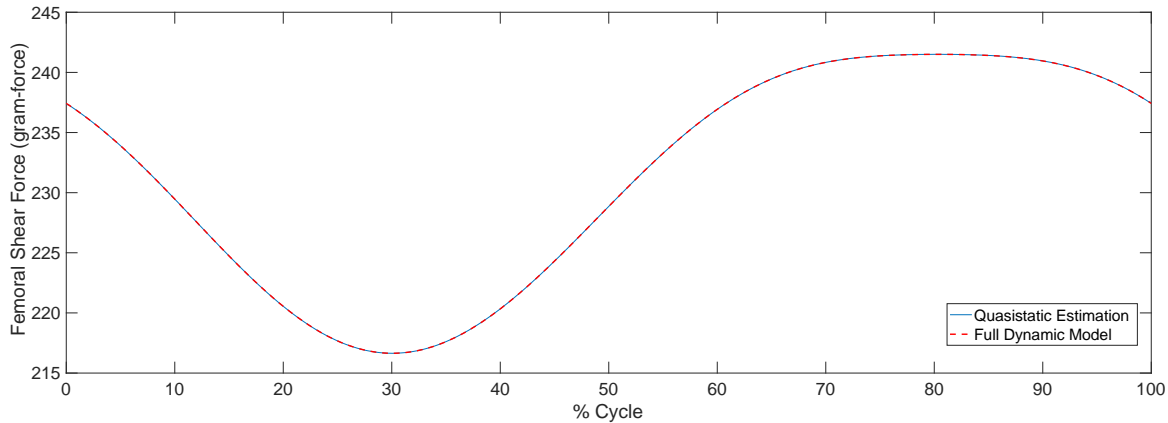
Figure 100: Comparison of Femoral Shear Force as Calculated by Quasi-Static Estimation and Full Dynamic Model – The agreement between the two models indicates that the relationship derived by quasi-static assumptions are sufficient to accurately predict the applied joint loads.

It is possible to use Equation (5.11) to determine the achievable femoral shear loads given the maximum torque capabilities of the loading motor. The motor used is reported to produce a maximum output torque of 0.35 Nm bi-directionally. This represents an ideal range but can still be used to calculate the range of achievable femoral shear forces under different conditions. Figure 101 shows the region of attainable femoral shear loads for a condition where no friction is considered and no counterweight is mounted. Figure 102 shows how that region shifts when a counterweight with mass 100 g is mounted at a distance of 3 cm from the motor shaft axis. Figure 103 shows how the region shape is skewed by the consideration of potential friction in the joints. The points at which the region changes non-continuously correspond with positions in the cycle where a joint rotation changes relative direction, resulting in a change in direction of that joint's frictional force.
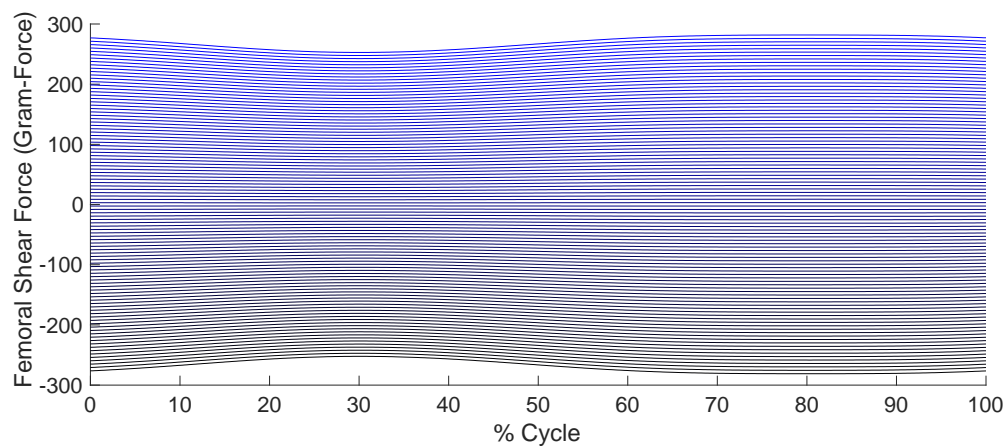
Figure 101: Region of Achievable Femoral Shear Loads with No Counterweight or Friction
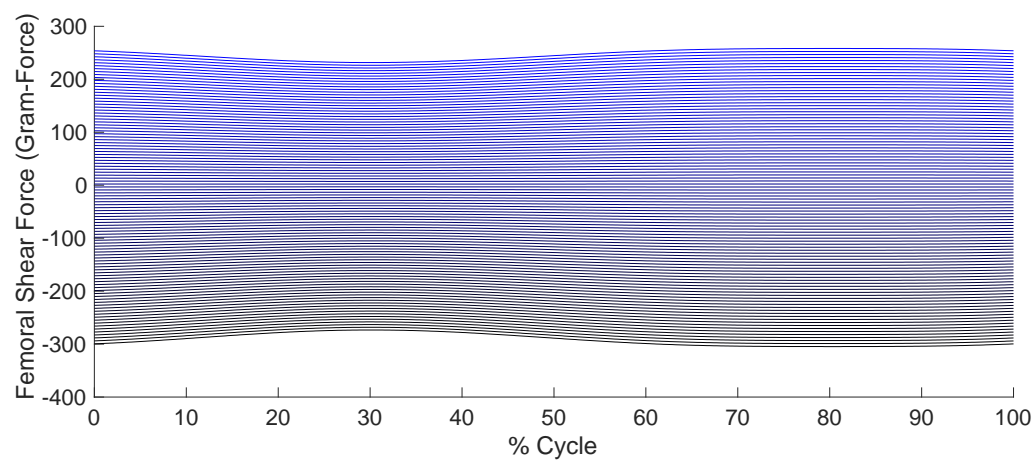
Figure 102: Region of Achievable Femoral Shear Loads with 100 g Counterweight Mounted 3 cm from Loading Motor Axis and No Friction
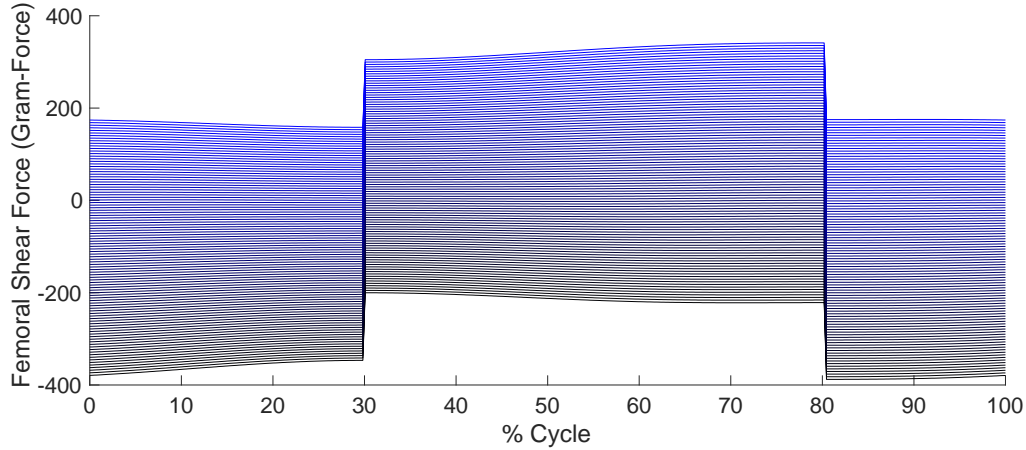
Figure 103: Region of Achievable Femoral Shear Loads with 100 g Counterweight Mounted 3 cm from Loading Motor Axis and 0.01 Nm of Frictional Resistance at Joints O, F & E.

Equations (5.11) and (5.8) make it possible to design a control profile in terms of raw sensor readings as a function of some desired F_{femur}^{shear} profile, which may be designed as a function of cycle position. Depending on the frictional properties of the joints, mass and position of the counterweight, analysis such as that performed for Figure 101, Figure 102 and Figure 103 must be performed first to consider the achievable range. Effectively, this sets the theoretical bounds for any defined function F_{femur}^{shear}.

5.5.3 System Identification

The derivations in the previous two sections allow the design of a reference signal in the form of raw sensor A/D readings. It is advantageous to generate the controller reference in terms of raw A/D values as opposed to motor torque or desired load in order to save computational power on the micro-controller. The task of designing a controller for active loading is not as straightforward as the design process for speed control. It was decided that a

system model needed to be developed between the motor input and sensor output in order to inform the controller design process.

Traditional system identification methodology was applied to determine the frequency response of the system. The system input is the percent duty cycle of a PWM modulated 9V voltage signal, scaled between 0-255. The output is the load sensor A/D value as sampled by the microcontroller. The system identification process involves driving the loading motor with a defined input in the form of *x(t)*:

$$x(t) = A_O + A_i \sin(\rho_k t)$$

Where A_O is an offset PWM duty cycle, A_i is the amplitude of the input signal and ρ_k is the frequency of the input signal. Assuming that the system is linear, the sensor output will have the form *y(t)*:

$$y(t) = B_O + B_i(\rho_k) \sin(\rho_k t + \phi_k(\rho_k))$$

Where B_o is an offset. $B_i(\rho_k)$ is the amplitude of the response $\phi_k(\rho_k)$ is the phase of the response, both of which are dependent on the driving frequency ρ_k. The function *x(t)* is designed in such a way that it does not cross zero, in order to keep the torque direction from changing which may result in loss of contact within the motor gears. The output signals were sampled at 100 Hz. Examples of an input signal and the resulting output are shown in Figure 104 and Figure 105 respectively for $\rho_k = 2.0\ Hz$.
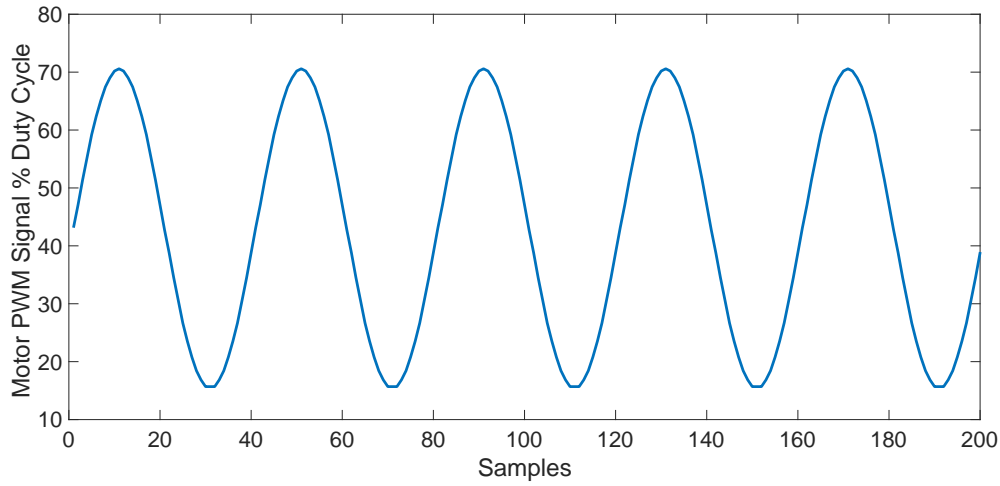
Figure 104: Example Input Signal – Motor input signal for system ID at 2.0 Hz.
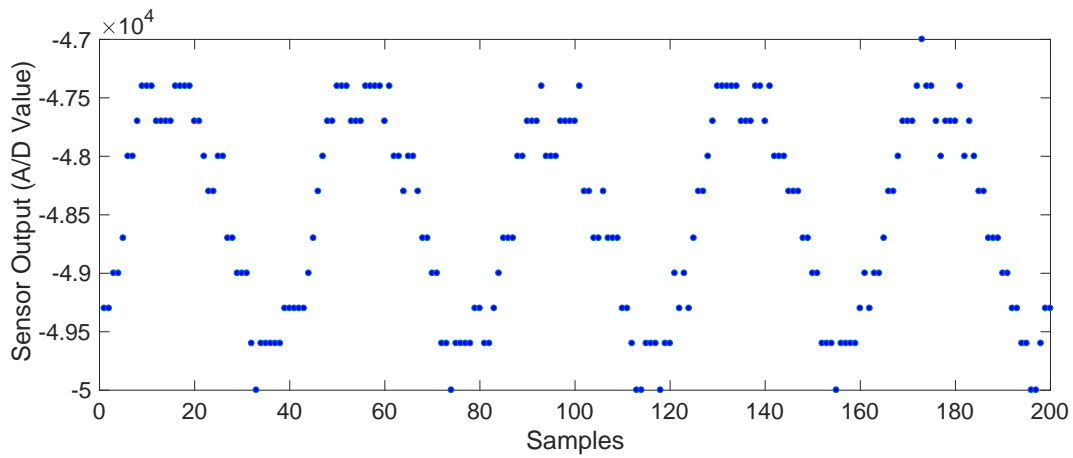
Figure 105: Example Output Signal - Raw sensor output post-A/D conversion for input signal shown in Figure 104.

System identification was performed for discrete frequencies ranging from 0.1 Hz to 25 Hz resulting in the bode plot shown in Figure 106. It is assumed that accuracy is lost towards the higher range of the frequency range due to the relatively low sample rate (e.g. at 100 Hz sampling rate a 20 Hz input has $n_{samples} = 5$). Identification was only performed for system

while static, meaning the drive motor was not operated. The linkage geometry was maintained such that $\theta_A = 0$.
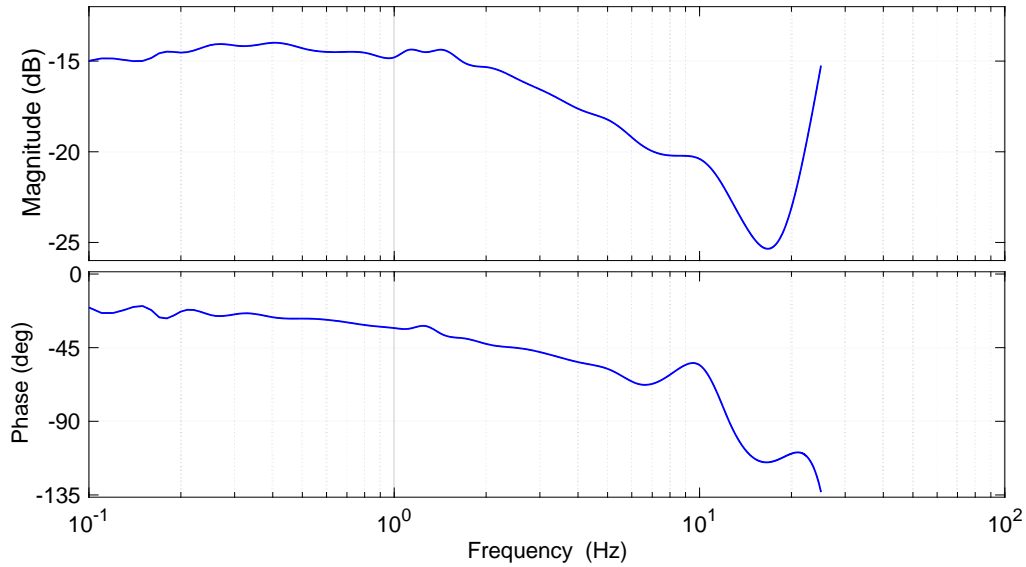
Figure 106: System ID Result - Bode plot relating sensor output to load motor PWM duty cycle.

The system does not behave as either a first or second order system. At lower frequencies, the response is fairly flat in terms of gain, and there is a constant lag of about 30°. Above about 1.0 Hz input frequency the gain begins to roll off in an atypical fashion and the phase lag increases. As the bode plot does not display the typical characteristics of common systems (e.g. 20-40 dB/decade gain roll-offs etc...), no mathematical model was developed to describe the output to input relationship. Therefore, all controller design was performed in the frequency domain.

5.6 Controller Design and Implementation

The work described so far in this chapter has laid out the framework for developing a comprehensive control scheme and algorithm for active loading control.

5.6.1 Development of Control Law

Using the frequency response data of the system, a control law was developed by considering the open loop stability criterion. The final control law developed is a proportional-integral formulation given as:

$$u_{D,j} = G_P e_{D,j} + G_I \sum_{j=0}^{j} e_{D,j} \tag{5.12}$$

Where u_D is the duty cycle of a PWM voltage signal driving the load motor, e_D is the error between the sensor output and reference, and G_P and G_I are the proportional and integral gains respectively. The subscript j represents the loop iteration of the controller. The full system including the PI controller can be expressed by the block diagram in Figure 107.
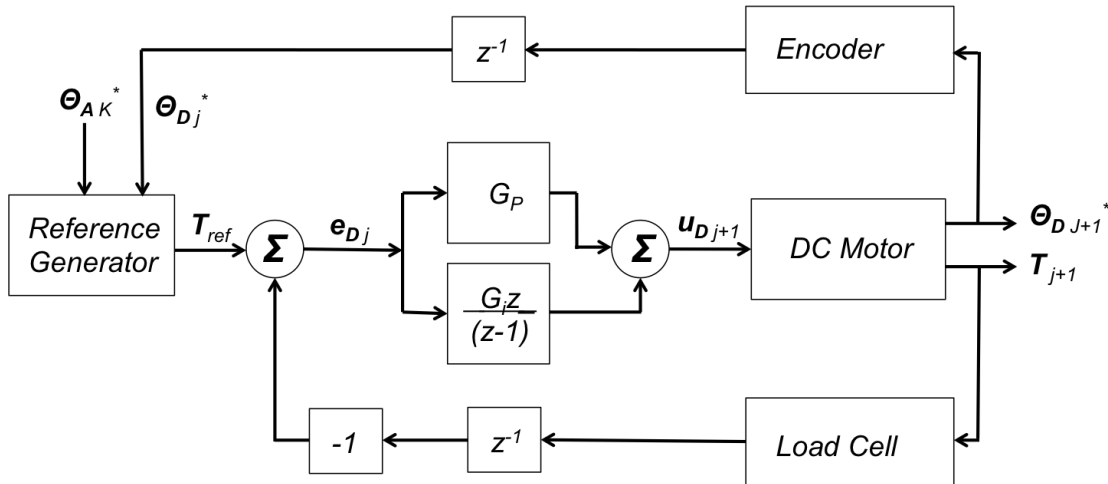
Figure 107: Active Loading Control System Block Diagram – The load cell is used for torque estimation and feedback to a PI controller.

The proportional and integral gains were derived by designing a control system such that the closed loop frequency response exhibits a gain of 0 dB and a phase lag lower than 180° at approximately 1.0 Hz. The gains were tuned to:

$$G_p = 0.23$$

$$G_I = 0.25$$

The z-domain transfer function for this controller between the input U, and error signal E can be expressed as:

$$\frac{U}{E} = \frac{0.48z - 0.23}{z - 1} \tag{5.13}$$

The controller, open loop, and closed loop frequency responses are shown in Figure 108,

Figure 109 and Figure 110 respectively.
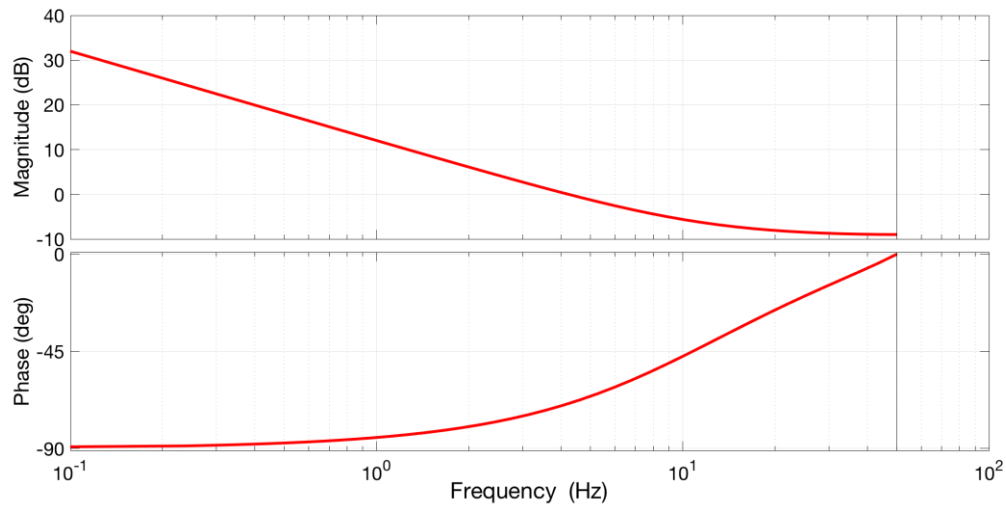
Figure 108: Controller Frequency Response – The frequency response of the PI control law implemented.
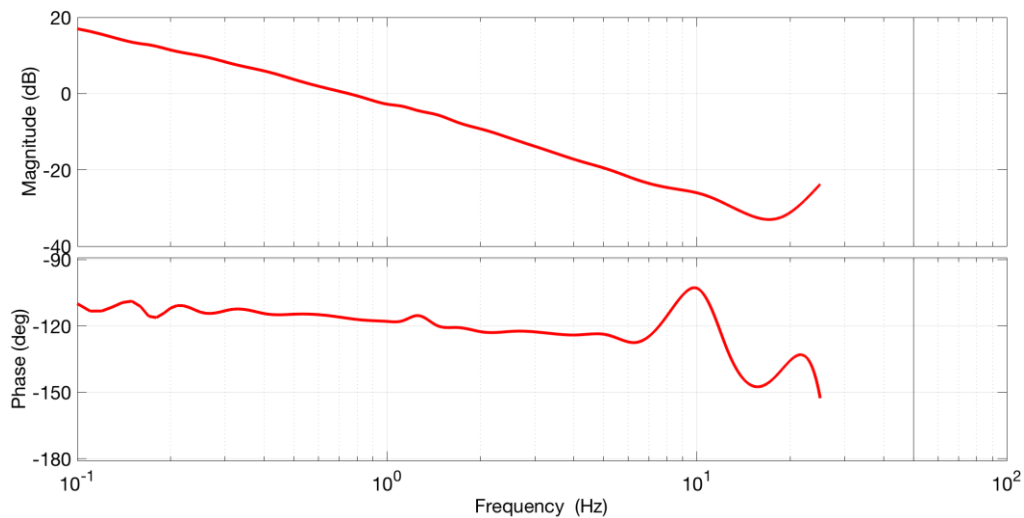
Figure 109: Open Loop Frequency Response – The open loop system has a 0 dB crossover at ~0.8 Hz with a sufficient phase margin to suggest stability.
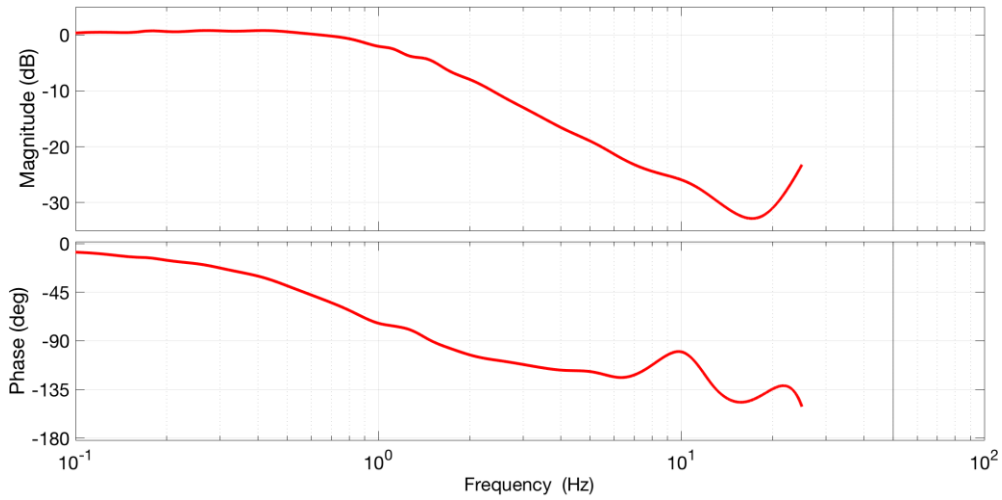
Figure 110: Closed Loop Frequency Response

The complete system has an open-loop 0 dB crossover frequency of 0.8 Hz, well above the operating cycle of the system (~0.5 Hz maximum). From the open loop frequency response the system is expected to be stable within the anticipated operational bandwidth. The closed loop system has a bandwidth from DC up to about 1 Hz.

5.6.2 Hardware Implementation

As stated previously, the control scheme is run on an Arduino Mega microcontroller. The full signal flow of the JM2 system with active loading control is shown in Figure 111. Components mounted on the actual JM2 device are marked, in addition to the components included on a single circuit to facilitate transfer and conditioning of signals between the microcontrollers to the device.
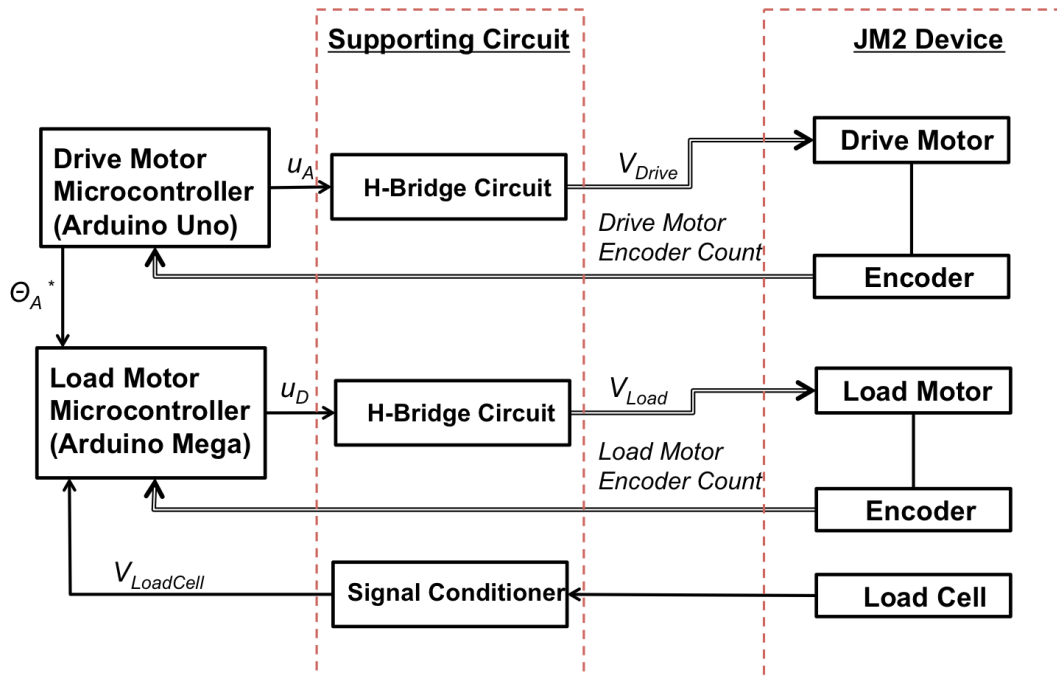
Figure 111: JM2 Full Supporting Hardware and Signal Flowchart

Since the active loading control program needs an estimate of the drive motor position, an inter-integrated circuit (I^2C) connection is made between the loading and driving microcontrollers. The communication is one-way, with the loading microcontroller requesting position estimates as necessary. The I^2C protocol limits communication to a rate of 1 byte of data per transaction. This limitation means that only an integer between 0-255 can be exchanged at a time, hence why the cycle position is divided into 255 steps from 0-254. A position of 255 is reserved to indicate a "resting" period, when the drive motor does not rotate. Aside from the communication related to drive motor position, each microcontroller operates independently with no knowledge of the other's status. Like the drive motor controller, the active loading controller operates on a 100 Hz sampling rate. The entire system is run off of two 9V power supplies.

5.7 Controller Testing

Testing of the active loading control system was directed at assessing its potentials and limitations under representative conditions. All testing was performed using an analogue stifle as opposed to explanted biological joints in the interest of ethics. The system was operated under the medium range of flexion and a 100 g counterweight was mounted 4.5 cm from the loading motor shaft. The drive motor was set to run at constant 0.25 Hz cycle rate.

5.7.1 Loading Profile Design

During testing, further limitations of the loading profile became apparent, indicating that care must be taken when designing the profile. Shown in Figure 112, are the load cell outputs under three conditions while the system runs at 0.25 Hz in the clockwise direction: 1) loading motor applies no torque; 2) loading motor applies maximum clockwise torque; 3) loading motor applies maximum counterclockwise torque.
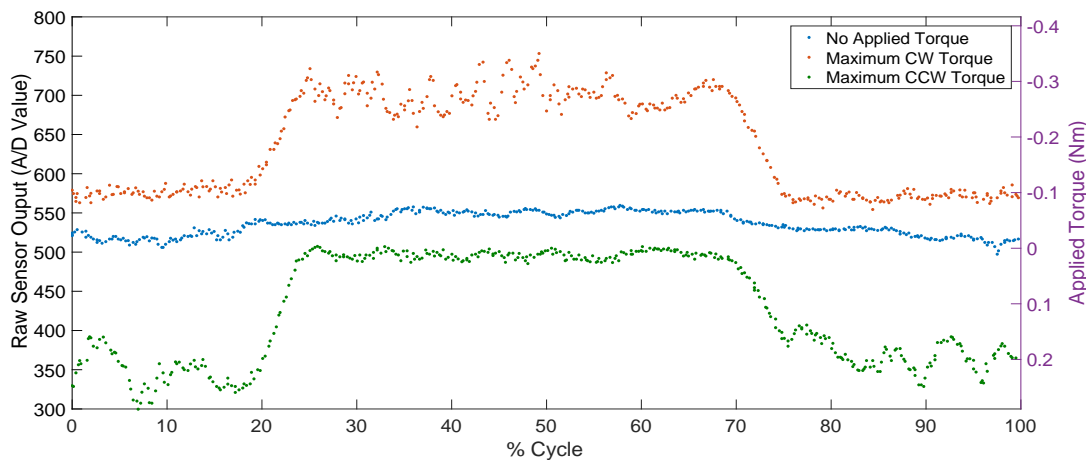
Figure 112: Torque Application Limits During Actuation – The maximum applicable torque in either direction is dependent on the position in the cycle due to the competing and supporting actions of both actuators.

From Figure 112 it is clear that the range of applicable torques is a function of cycle position when the system is being actuated. This limitation is due to the relative effects of both motors as the cycle progresses. For example, consider the case of applying the maximum counterclockwise torque in the case that the driving motor rotates clockwise. This case corresponds to applying the maximum amount of compression on the stifle throughout the cycle. Between 0-25% and 75-100% of the cycle, the drive motor and loading motor actions both result in effectively compressing the linkage system. Effectively, they apply torques that would result in opposing motion if either is operated individually. Therefore, during this portion of the cycle, it is possible to apply a significantly higher amount of compression. Between 25-75% of the cycle, the action of the drive motor constantly relieves the system of any compression applied by the loading motor. Effectively, both motors are pushing the system in the same direction. Therefore, only a limited amount of compression can be applied in this region. The opposite trends are seen in the case of applying maximum tension by application of maximum clockwise torque. Effectively, this results in two regions in the cycle where compressive and tensile loading limits vary, Figure 113. Using the relationship derived in Equation (5.11), it is possible to determine the limits of the applied femoral shear force, Figure 114.
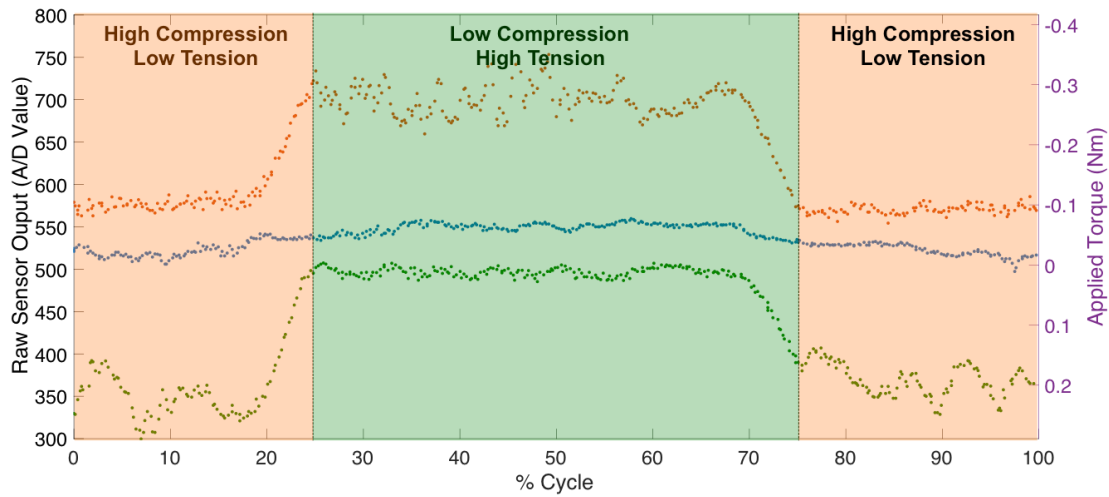
Figure 113: Loading Limit Regions – The torque application limits result in two regions where either high compression/low tension can be applied, or low compression/high tension can be applied.
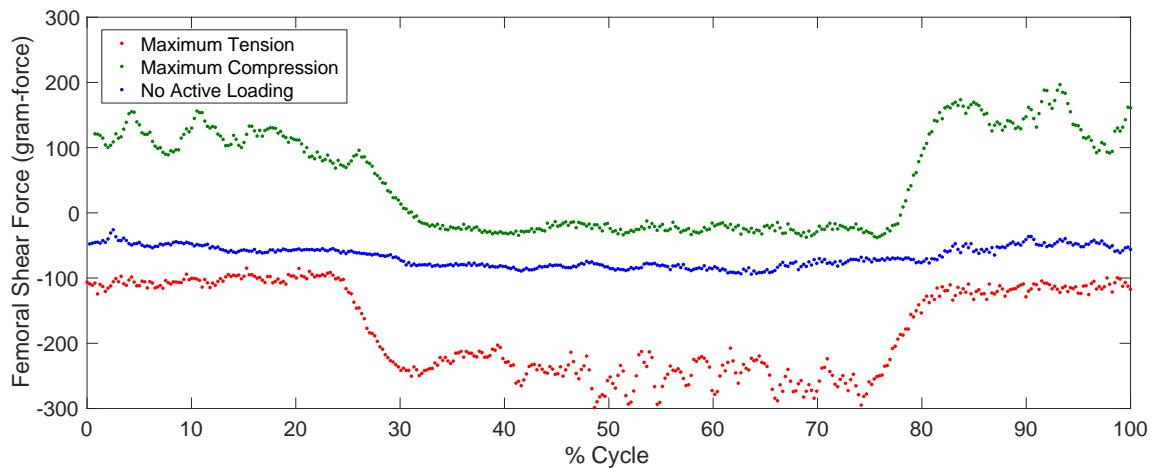
Figure 114: Loading Limits in Terms of Applied Femoral Shear Force

It should be noted from Figure 113 and Figure 114 that the force experienced when no torque is applied at the loading motor tends towards tension. This is expected given the location of the counterweight, which adds a tensile preload to the system, or a clockwise torque.

These limits must be considered when designing the loading reference profile for control. They essentially describe the limits of controllability and capability of the system given the geometry and actuators. Therefore, any desired loading profiles must not cross either the maximum tension or maximum compression limits. Furthermore, crossing the no active loading limit results in a change of direction of the applied loading torque, which may result in unanticipated effects due to backlash in the motor gears. Three profiles were defined as values of raw load sensor reading for testing purposes. The first two were designed to apply compression at the joint, and are defined between the maximum CCW torque and no applied torque limits. The third profile was designed to span as much of the applicable loading range as possible. The profiles are designed as functions of the discrete cycle position, θ_A^*, shown below and plotted in Figure 115.

$$Profile\ 1: \quad O_{LC} = \begin{cases} 525 - 100\cos\left(\dfrac{\theta_A^*}{254} * 2 * \pi\right) & for\ 0 < \theta_A^* \le 67 \\ 535 & for\ 67 < \theta_A^* \le 186 \\ 525 - 100\cos\left(\dfrac{\theta_A^*}{254} * 2 * \pi\right) & for\ 186 < \theta_A^* \le 254 \end{cases}$$

$$Profile\ 2: \quad O_{LC} = \begin{cases} 525 - 100\cos\left(\dfrac{\theta_A^*}{254} * 2 * \pi\right) & for\ 0 < \theta_A^* \le 60 \\ 515 & for\ 60 < \theta_A^* \le 195 \\ 525 - 100\cos\left(\dfrac{\theta_A^*}{254} * 2 * \pi\right) & for\ 195 < \theta_A^* \le 254 \end{cases}$$

$$Profile\ 3: \quad O_{LC} = 525 - 100\cos\left(\dfrac{\theta_A^*}{254} * 2 * \pi\right)$$
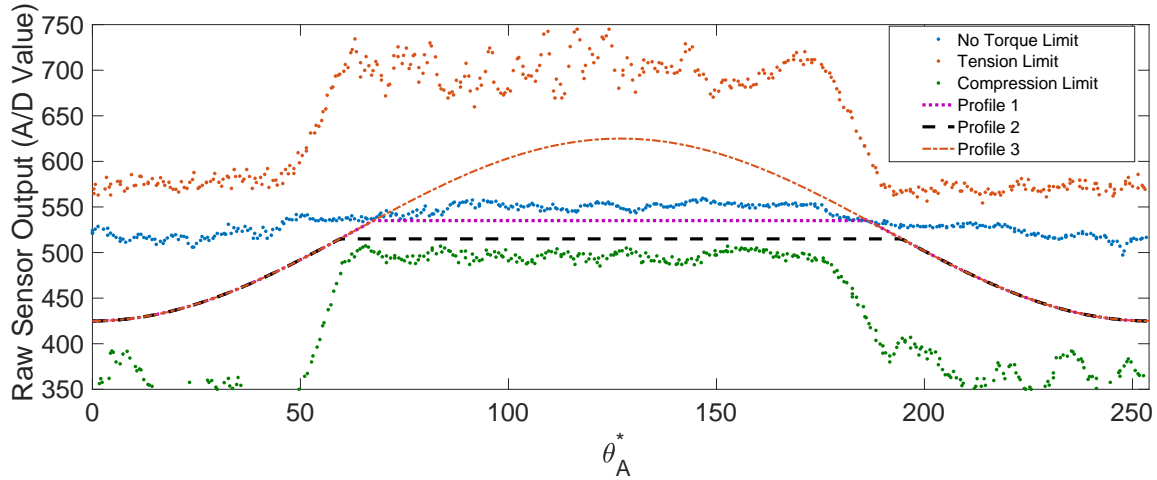
Figure 115: Loading Profiles Used for Testing and Their Relationship to Loading Limits – In order to determine how the identified torque limits affect the application of controlled loads, three loading profile were designed to span different ranges and their tracking ability was investigated.

The difference between profiles 1 and 2 is their values during the low compression region of the cycle. Profile 1 tends towards the no torque limit, while profile 2 tends towards the maximum compression limit. Profile 3 was purposefully designed to apply both compression and tension in order to evaluate how well the system handles a change in direction of loading.

5.7.2 Loading Profile Tracking Results

The developed control system was used to implement the three loading profiles. The measured sensor values are shown along with their respective reference signals in Figure 116, Figure 117 and Figure 118.
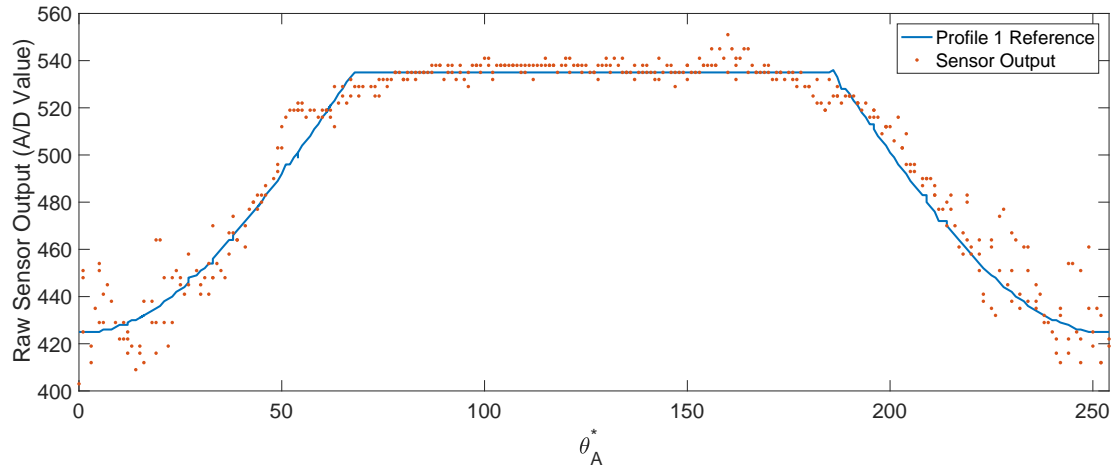
Figure 116: Profile 1 Tracking Results – Aside from measurable sensor noise and quantization error, the designed controller is able to track profile 1 with favorable accuracy.
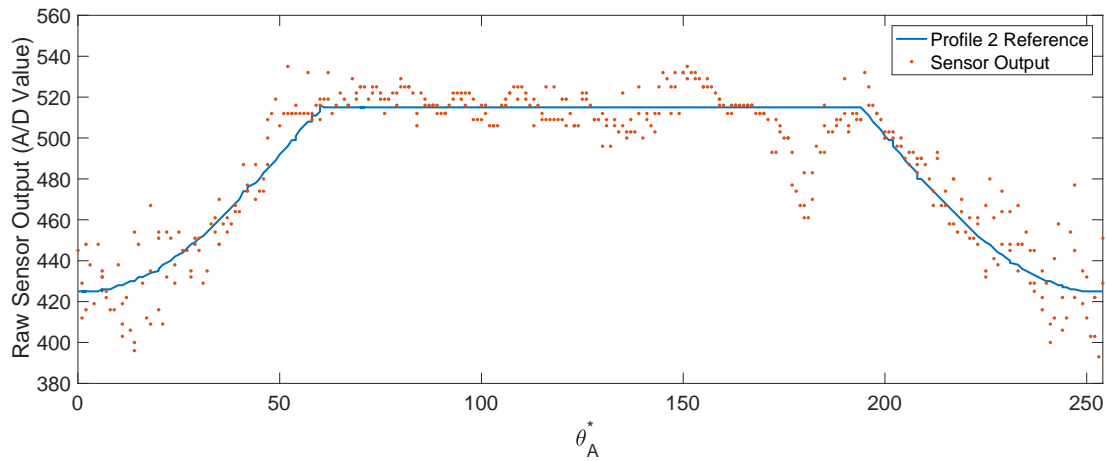
Figure 117: Profile 2 Tracking Results – In addition to the noise observed with profile 1, there is consistent error at around $\theta_A^* = 175$.
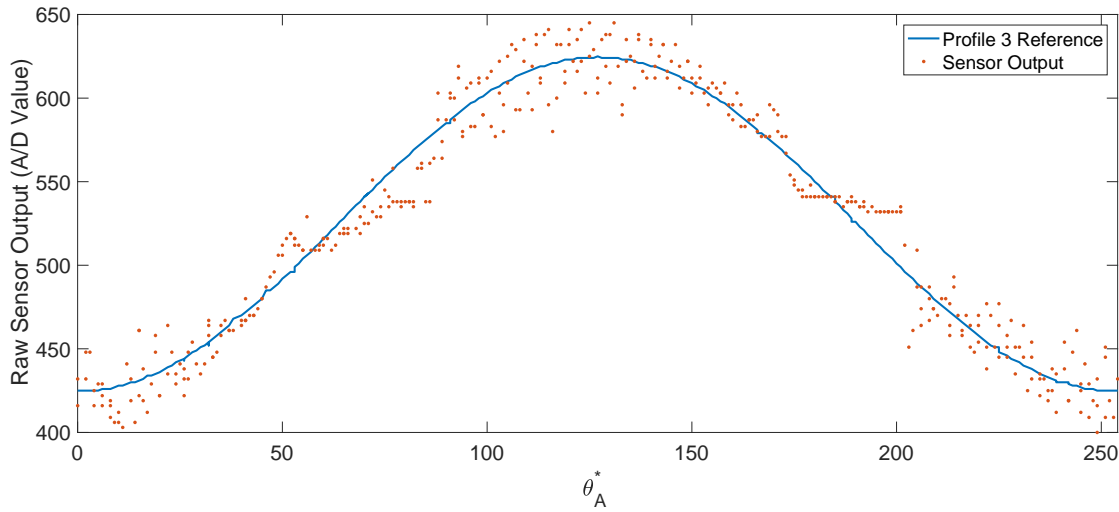
Figure 118: Profile 3 Tracking Results – Profile 3 tracking is consistently lost when the load switches from compressive to tensile and vice-versa.

Although this data is taken from a single cycle, these are representative of the tracking abilities for each profile. There is measurable quantization error within the sensor reading due to the analog to digital conversion. This error is on the order of +/- 6 A/D values, and its effect can be clearly seen in all the profiles, particularly in Figure 116 over the flat constant torque region. In addition to the quantization error, there is evenly distributed error in most cases. However, in general the reference tracking is relatively good for Profile 1.

The tracking for Profile 2 shows a consistent error around $\theta_A^* = 175$, where the sensor output is significantly lower than the desired profile. This feature is seen when tracking Profile 1 but to a much lesser extent. Furthermore, the constant torque region of Profile 2 exhibits noisier tracking than it's counterpart in Profile 1. Profile 3 shows two regions where tracking is not maintained well, which correspond with the points at which the loading profile switches from compressive to tensile and vice-versa.

5.8 Discussion

In general the reference tracking is accurate but exhibits low precision. Much of this can be attributed to quantization error and sensor noise. The relatively high quantization error makes the application of higher proportional gain impracticable. Increasing it would make the controller less robust to this error and lead to instability. As a result, most of the control is due to integral action, which can be slow in correcting other errors. The best solution is simply the use of a higher bit A/D converter. This is not the only limitation of the system however. Several of the features mentioned in the previous section give insight to additional limitations and further highlight the importance of reference design for accurate control.

The difference between tracking Profile 1 and Profile 2 are fairly remarkable, particularly over the constant torque region. Given that the two profiles are nearly identical aside from the constant torque region, one would initially expect their performance to be comparable. The loss of tracking in Profile 2, highlighted in Figure 119, can be explained by transition between the low compressibility region to high compressibility region.
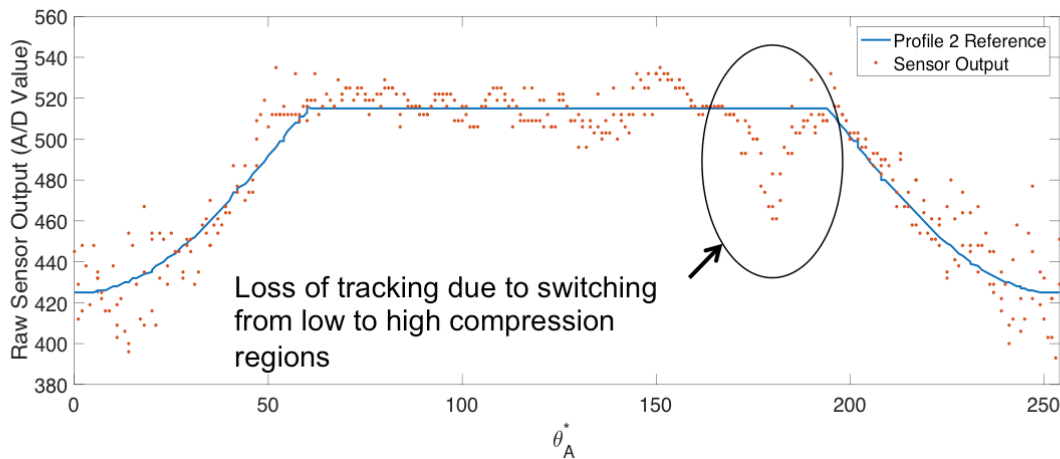
Figure 119: Loss of Tracking in Profile 2 – The encircled region indicates a representative loss of tracking due to switching between regions of low compression to high compression.

Effectively, when transitioning between the two regions, the dynamic range between motor input and applied torque suddenly changes, Figure 120. During this particular transition, the dynamic range increases dramatically, as can be seen by the sudden ability to apply significantly more compression. The same range of motor inputs has the potential to create a wider range of applied torques. Initially, it may be expected that the transition should affect both profiles equally. However, because Profile 2 tracks closer to the maximum compression limit than Profile 1, it requires a higher motor input. The input must quickly decrease when shifting to region where the dynamic range is greater. As a result, the higher the input in the low dynamic range region, the larger the shift in input value must be in order to correct for the transition.
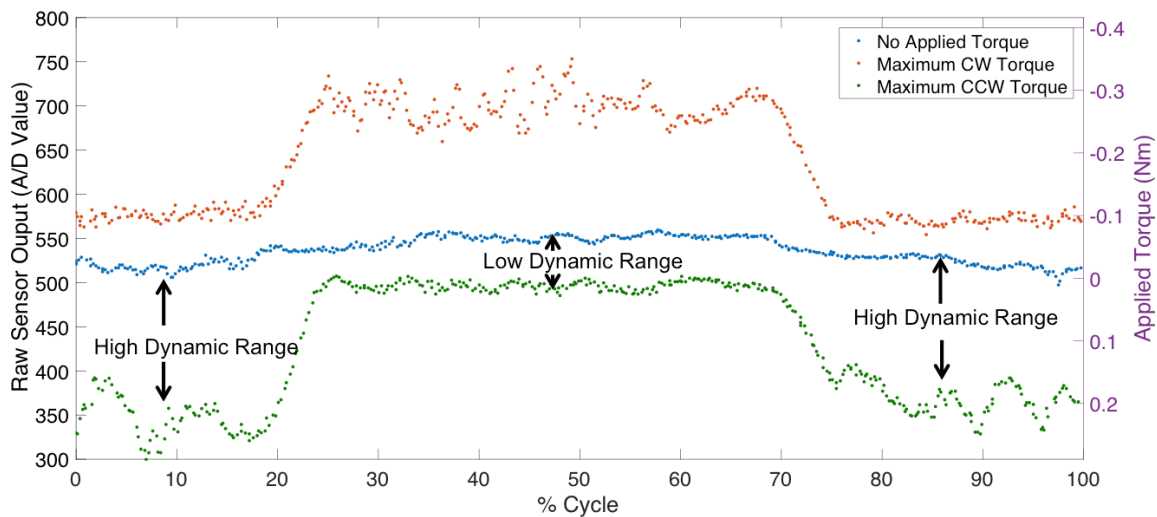
Figure 120: High and Low Dynamic Range Regions of Compression – Effectively, the system displays two characteristic dynamic ranges between motor input and applied torque as shown. The implications of this are that there is a sudden change in the amount of torque that the motor can apply under the same input range.

A few solutions may prevent this issue. First, the reference can be designed such that the motor input over the constant torque region remains relatively low, similar to Profile 1. In fact,

it may even span the entire range as long as it tends closer to a low input prior to switching regions. Another approach is to design an adaptive control law that accounts for the shift in gains. This would also need to take into account the fact that the trend is the opposite when applying tension.

The two areas in Profile 3 where tracking is poorly maintained correspond the points where the reference switches between compression and tension, Figure 121. This is an indication that backlash in the motor gearbox results in a loss of ability to apply a torque. As gear tooth contact is lost, so is the ability to apply any controlled torque, and as the contact is recovered, that ability is returned. This represents a fundamental limitation in using a geared motor to perform active loading control. Although a direct drive motor could be used, they typically exhibit lower torque capacity.
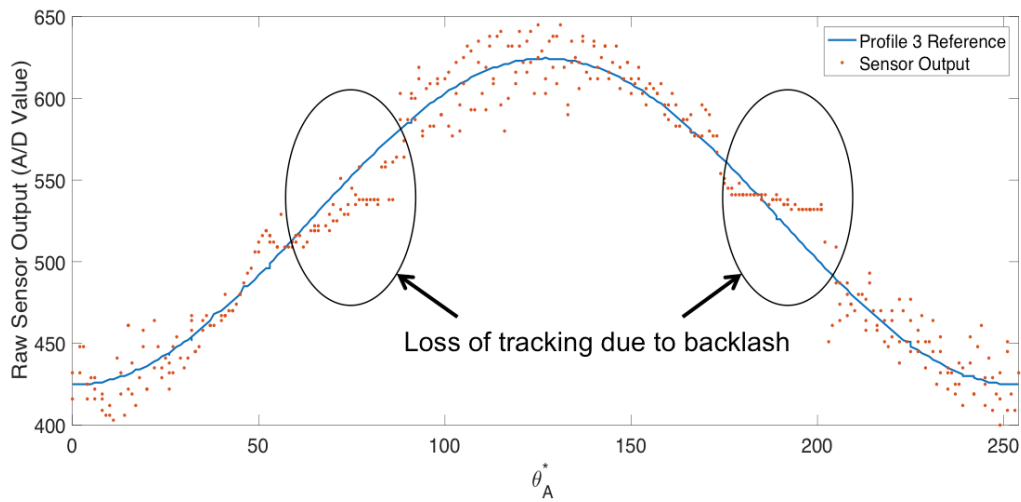
Figure 121: Loss of Tracking in Profile 3 – The error seen in tracking of profile 3 is related to backlash in the system when the direction of the applied torque is changed.

A final observation is the relatively wide dispersion of sensor readings over certain regions of the cycle. This phenomenon can be seen for example in Figure 121 near the maximum and minimum parts of the reference profile. It is present in all three profiles. The same effect is seen in the torque limits over certain parts of the cycle, Figure 122. The reasons for this effect are not immediately clear. However, they occur at parts of the cycle where the actions of the two motors oppose each other. Therefore, it is speculated that the effect is due to a coupling between the two motors and their control systems. For example, consider that the action of the loading motor acts to resist the motion of the linkage system, resulting in the application of compression. This action acts as a disturbance to the drive motor, and the drive motor controller must compensate to overcome this increased resistance in order maintain a constant speed. The resulting increase in drive motor torque results in further compression of the system, which is in turn sensed by the load motor controller as a new disturbance. Now the load motor control system must compensate. This interaction continues, and it can be expected that this results in a coupling effect between the motors; where both control systems are constantly attempting to compensate for the effects of the other.
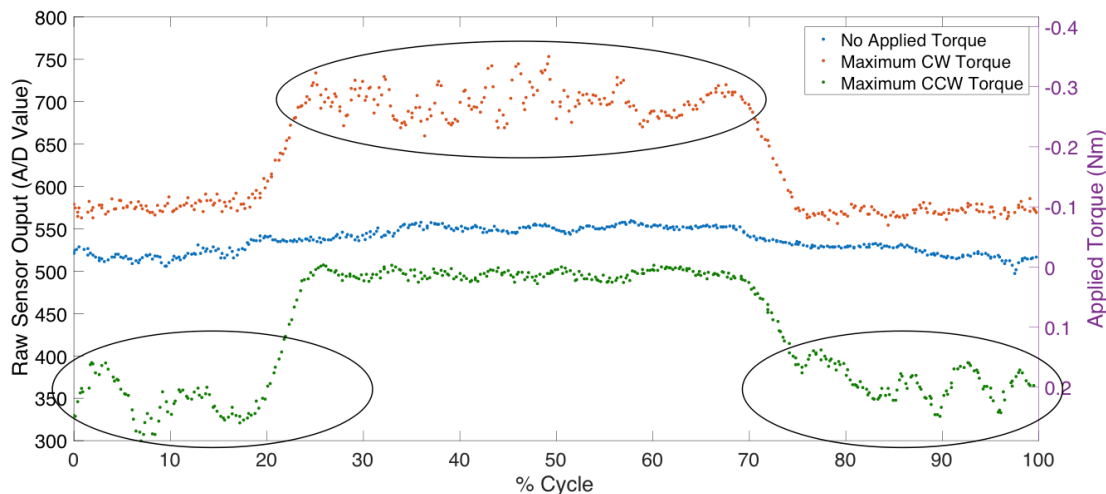
Figure 122: Torque Application Limits – Encircled regions highlight significant dispersion in the load cell measurement.

The current assumption that both motors can be operated by independent control systems neglects to take this coupling into account. The approach to solving this issue is the development of a single multi-input multi-output control system that takes into account the coupling effects of the two motors.

The results of testing have highlighted the importance of effective profile design. The performance of the controller is sensitive to the desired loading profile. To conclude, a list of profile design "rules" can be listed:

1. The profile must be designed such that exists between either the no applied torque limit and maximum counterclockwise torque limit, or the no applied torque limit and the maximum clockwise torque limit.

2. The profile must not cross the no applied torque limit as to prevent effects of backlash in the loading motor.

3. In regions of low gain between the motor input and applied torque, the profile should tend towards the no applied torque limit, especially when approaching the cycle position where the system switches to a high gain region.

5.9 Conclusions

In summary, the development and testing of the active loading system has shown that it is possible to apply a limited range of joint loads with fair accuracy using the system. Extensive modeling was performed to relate applied motor torque to internal loading of the stifle joint. The formulation derived here is based on controlling femoral shear load. However, it can be

expanded to consider any component of the joint load, as they are all coupled and their magnitudes must ultimately satisfy the dynamic constraints of the system's motion.

Work directed at using current sensing as a feedback method for estimating motor torque and ultimately applied load proved that the frictional properties of the motors used are not comparable and that such an approach would require individual calibration of each device. Therefore, efforts were focused on using an instrumented link to estimate applied torque and loads. Although the chosen sensor coupled with microcontroller has relatively low precision, active loading control was achieve with some limitations.

Testing of the control system demonstrated the ability to apply controlled compressive loads on the stifle joint as a function of the cycle position. The investigation revealed several conditions that must be met when defining a reference curve for control. These conditions are a combination of limitations set by the system geometry, the motor capacities and the neglected coupling between the two control systems. Nevertheless, the work outlined in this chapter has set precedent for utilizing the JM2 system with active loading control capability.

6

Conclusions

6.1 Summary of Research

The work presented in this dissertation has been directed towards the development and demonstration of a novel system for studying OA using a mouse model. In Chapter 1, the necessity of this system and research was presented. A diagnosis of OA is life altering for patients. With no comprehensive treatment options aside from pain management or surgical joint replacement, patients are fated to continuing pain and loss of mobility. The current research models aimed at developing OA treatments are limited, and hinder progress.

Chapter 2 provided a detailed outline of the human knee joint, the most prominent joint to feature OA pathology. The complexity of knee's biomechanics have driven decades of research, much of which has led to the development of numerous knee simulating devices. Despite the wide portfolio of existing systems, none were found in the literature with the capabilities designed for with the joint-in-motion devices.

In Chapter 3, the first generation system was introduced. The JM1 was designed and fabricated to repeatedly actuate amputated murine stifle joints during extended periods of culture. Although limited in capability, the device was used for several experimental investigations of glucose concentration in the culture media. Results suggested that higher

levels of glucose concentration in the culture media promote loss of articular cartilage when cultured under dynamic actuation. Samples cultured under those conditions showed weaker Safranin-O staining at the articular surfaces.

Chapter 4 introduced the second-generation joint-in-motion system, JM2. The design process of the device was outlined with special attention paid to addressing issues related to repeatability, reliability and usability identified with the JM1. The system exhibits a rigid linkage system, geometrically designed to repeatedly actuate an amputated stifle joint through controlled flexion cycles. A custom mounting system consisting of clamps and a mounting fixture was developed to minimize human error associated with device set-up. Through the action of a feed-forward and PI control system, the JM2 system accurately and reliably actuates cultured stifle joints. Experimental use of the system shows its aggressive effects during culture. Eight hours of actuation proved to effectively have a saturating effect of joint damage to the point that no differences were seen between samples actuated at 0.25 Hz and 0.50 Hz cycle rates. However, shorter durations of actuation demonstrated that a range of damage could be induced.

In Chapter 5 the capabilities of the JM2 system to accomplish active loading control were explored and developed. Research into sensing methods showed that the use of a load cell on a system link could be used to predict and control the shear load at the femoral surface. Through thorough analytical and experimental modeling, a control system was developed to track user defined loading profiles. Several limitations of the profiles were notes however, due to a combination of effects from the system's mechanical geometry, the torque capacity of the loading motor and unaccounted for couplings between the two independent controllers. However, acceptable tracking was demonstrated given a satisfactorily designed reference profile.

The objectives outlined in Section 1.3 have all been successfully addressed. The JM2 system was developed to culture and actuate amputated stifle joints. Several analytical models were developed to describe the state of loading at the stifle joint. Control systems were developed to effectively run the developed system. And finally, investigations into different actuation cycles were performed and their effects on the health of explanted joints were noted.

6.2 Unique Contributions

The uniqueness of this research lies in the novelty of the developed system as a whole. The combination of mechanical, electrical and controller design for the desired application is non-trivial and represents significant progress into the development of a novel research avenue. To date, no similar system has been developed with the capability to perform long-term *in-vitro* culture of whole joints under actuation at the scale presented here. Furthermore, the focus on design and fabrication simplicity as well as usability has established the system as an accessible alternative to current OA research models.

Overall the research presented here is meant to provide a comprehensive overview. The analytical and experimental models developed fully characterize the joint-in-motion system in terms of dynamics and controllability. In combination, the development of the physical system, development of supporting hardware and software, and the development of comprehensive engineering models provide a framework for extensive future research in to the pathology and treatment options of OA.

6.3 Suggestions for Future Directions

As this research has been directed towards the development and demonstration of a novel system, it establishes a framework for an extensive range of future work. Firstly, there are numerous modifications that can be made to the JM2 device itself to further facilitate its use and functionality. Chapter 5 highlighted several limitations related to the assumption that the two control systems of the device can be operated independently. One suggested avenue of future work is to develop a single multi-input multi-output controller that accounts for coupling in the system. Preliminary steps are already being taken combine all the controller software to a single, more powerful microcontroller. Such a design would allow for higher precision in position estimation since the limitations of I^2C communication are eliminated. Furthermore, the performance of both controllers can be expected to benefit from higher order A/D and D/A conversions due to the higher precision of input and output signal sampling. Higher precision in the outputted PWM motor signals would allow for more subtle control of both speed and applied torque. High precision in the sampled load cell signal would reduce quantization error.

The novel nature of the JM2 system makes it a unique test bed for a myriad of investigations related to OA. The system can be used to vary and control numerous aspects of active explanted stifle joint cultures including range of motion, relative durations of activity and rest periods, cycle rates at either constant and variable profiles and mechanical loads at the joint. The use of the system to investigate the effects of cycle rate and duration of activity has been demonstrated here. However, any combinations of these factors can effectively be researched. In combination with investigating culture media additives such as growth factors or inflammation promoting substances, the variety of mechanical variables opens a field of unexplored research opportunities.

Finally, future work can also be directed to alternative methods of joint health assessment. The nature of using animal samples limits the total number of samples that can be used for experimentation. Ethically and practically, experiments should be designed to use the least number of samples possible. Although the use of Safranin-O staining showed some measurable differences between differently cultured samples, the development of an assessment method that is more forgiving of the low sample numbers would greatly increase the efficiency of future research.

7

List of References

[1] Ralphs, J. R., & Benjamin, M. (1994). The joint capsule: structure, composition, ageing and disease. *Journal of anatomy*, *184*(Pt 3), 503.

[2] Thysen, S., Luyten, F. P., & Lories, R. J. (2015). Targets, models and challenges in osteoarthritis research. *Disease Models and Mechanisms*, *8*(1), 17-30.

[3] A.R. Poole, F. Guilak, S.B. Abramson, Etiopathogenesis of osteoarthritis in Osteoarthritis, Diagnosis and Medical management, 4th. edition, R.W. Moscowitz, R.D. Altman, M.C. Hochberg, J.A. Buckwalter, V.M.Goldberg, eds., Wolters Kluwer/Lippincott Williams and Wilkins, Philadelphia, pp. 27–49, 2007 Ligaments

[4] Huiskes, R., R. Van Dijk, A. De Lange, H. J. Woltring, and Th. J. G. Van Rens. "Kinematics of the Human Knee Joint." *Biomechanics of Normal and Pathological Human Articulating Joints*. Ed. Necip Berme, Ali E. Engin, and Kelo M. Correia De Silva. Dordecht: Martinus Nijhoff, 1985. 165-88. Print. NATO ASI Ser.

[5] Most, E. (2000). *Development of a 6-DOF robotic test system for studying the biomechanics of total knee replacement* (Doctoral dissertation, Massachusetts Institute of Technology).

[6] Girgis, F. G., Marshall, J. L., & Jem, A. A. M. (1975). The Cruciate Ligaments of the Knee Joint: Anatomical. Functional and Experimental Analysis. *Clinical orthopaedics and related research*, *106*, 216-231.

[7] Welsh, R. P. (1980). Knee joint structure and function. *Clinical orthopaedics and related research*, *147*, 7-14.

[8] Bach, J. M., & Hull, M. L. (1995). A new load application system for in vitro study of ligamentous injuries to the human knee joint. *Journal of biomechanical engineering*, *117*(4), 373-382.

[9] Nilsson, J., & Thorstensson, A. (1987). Adaptability in frequency and amplitude of leg movements during human locomotion at different speeds. *Acta Physiologica Scandinavica*, *129*(1), 107-114.

[10] Thysen, S., Luyten, F. P., & Lories, R. J. (2015). Targets, models and challenges in osteoarthritis research. *Disease Models and Mechanisms*, *8*(1), 17-30.

[11] Farrokhi, S., Meholic, B., Chuang, W. N., Gustafson, J. A., Fitzgerald, G. K., & Tashman, S. (2015). Altered frontal and transverse plane tibiofemoral kinematics and patellofemoral malalignments during downhill gait in patients with mixed knee osteoarthritis. *Journal of biomechanics*, *48*(10), 1707-1712.

[12] Weyand, P. G., Sandell, R. F., Prime, D. N., & Bundle, M. W. (2010). The biological limits to running speed are imposed from the ground up. *Journal of applied physiology*, *108*(4), 950-961.

[13] Costigan, P. A., Deluzio, K. J., & Wyss, U. P. (2002). Knee and hip kinetics during normal stair climbing. *Gait & posture*, *16*(1), 31-37.

[14] Kautz, S. A., Brown, D. A., Van der Loos, H. F. M., & Zajac, F. E. (2002). Mutability of bifunctional thigh muscle activity in pedaling due to contralateral leg force generation. *Journal of neurophysiology*, *88*(3), 1308-1317.

[15] Bini, R. R., & Diefenthaeler, F. (2010). Kinetics and kinematics analysis of incremental cycling to exhaustion. *Sports Biomechanics*, *9*(4), 223-235.

[16] Kutzner, I., Heinlein, B., Graichen, F., Rohlmann, A., Halder, A. M., Beier, A., & Bergmann, G. (2012). Loading of the knee joint during ergometer cycling: telemetric in vivo data. *journal of orthopaedic & sports physical therapy*, *42*(12), 1032-1038.

[17] Poole, A. R. (2012). Osteoarthritis as a whole joint disease. *HSS Journal*, *8*(1), 4-6.

[18] Driban, J. B., Hootman, J. M., Sitler, M. R., Harris, K., & Cattano, N. M. (2015). Is participation in certain sports associated with knee osteoarthritis? a systematic review. *Journal of athletic training*.

[19] Felson, D. T. (2013). Osteoarthritis as a disease of mechanics. *Osteoarthritis and cartilage*, *21*(1), 10-15.

[20] Hootman, J. M., & Helmick, C. G. (2006). Projections of US prevalence of arthritis and associated activity limitations. *Arthritis & Rheumatism*, *54*(1), 226-229.

[21] Perry, J., Antonelli, D. A. N. I. E. L., & Ford, W. (1975). Analysis of knee-joint forces during flexed-knee stance. *The Journal of Bone & Joint Surgery*, *57*(7), 961-967.

[22] Bourne, R. B., Goodfellow, J. W., & O'Connor, J. J. (1978). A functional analysis of various knee arthroplasties. *Transactions of the Orthopaedic Research Society*, *24*, 160.

[23] Pavlovic, J. L., Kirstukas, S. J., Touchi, H., & Bechtold, J. E. (1994). Dynamic simulation machine for measurement of knee mechanics and intra-articular pressures. *ASME-PUBLICATIONS-BED*, *28*, 277-277.

[24] More, R. C., Karras, B. T., Neiman, R., Fritschy, D., Woo, S. L., & Daniel, D. M. (1993). Hamstrings—an anterior cruciate ligament protagonist An in vitro study. *The American journal of sports medicine*, *21*(2), 231-237.

[25] Churchill, David L., et al. "The transepicondylar axis approximates the optimal flexion axis of the knee." *Clinical orthopaedics and related research*356 (1998): 111-118.

[26] Zavatsky, A. B. (1997). A kinematic-freedom analysis of a flexed-knee-stance testing rig. *Journal of biomechanics*, *30*(3), 277-280.

[27] D'Lima, D. D., Trice, M., Urquhart, A. G., & Colwell Jr, C. W. (2000). Comparison between the kinematics of fixed and rotating bearing knee prostheses. *Clinical orthopaedics and related research*, *380*, 151-157.

[28] Miller, M. C., Zhang, A. X., Petrella, A. J., Berger, R. A., & Rubash, H. E. (2001). The effect of component placement on knee kinetics after arthroplasty with an unconstrained prosthesis. *Journal of Orthopaedic Research*, *19*(4), 614-620.

[29] D'Lima, D. D., Poole, C., Chadha, H., Hermida, J. C., Mahar, A., & Colwell Jr, C. W. (2001). Quadriceps moment arm and quadriceps forces after total knee arthroplasty. *Clinical orthopaedics and related research*, *392*, 213-220.

[30] Patil, S., Colwell, C. W., Ezzet, K. A., & D'Lima, D. D. (2005). Can normal knee kinematics be restored with unicompartmental knee replacement?. *The Journal of Bone & Joint Surgery*, *87*(2), 332-338.

[31] Guess, T. M., & Maletsky, L. P. (2005). Computational modeling of a dynamic knee simulator for reproduction of knee loading. *Journal of biomechanical engineering*, *127*(7), 1216-1221.

[32] Maletsky, L. P., & Hillberry, B. M. (2005). Simulating dynamic activities using a five-axis knee simulator. *Journal of biomechanical engineering*, *127*(1), 123-133.

[33] Yildirim, G., Walker, P. S., & Boyer, J. (2009). Total knees designed for normal kinematics evaluated in an up- and- down crouching machine. *Journal of Orthopaedic Research*, *27*(8), 1022-1027.

[34] Halloran, J. P., Clary, C. W., Maletsky, L. P., Taylor, M., Petrella, A. J., & Rullkoetter, P. J. (2010). Verification of predicted knee replacement kinematics during simulated gait in the Kansas knee simulator. *Journal of biomechanical engineering*, *132*(8), 081010.

[35] Fujie, H., Mabuchi, K., Woo, S. L. Y., Livesay, G. A., Arai, S., & Tsukamoto, Y. (1993). The use of robotics technology to study human joint kinematics: a new methodology. *Journal of biomechanical engineering*, *115*(3), 211-217.

[36] Rudy, T. W., Livesay, G. A., Woo, S. Y., & Fu, F. H. (1996). A combined robotic/universal force sensor approach to determine in situ forces of knee ligaments. *Journal of biomechanics*, *29*(10), 1357-1360.

 [37] Li, G., Zayontz, S., DeFrate, L. E., Most, E., Suggs, J. F., & Rubash, H. E. (2004). Kinematics of the knee at high flexion angles: an in vitro investigation. *Journal of Orthopaedic Research*, *22*(1), 90-95.

[38] Li, G., Papannagari, R., E Defrate, L., Doo Yoo, J., Eun Park, S., & J Gill, T. (2006). Comparison of the ACL and ACL graft forces before and after ACL reconstruction an in-vitro robotic investigation. *Acta orthopaedica*, *77*(2), 267-274.

[39] Noble, L. D., Colbrunn, R. W., Lee, D. G., van den Bogert, A. J., & Davis, B. L. (2010). Design and validation of a general purpose robotic testing system for musculoskeletal applications. *Journal of biomechanical engineering*,*132*(2), 025001.

[40] Lo, J., Müller, O., Dilger, T., Wülker, N., & Wünschel, M. (2011). Translational and rotational knee joint stability in anterior and posterior cruciate-retaining knee arthroplasty. *The Knee*, *18*(6), 491-495.

[41] Radin, E. L., & Paul, I. L. (1971). Response of joints to impact loading. I. In vitro wear. *Arthritis & Rheumatism*, *14*(3), 356-362.

[42] Shaw, J. A., & Murray, D. G. (1973). Knee joint simulator. *Clinical orthopaedics and related research*, *94*, 15-23.

[43] Blankevoort, L., Huiskes, R., & De Lange, A. (1988). The envelope of passive knee joint motion. *Journal of Biomechanics*, *21*(9), 705-720.

[44] Lewis, J. L., Lew, W. D., & Schmidt, J. (1988). Description and error evaluation of an in vitro knee joint testing system. *Journal of biomechanical engineering*, *110*(3), 238-248.

[45] Berns, G. S., Hull, M. L., & Patterson, H. A. (1990). Implementation of a five degree of freedom automated system to determine knee flexibility in vitro.*Journal of biomechanical engineering*, *112*(4), 392-400.

[46] McLean, C. A., & Ahmed, A. M. (1993). Design and development of an unconstrained dynamic knee simulator. *Journal of biomechanical engineering*, *115*(2), 144-148.

[47] Walker, P. S., Blunn, G. W., Broome, D. R., Perry, J., Watkins, A., Sathasivam, S., ... & Paul, J. P. (1997). A knee simulating machine for performance evaluation of total knee replacements. *Journal of biomechanics*,*30*(1), 83-89.

[48] MacWilliams, B. A., DesJardins, J. D., Wilson, D. R., Romero, J., & Chao, E. Y. S. (1998). A repeatable alignment method and local coordinate description for knee joint testing and kinematic measurement. *Journal of biomechanics*,*31*(10), 947-950.

[49] DesJardins, J. D., Walker, P. S., Haider, H., & Perry, J. (2000). The use of a force-controlled dynamic knee simulator to quantify the mechanical performance of total knee replacement designs during functional activity.*Journal of Biomechanics*, *33*(10), 1231-1242.

[50] Walker, P. S., Blunn, G. W., Perry, J. P., Bell, C. J., Sathasivam, S., Andriacchi, T. P., ... & Campbell, P. A. (2000). Methodology for long-term wear testing of total knee replacements. *Clinical orthopaedics and related research*, *372*, 290-301.

[51] White, B. F., D'Lima, D., Drueding, A. C., Cox, J., Carignan, F. J., & Dean, S. (2006). A simulator study of TKR kinematics using modeled soft-tissue constraint: Virtual soft-tissue control for knee simula-tion. *Journal of ASTM International*, *3*(8), 33-44.

[52] Stasiak, M. M., Imhauser, C., Packer, J., Bedi, A., Brophy, R., Kovacevic, D., ... & Torzilli, P. (2010). A novel in vivo joint loading system to investigate the effect of daily mechanical load on a healing anterior cruciate ligament reconstruction. *Journal of medical devices*, *4*(1), 015003.

[53] Gu, X. I., Leong, D. J., Guzman, F., Mahamud, R., Li, Y. H., Majeska, R. J., ... & Cardoso, L. (2010). Development and validation of a motion and loading system for a rat knee joint in vivo. *Annals of biomedical engineering*, *38*(3), 621-631.

[54] Sutton, L. G., Werner, F. W., Haider, H., Hamblin, T., & Clabeaux, J. J. (2010). In vitro response of the natural cadaver knee to the loading profiles specified in a standard for knee implant wear testing. *Journal of biomechanics*, *43*(11), 2203-2207.

[55] Stasiak, M. E., Wiznia, D., Alzoobaee, S., Ciccotti, M. C., Imhauser, C. W., Voigt, C., ... & Rodeo, S. A. (2012). A Novel Device to Apply Controlled Flexion and Extension to the Rat

Knee Following Anterior Cruciate Ligament Reconstruction. *Journal of biomechanical engineering*, *134*(4), 041008.

[56] Liu, A., Jennings, L. M., Ingham, E., & Fisher, J. (2015). Tribology studies of the natural knee using an animal model in a new whole joint natural knee simulator. *Journal of biomechanics*, *48*(12), 3004-3011.

[57] Verstraete, M. A., & Victor, J. (2015). Possibilities and limitations of novel in-vitro knee simulator. *Journal of biomechanics*, *48*(12), 3377-3382.

[58] Biden, E. (1981) The mechanics of synovial joints. D. Phil thesis, University of Oxford.

[59] Biden, E., O'Connor, J., & Goodfellow, J. (1984, February). Tibial rotation in the cadaver knee. In *Transactions of the 30th Meeting of the Orthopaedic Research Society* (Vol. 30).

[60] Biden, E., & O'Connor, J. (1990). Experimental methods used to evaluate knee ligament function. *Knee ligaments: structure, function, injury, and repair*, 135-151.

[61] Fitzpatrick, D. P. (1989) Mechanics of the knee joint. D. Phil thesis, University of Oxford.

[62] Kantomaa, T. U. O. M. O., & Hall, B. K. (1988). Organ culture providing an articulating function for the temporomandibular joint. *Journal of anatomy*, *161*, 195.

[63] Lin, Y. C. (2015). Novel organ culture model for a complete synovial joint: creation and application.

[64] Drewniak, E. I., Jay, G. D., Fleming, B. C., Zhang, L., Warman, M. L., & Crisco, J. J. (2012). Cyclic loading increases friction and changes cartilage surface integrity in lubricin-mutant mouse knees. *Arthritis & Rheumatism*, *64*(2), 465-473.

[65] Nugent-Derfus, G. E., Takara, T., O'neill, J. K., Cahill, S. B., Görtz, S., Pong, T., ... & Klein, T. J. (2007). Continuous passive motion applied to whole joints stimulates chondrocyte biosynthesis of PRG4. *Osteoarthritis and cartilage*, *15*(5), 566-574.

[66] McNulty, M. A., Loeser, R. F., Davey, C., Callahan, M. F., Ferguson, C. M., & Carlson, C. S. (2011). A comprehensive histological assessment of osteoarthritis lesions in mice. *Cartilage*, *2*(4), 354-363.

[67] Louati, K., Vidal, C., Berenbaum, F., & Sellam, J. (2015). Association between diabetes mellitus and osteoarthritis: systematic literature review and meta-analysis. *RMD open*, *1*(1), e000077.

[68] Berenbaum, F. (2012). Diabetes-induced osteoarthritis: from a new paradigm to a new phenotype. *Postgraduate medical journal*, *88*(1038), 240-242.

[69] Verzijl, N., Bank, R. A., TeKoppele, J. M., & DeGroot, J. (2003). AGEing and osteoarthritis: a different perspective. *Current opinion in rheumatology*, *15*(5), 616-622.

Appendix A: Joint Processing Protocol

Joint Collection and Decalcification

Day 1:

1. Harvest joints from device

2. Fill labeled vials with 3 ml of PFA solution under hood (do not inhale PFA vapors). Keep vials on ice.

3. In a 10 cm petri-dish, fill halfway with sterile PBS and place joint in.

4. Trim off excess muscles from ones carefully so as to not damage the joint (allow excess tissue to float off into PBS)

5. Place trimmed joints into 3 ml of PFA solution quickly, and allow to incubate overnight in shaker in cold room.

Day 2:

1. Remove PFA solution under hood and dispose of in appropriately labeled container.

2. Wash joints twice with 3 ml of PBS for 10 minutes each. Place of room temperate rocker for wash.

3. Remove PBS solution from second wash and replace with 3 ml decalcification solution. Allow to incubate in cold room for 3 days.

Day 5:

1. Change decalcification solution. Allow to incubate in cold for additional 3 days.

Day 7/8:

1. Remove decalcification solution.

2. Replace with 3 ml of PBS if not ready for dehydration. If ready, proceed to dehydration

Joint Processing for Paraffinization

Materials:

25% Ethanol (diluted in PBS)

50% Ethanol (diluted in PBS)

75% Ethanol (diluted in sterile water)

100% Ethanol

Xylene

Day 1:

1. Wash joints in 3 ml of 25% ethanol for 1 hour

2. Remove 25% ethanol solution and replace with 3 ml of 50% ethanol for 1 hour

3. Remove 50% ethanol solution and replace with 3 ml of 75% ethanol for 1 hour

4. Remove 75% ethanol solution and replace with 3 ml of 100% ethanol for 1 hour

5. Remove 100% ethanol solution and replace with new 3 ml of 100% ethanol for 1 hour

6. Remove 100% ethanol solution and replace with 3 ml of xylene for 1 hour

7. Remove xylene and replace with new 3 ml of xylene for overnight

Day 2:

1. Place joints in liquid paraffin overnight

Day 3:

1. Embed joints into blocks of paraffin. Allow to harden and then section.

Appendix B: Safranin O Staining Protocol

1. Deparaffinize and hydrate sections.
   a. 2 x 5 minutes Xylene
   b. 2 x 5 minutes 100% Ethanol
   c. 1 x 3 minutes 75% Ethanol
   d. 1 x 3 minutes 50% Ethanol
   e. 1 x 3 minutes 25% Ethanol
   f. Carry to bench in deionized water or PBS

2. Stain sections in Weigert's Iron Hematoxylin for 10 minutes.

3. Wash in warm tap water.
   a. 2 x 3 minutes warm tap water
   b. 1 x 4 minutes warm tap water

4. Dip in distilled deionized water.

5. Stain slides in 0.02–0.1% Fast Green for 10 minutes (can extend if necessary).

6. Using a pipet, gently rinse slides with 1% Acetic Acid.

7. Stain slides in 1% Safranin O for 30 minutes.

8. Dip slides in 100% Ethanol.
   a. 2 x 3 dips
   b. For more conservative staining, dip once in each container of 100% Ethanol, tapping off the excess after each dip.

9. Clear slides in Xylene (5-10 dips, until the bubbles disappear).

10. Mount a coverslip on each slide using Permount. Allow to dry in the chemical hood overnight.
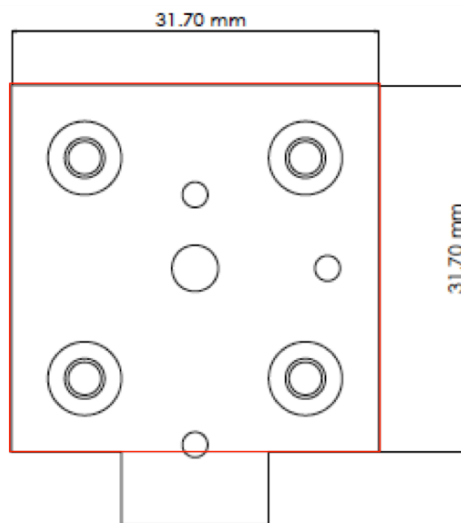
Appendix C: Link Shape Assumptions

Figure 123: Link AB Shape Assumption

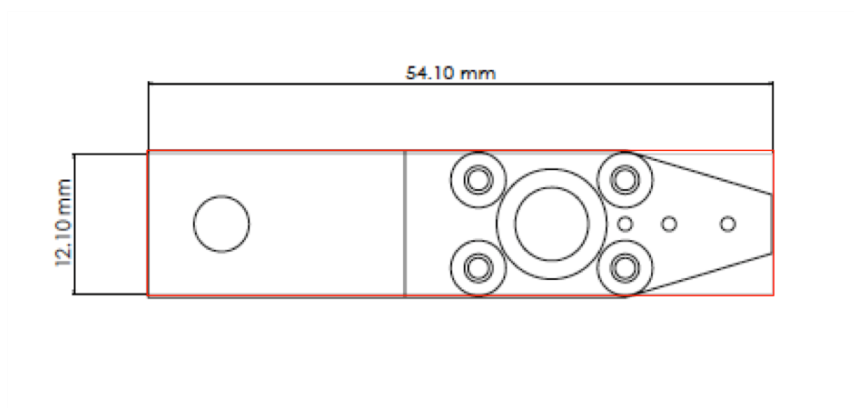

Figure 124: Link BC Shape Assumption
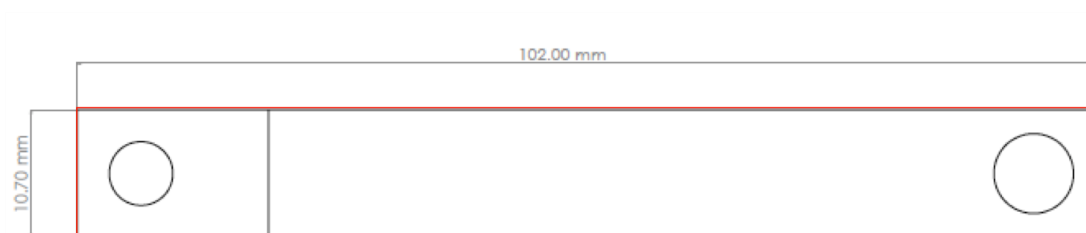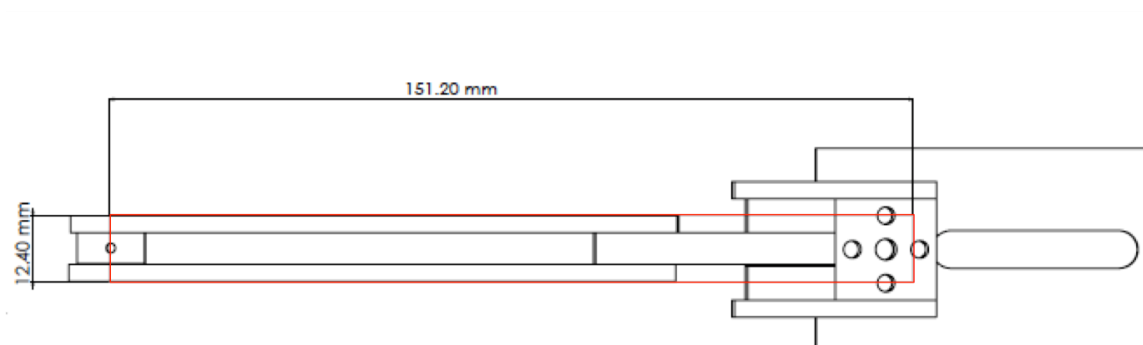
Figure 125: Link CF Shape Assumption

Figure 126: Link FE Shape Assumption

Figure 127: Link ED Shape Assumption